Assemblies and polymerizations

Exploring the electrical and mechanical properties of organic molecules on metal surfaces

Inauguraldissertation

zur

Erlangung der Würde eines Doktors der Philosophie

vorgelegt der

Philosophisch-Naturwissenschaftlichen Fakultät

der Universität Basel

von

Philipp D'Astolfo

Basel, 2022

Genehmigt von der Philosophisch-Naturwissenschaftlichen Fakultät
auf Antrag von:

Prof. Dr. Ernst Meyer
Prof. Dr. Stefan Willitsch
Prof. Dr. Ingmar Swart

Basel, 16. November 2021

Prof. Dr. Marcel Mayor, Dekan

Abstract

Understanding the interaction of molecules and metal surfaces is of paramount importance in research and engineering of new microchips, solar cells and nanobots for medical application. Progress in these fields requires minimizing mechanical wear and energy dissipation to increased stability of the components used. This work aims to investigate the mechanisms underlying molecular self-assembly and its resulting electronic properties along with adsorption and desorption of molecules. To this extend scanning tunneling microscopy (STM) and atomic force microscopy (AFM) in ultra-high vacuum at low temperature are utilized and complemented with molecular dynamics (MD) simulations as well as density functional theory (DFT) calculations.

Two distinct quantum dot arrays (α and β), self-assembled from pyrene derivatives on $Ag(111)$, are characterized by high-resolution AFM with a CO-modified tip, energy dissipation measurements and scanning tunneling spectroscopy (STS). The energy bands formed by interaction of the respective quantum dots of the α- and β-arrays were lower in the β-network compared to α and the interdot-tunneling rates and quantum-capacitances were reduced.

To investigate the mechanical behavior of poly-pyrenylene and poly-anthracenylene chains lifting and sliding experiments of pyrene- and anthracene-polymers were performed by AFM unveiling the rotational mechanics of single monomers as well as a snakelike motion during lifting of the pyrenylene chain. Sliding experiments further revealed a total change in mechanical behavior within the lifting distance of one monomer due to the intrinsic flexibility of the chain. A much stiffer structure, a pyrene-based graphene nanoribbon (pGNR), was then manipulated showing a a different sliding characteristic. This illustrated the importance of polymer degrees of freedom versus sliding behavior. Finally a polymer of sterically frustrated anthracene derivatives was peeled from the surface and gently redepositioned for stabilization of rotational conformers. Complementary MD simulations were used to investigate the influence of polymer length and pinning strength of the polymer-end on the desorption behavior.

This work unveils new aspects of quantum dot arrays self-assembled from organic mol-

ecules and characterizes the behavior and mechanical stabilization of organic polymers on metal surfaces in unprecedented detail to further technological advances.

Keywords: self-assembly, organic molecules, nanoporous networks, confined states, quantum dot arrays, quantum capacity, scanning tunneling microscopy, scanning tunneling spectroscopy, atomic force microscopy, cryo force-spectroscopy, molecular manipulation, tribology, molecular dynamics simulation, density functional theory calculation

Zusammenfassung

Die Interaktion von organischen Molekülen und metallischen Oberflächen ist ein zentraler Mechanismus in der Weiterentwicklung verschiedener Technologien, wie z.B. Mikrochips, Solarzellen oder Nanoroboter für medizinische Anwendungen. Ein vertieftes Verständnis der Interaktionen kann zu Optimierung von Reibungseffekten, Minimierung von Energieverlusten, sowie einer erhöhten Stabilität einzelner Komponenten führen und damit diese Technologien maßgeblich verbessern. In dieser Arbeit werden daher Interaktionen verschiedener organischer Moleküle mit metallischen Oberflächen untersucht. Mittels Rastertunnelmikroskopie (STM) und Rasterkraftmikroskopie (AFM) im Ultrahochvakuum und bei tiefen Temperaturen wurden die Mechanismen der Selbstorganisation, die daraus resultierenden elektronischer Effekte, sowie Adsorption und Desorption von langkettigen Molekülen untersucht. Die experimentellen Ergebnisse wurden mit Simulationen der Molekulardynamik (MD) sowie Berechnungen mittels Dichtefunktionaltheorie (DFT) komplementiert.
Bei der Verdampfung von Pyren Derivaten auf eine einkristalline Silberoberflache konnte die Kondensation in zwei unterschiedliche Netzwerke (α und β) beobachtet werden. Die resultierenden Quantenpunktmatrizen wurden mit Hilfe von hochauflösenden AFM Messungen sowie Rastertunnelspektroskopie charakterisiert. Im Vergleich zum α-Feld, zeigten die durch die Quantenpunktnetzwerke erzeugten Energiebänder im β-Feld eine verminderung. Auch die Tunnelraten zwischen Quantenpunkten sowie die Quantenkapazität im β-Feld waren reduziert.
Um die Interaktion und Adsorption von langen Polymeren auf metallischen Oberflächen zu untersuchen, wurden Pyren und Athrazen Polymere auf einkristallinen Gold Oberflächen synthetisiert und mittels einer AFM Spitze von der Oberfläche angehoben, sowie über die Oberfläche gezogen. Pyren-Polymere zeigten gerichtete Rotationen einzelner molekularer Einheiten sowie eine schlangenhafte Bewegung des Polymer-Endes während des Anhebens. Wurde das Pyrene-Polymer über die Oberfläche gezogen, änderte sich das Verhalten des Moleküls drastisch. Die Bewegung änderte sich von reibungsreich zu reibungsarm, sobald die Distanz zwischen Spitze und Oberfläche um den Bruchteil einer Pyrene-Einheit erhöht wurde. Um den Einfluss von Rigidität

auf das Verhalten von Polymeren zu untersuchen, wurde ein Experiment mit Graphen-Nanobändern, basierend auf Pyren Molekülen (pGNR), als Bindeglied zwischen Experimenten mit Pyrene-Polymeren und klassischen Graphen-Nanobändern [1] durchgeführt.
Schließlich konnte die Stabilisierung von Polymeren unter Rotationsspannung gezeigt werden, in dem ein Anthrazen-Polymer angehoben und kontrolliert abgelegt wurde. Mittels MD Simulationen wurde der Effekt der Bindungsstärke des Polymer-Endes, sowie der Einfluss der Polymer-Länge, auf das Adsorptionsverhalten untersucht.
Die Ergebnisse dieser Arbeit vertiefen somit das Verständniss von Selbstorganisation, Adsorption und Reibung von organischen Molekülen auf metallischen Oberflächen. Damit könnten neue Technologien zur Datenspeicherung und Datenverarbeitung generiert, sowie reibungsarme Komponenten aus organischen Molekülen für Nanomaschinen entwickelt werden.

Contents

Introduction

In our everyday life, especially since the emergence of portable electronics such as smartphones, smartwatches and wearables, microelectronics and circuitry become increasingly smaller and are shrunk down to sizes of few nanometers. From the emergence of the first transistor in 1948 by J. Bardeen and W. H. Brattain [2] with a transistor of a few centimeters in size, a computer CPU nowadays hosts millions of transistors on an area ~ 10 cm^2 (*e.g.* AMD Epyc, transistor density: $39.23 \cdot 10^6$ mm^{-2} [3]) with a transistor gate-size of just 7 nm. The production of microelectronics therefore consumes a huge amount of noble metals like gold, copper and aluminium for conductive components and circuitry which can not be satisfied for a prolonged period of time since our resources are limited. Other means of conducting electrical signals, sensing of environmental changes, computing of instructions in microchips as well as storing information therefore have to be explored. Another difficulty lies in the effects that arise at these small length-scales, in the form of dissipated energy due to electrical heating which in turn can interact with surrounding components, adhesion of components to one another, as well as friction in moving and flexible parts (*e.g.* smart clothing or nanobots for medical application).
The same drawbacks of miniaturization, *i.e.* increasing quantum mechanical effects and energy dissipation, also hold true for data-storage. Due to the increasing demand of data storage with the simultaneous decrease in size of the bits, the density of storage units has to increase drastically. The density of components in solid-state-drives as well as magnetic domains in hard-drives however have reached a limit in the stability of the states stored that are now influenced by quantum mechanic events and the electric heating of the surrounding area.
A solution to these problems can be envisioned using carbon-based organic molecules in combination with noble metals, since atomically precise structures can be synthesized specifically for the desired application. Organic molecules are also flexible and simultaneously sturdy due to the strong character of the covalent bond between atoms. Carbon was already shown to be useful in many different applications, *e.g.* in the form of graphene [4], graphene nano ribbons (GNR) [5] and carbon nano tubes (CNT) [6, 7, 8]. These however are relatively big molecules and their synthesis still

challenging. Recently self-assembly and on-surface reactions of organic molecules on noble metals such as gold, silver and copper, with specifically designed precursor molecules have been used in the creation of graphene and GNRs with a variety of different edges [9, 10, 11, 12] as well as metal-organic-frameworks [13] where molecules and metal-adatoms self-assemble into a network on the surface.
Research on the interaction of organic molecules with these surfaces and understanding the mechanisms governing molecule-surface interaction as well as intra-molecular processes however is thus primordial. The advent of the scanning tunneling microscope (STM) [14, 15] and atomic force microscope (AFM) [16, 17] and recent improvements in topographical resolution via tip-modification [18] has enabled researchers to shed light onto these mechanisms. In 2014 Kawai *et al.* [19] were able to precisely quantify the friction force acting on an on-surface synthesized polymer being pulled over the surface of a gold sample. From there several other experiments manipulating molecules and ultimately uncovering the underlying mechanisms have been performed from conformational changes of molecules [20], charging single molecules therefore changing the adsorption geometry [21], to gaining insight into the conformational changes of DNA molecules lifted from a surface [22]. Other research focussed on the adsorption and coordination geometry of self-assembled-networks [23, 24], as well as the electronic interaction of confined electrons in supramolecular networks [25, 24].
This work aims to further increase the understanding of the molecule-surface interaction such as confinement of surface electrons and the resulting quantum mechanical effects, adsorption and desorption of organic molecules and the behavior of long molecules during motion over a surface. Chapter 1 introduces the concepts of supramolecular self-assemblies and the resulting electronic confinement as well as on-surface chemistry for the synthesis of elongated molecules. Scanning Tunneling Microscopy (STM) and Atomic Force Microscopy (AFM) at ultra-high vacuum and low temperature conditions are described in Chapter 2 along with methods to prepare the samples and the molecules to be investigated. In Chapter 3 the electronic confinement of surface electrons into two distinctly different supramolecular networks and the resulting electronic (band formation) and quantum-mechanical effects such as quantum capacitance and interdot coupling rates are studied. The characterization of the molecules and structure elucidation is performed using STM and AFM with modified tips. The mechanics and motion on the single monomer level of on-surface synthesized suspended polymers are unveiled in Chapter 4 using Cryo force-spectroscopy. This technique is also used in Chapter 5 to investigate the stabilization of sterically frustrated polymers synthesized on the surface. All molecular manipulation experiments were accompanied by molecular dynamic simulations and density functional theory calculations to further increase the understanding of the processes experimentally investigated.

Part I

Theory and Methods

1 Metallic surfaces and molecules

Coating or evaporation of molecules onto metallic and semiconductor surfaces is a research field that has gained much interest in the last decade, especially in the construction of transparent organic solar cells [26, 27] and flexible organic light emitting diodes (OLED) [28]. For these applications organic molecules consisting of mostly carbon rings and long alkyl chains are used.

1.1 Organic polycyclic molecules with conjugated π-electron system

Most organic molecules are based of at least one, if not several carbon rings, sometimes fused together. These carbon rings consist of four to seven carbon atoms connected by a covalent- or double bond. Single bonds are created by the overlap of either s- or p-orbitals (in the direction of the axis through both atoms) forming σ molecular-orbitals (MO). Overlapping additional p-orbitals subsequently creates double and triple bonds in the form of π MOs.
With alternation of single- and double-bonds the p-orbitals of the whole molecule can overlap, delocalizing the electrons over all π MOs, which is defined as conjugation of the π-system. This conjugation stabilizes the molecule by lowering the overall energy. Conjugation is especially prevalent in organic aromatic molecules where the electrons in the ring-system additionally follow Hückel's rule. This rule states, that the molecule in order to be aromatic and conjugated has to be planar and cyclic, with the amount of π-electrons following $4n + 2$ (with n a non-negative integer). In addition to Hückels rule the participating bonds in aromatic molecules are neither single nor double bonds, which becomes evident comparing the bond lengths and strengths for ethane, ethene and benzene (Tab. 1.1).

In cyclic organic molecules carbon can sometimes be replaced by another atom, e.g. nitrogen, oxygen or sulphur without losing the ring structure albeit only nitrogen preserving the aromaticity.

Molecule	Bond order	Bond length (Å)	Bond strength (kj mol^{-1})
Ethane	1	1.54	356
Ethene	2	1.33	636
Benzene	1.5	1.39	518

Table 1.1: ***Bond lengths and strengths of carbon bonds in different molecules.***

1.2 Top-down or bottom-up: methods for molecule synthesis

When synthesizing molecules in physics, biology and chemistry, generally two approaches can be utilized: top-down and bottom-up.

Top-down approaches usually take a compound or material that already includes the desired structure in its initial state and subsequently removes material until only the desired end product remains. This is used e.g. in optical lithography where a photosensitive chemical resist is coated onto a bulk-material, covered with a patterned geometrical mask and subsequently exposed to ultra violet (UV) light and developer solution (e.g. *tetramethylammonium hydroxide*) to remove the uncovered parts of the resist. The coated and patterned material is then exposed to chemical or plasma etching that removes areas not covered by the patterned resist from the bulk.
The same principle of removing parts of the initial state to achieve the end product can be used to create e.g. graphene and graphene nanoribbons (GNRs). For the production of graphene a graphite source can be used with either mechanical exfoliation (via adhesive tape) [29], ultrasonic exfoliation using dispersed graphite in liquid medium with subsequent sonication and centrifugation [30, 31, 32] or using mechanical cleaving with a single crystal diamond wedge [33]. GNRs can subsequently be created from graphite by nanotomy [34] and single graphene sheets [35, 36, 37, 38] or from carbon nano tubes (CNTs) [39, 40] by electron-beam lithography and plasma etching.
While these methods can produce large quantities of the desired structure the fragments and atoms that are removed during the procedure can pollute the sample surface and therefore negatively impact the experiments to be performed. Another problem of the top-down approach is the limited control when synthesizing small or narrow molecules of just a few Å due to the macroscopic scale of the methods presented. For small or narrow molecules it is more feasible to directly build them up from the ground.

Bottom-up methods use smaller building blocks to completely assemble the final product, much like using Lego to build the desired structures. Bottom-up fabrication is an integral method in the construction of e.g. microchips where the chip is build stepwise by printing, soldering and attaching other components, or cars where mechanical components are assembled into a working engine.
In organic chemistry this approach is used to create molecules for organic solar cells [27] and OLEDs [28] as well as polymers for wearables [41] and electrochemical sensors in

medicine [42]. In the pharmaceutical industry bottom-up processes are used to synthesize active ingredients for medical drugs from other compounds extracted from plants, animals, minerals and microbiological sources [43].
CNTs for use in engineering and research can be produced by arc discharge from graphite electrodes [44], laser ablation of a graphite target [45] or chemical vapor deposition using various catalysts such as metals and carbon-containing gases [46, 47, 48]. Graphene and GNRs can similarly be synthesized using fitting precursor molecules [9, 49].
The drawback of Bottom-up fabrication or synthesis is at the same time its strength. Due to the precision of the synthesis production of large and complex compounds takes time and is rarely feasible in industrial applications. For research purposes however Bottom-up synthesis can achieve small molecules and molecular networks with atomic precision.

1.3 Molecules on surfaces

Having a surface be covered with molecules can be achieved by various methods depending on the layer thickness desired. For coverages of up to three monolayers thickness simple sublimation of ready-to-use light molecules from a molecular powder [50] or electro-spray deposition [51, 52] of heavier and bigger molecules e.g. DNA molecules [22] can be used. Another alternative would be the synthesis of the targeted molecule directly on the surface using specific precursor molecules.

1.3.1 Molecular self-assemblies

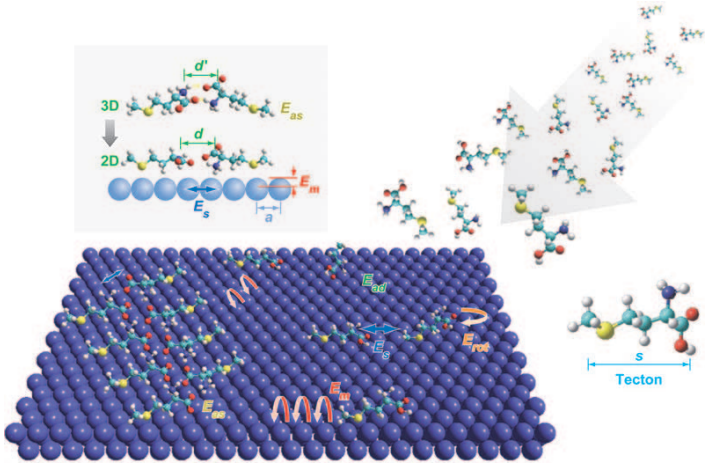

Figure 1.1: ***Mechanism of Supramolecular engineering.*** *Self-assembly of amino acids into a twin-chain is influenced by the adsorption (E_{ad}), migration (E_m) and rotation (E_{rot}) of the precursors as well as molecule-surface (E_s) and direct interaction (E_{as}). (Reprinted with permission of Annual Reviews [53])*

The concept of self assembly of smaller and bigger molecules can be discovered all

through nature, in the formation of cells, proteins or viruses. It can be defined as spontaneously formed, structurally well defined and stable aggregates of molecules under equilibrium conditions mediated by non-covalent bonds [54]. An illustration of a self-assembly process using amino acid precursor molecules into a twin chain is given by J. V. Barth [53] (Fig. 1.1) where the self-assembly is influenced by adsorption, migration and rotation of the precursors as well as molecule-surface and direct molecule-molecule interactions.
The first supramolecular self-assemblies on metal surfaces investigated by Scanning Tunneling Microscopy (STM) were already reported as early as 2002 by Griessl *et al.* [55] and Dmitriev *et al.* [56]. Many molecules, when evaporated onto a metal surface such as gold (Au), silver (Ag), copper (Cu) or lead (Pb) held at room temperature, assemble into close-packed networks [53, 56, 55]. The assembly is mediated by non-covalent bonds either between the molecules directly [56, 55, 57] or via interaction and coordination with a metal adatom inbetween molecules (metal-organic-framework, MOF) [13, 58].
A direct self-assembly of molecules mainly results due to interaction between electron-

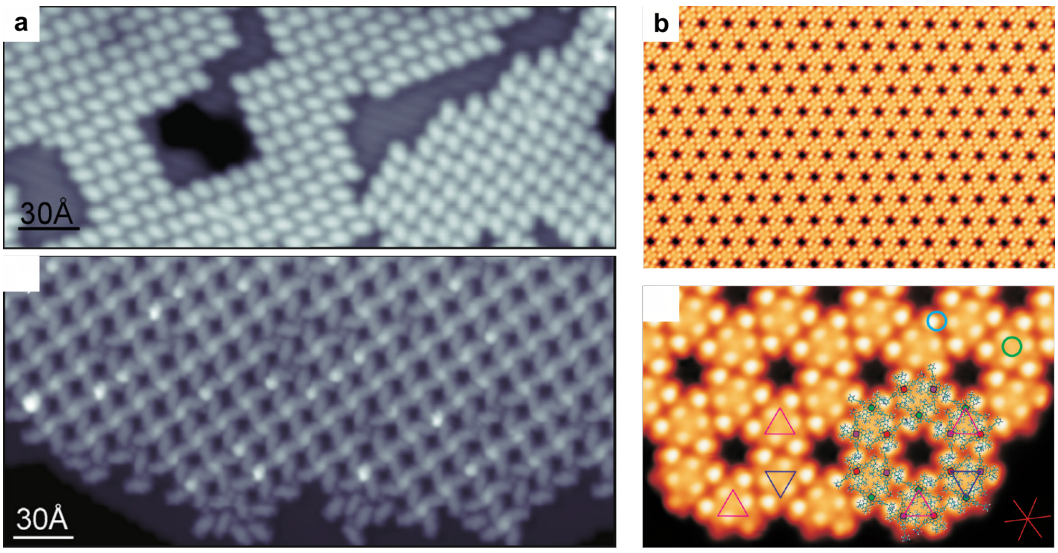

Figure 1.2: ***Self-assembled molecular layers on metal surfaces. a,*** *STM image of the close-packed- and metal mediated network-assembly respectively of TNAP molecules on $Pb(111)$.* ***b,*** *Hydrogen-bond driven assembly of porphyrin derivates on $Ag(111)$. (Reprinted with permission from Applied Surface Science [59] and ACS Nano [60] respectively)*

rich moieties such as oxygen, nitrogen or sulphur (or other atoms with free electron pairs) with hydrocarbon or hydroxyl groups of neighboring molecules. Other driving factors for self-assembly can be high surface coverages and molecule surface registry. Two different molecular self-assemblies of molecules on metal surfaces are illustrated in Fig. 1.2. Shown in Fig. 1.2**a**, Ahmadi *et al.* [59] evaporated TNAP molecules at low temperature conditions onto $Pb(111)$ with the molecules forming a close-packed structure. This assembly is guided by intermolecular electrostatic forces between the nitro-

gen atoms (electronegative) and hydrogen atoms of the molecular backbone. Evaporating the same molecules at higher temperatures changes the assembly mechanism, incorporating *Pb* adatoms into the network forming a MOF (Fig. 1.2**b**).
In 2010, Écija *et al.* [60] already created a self-assembled nanoporous network by evaporating porphyrin derivatives onto a heated *Ag*(111) surface. The assembly in this case was driven mainly by van-der-Waals interaction between the molecules along with weak intermolecular hydrogen bonding between different side-groups of the molecules. Porous networks such as this were later used in the creation of quantum dot arrays [23, 13, 57] where self-assembly is used to create supramolecular networks that confine the surface electrons into their cavities.

1.3.1.1 Electronic confinements in porous networks

Confinement of surface electrons into self-assembled nanoporous networks was first discovered by Lobo-Checa *et al.* [25]. They used *DPDI* molecules on *Cu*(111) to confine the 2D electron gas (2DEG) of the *Cu* surface into the pores of the network (Figs. 1.3**a** and **b**). These confined electrons interacted through the barriers posed by the molecules to create a energy band that could be measured by angular resolved photo-electron spectroscopy (ARPES), shown in Fig. 1.3**c**.
In 2017 Piquero-Zulaica *et al.* [57] used the same approach but with other molecules

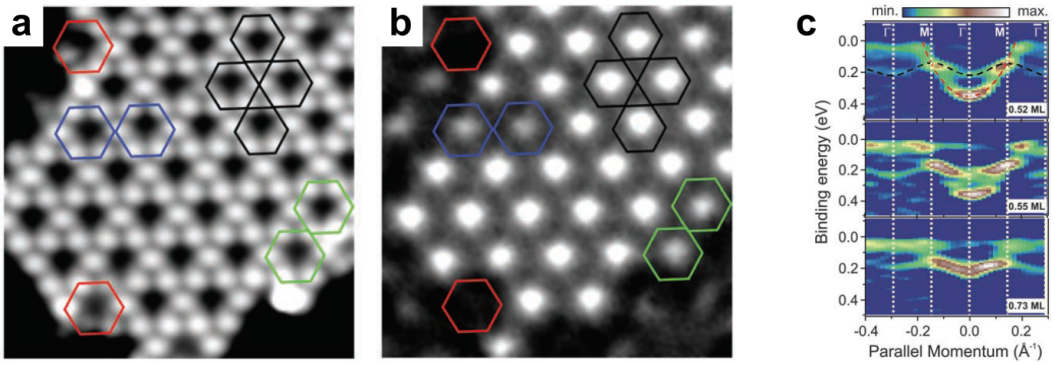

Figure 1.3: ***Formation of quantum dot arrays of confined electrons.*** ***a,*** *STM measurement of the nanoporous network on Cu*(111)*.* ***b,*** *dI/dV-map simultaneously acquired at* $V_{\text{Bias}} = -220$ mV*.* ***c,*** *Energy dispersion measurements depending on the surface coverage of the nanoporous network. (Reprinted with permission from Science [25])*

to confine the 2DEG of a *Ag*(111) surface into precisely engineered networks with controllable wall width therefore manipulating the coupling strength between the confined states. Using molecules with a sulphur center atom produced single molecule domain walls (SW), shown in Fig. 1.4**a**, whereas molecules with a oxygen moiety resulted in double-walls (DW), depicted in Fig. 1.4**b**. Subsequently the interdot spacing between the cavities increased in the DW case compared to the SW network. The influence of the molecular networks as well as their wall width on the 2DEG could again be measured by dI/dV spectroscopy and ARPES (Fig. 1.4**c**). In the SW network the

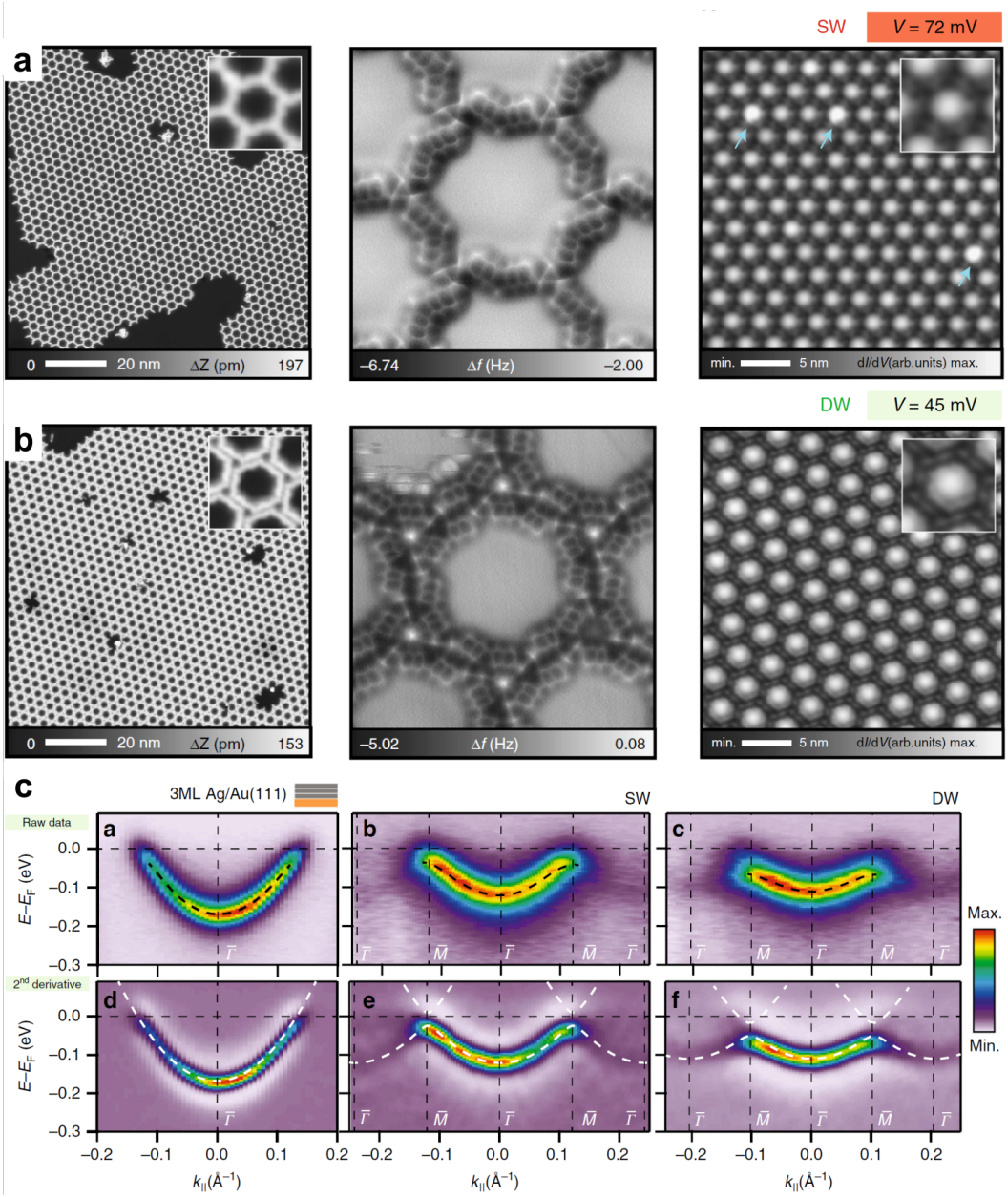

Figure 1.4: ***Precise engineering of a QDA. a,*** *Single wall network on Ag(111): Topographic STM image, AFM measurement and dI/dV-maps at $V = 72$ mV.* ***b,*** *Double wall network on Ag(111): Topographic STM image, AFM measurement and dI/dV-maps at $V_{\mathrm{Bias}} = 45$ mV.* ***c,*** *ARPES measurement comparing SW and DW quantum dot arrays. (Reprinted with permission from Nat. Comm. [57])*

confinement of the electrons produced a resonance peak in the dI/dV spectrum at 72 mV whereas in the DW case the peak decreased to 45 mV. In ARPES measurements the influence of the domain wall width was visible by a flattening of the parabolic shape of the energy dispersion as well as a modulation of the edges of the energy band. These networks are unfortunately not stable under high temperatures since the mole-

cules react with the surface ultimately destroying the network. The reaction with the surface however can be used in the synthesis of new compounds.

1.3.2 On-surface chemistry

Surfaces, especially metal substrates, have long been of substantial importance in engineering, chemistry and physics. Palladium for example is used in the production, purification and storage of hydrogen as a green alternative to the usage of fossil fuels [61]. In recent years on-surface reactions have been used in the research of organic- and biomolecules because of their ability to be performed in vacuum.

1.3.2.1 Organic polymers synthesized by Ullmann-Coupling

Investigating long polymeric molecules as well as GNRs other big organic molecules was for a long time difficult due to the inability to evaporate intact molecules onto a sample surface. The first Ullmann-reaction of single molecules induced by STM was performed by Hla *et al.* [62] in 2000 on iodobenzene molecules on a Cu surface, reproducing the famous reaction uncovered by Ullmann *et al.* in 1904 [63]. They used the tip of an STM to manipulate iodobenzene molecules adsorbed at step edges, removing I atoms from the molecules. The newly formed benzene radicals were moved in close proximity to one another. Using a voltage pulse between tip and sample above the molecules a covalent bond between two radicals was formed, creating biphenyl molecules.
The reaction has since been refined removing the need of tip-induced complex creation. Nowadays thermal annealing under vacuum conditions is used to synthesize the desired molecules from specifically designed precursor molecules. In 2007 Grill *et al.* investigated the dependence of covalently bonded structures from porphyrin derivatives on $Au(111)$ on the evaporation temperature [64]. They reported on complex formation after thermal activation of the precursor molecules, with differently halogenated porphyrin moieties. Later in 2010 O. Blunt *et al.* used two halogenated molecules to synthesize a supramolecular network on $Au(111)$ as a template for the capture of fullerene molecules into the resulting cavities [65]. On-surface Ullmann-coupling with halogenated precursor molecules has since been used in the creation of other 2D polymers [66, 67] as well as other complexes using ethyne-moieties (triple bonded carbon) instead of halogen atoms [68, 69, 70].
Fan *et al.* reported in 2013 on the thermal on-surface synthesis of hyperbenzene on $Au(111)$, huge ring-like molecules of covalently bonded benzene rings [71]. They used thermal annealing surface to cleave the bromine atoms (Br) from the precursor molecules, forming molecule-metal intermediate states (Fig. 1.5**a**). Increasing annealing temperature resulted in covalently bonded hyperbenzene rings and zig-zag polymers without metal-intermediates (Fig. 1.5**b**).
On-surface Ullmann-coupling has since been a standard tool for the synthesis of long physisorbed chains for the investigation of molecule-surface interaction as well as intramolecular characteristics [72]. Kawai *et al.* synthesized polyfluorene chains from dibromoterfluorene molecules in order to lift them with the tip of an AFM [19]. They

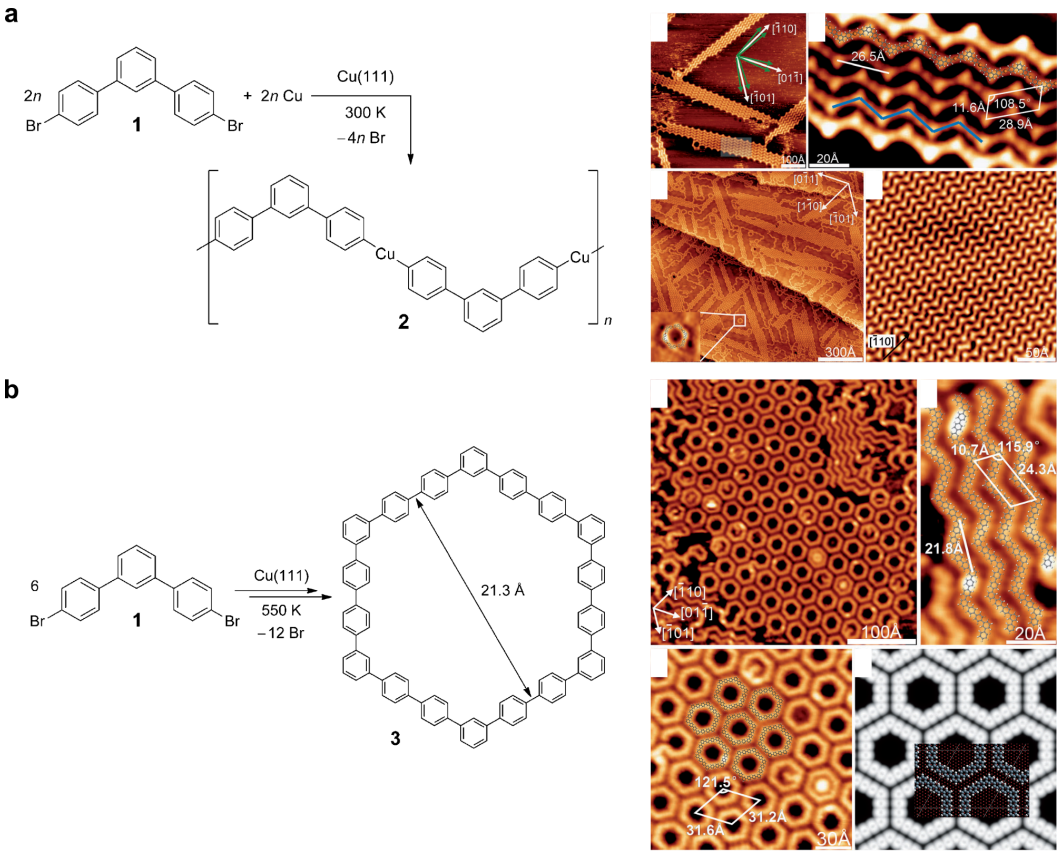

Figure 1.5: ***Ullmann-reaction by thermal annealing.*** ***a,*** *Reaction pathway along with STM measurements of the metal-mediated intermediate state.* ***b,*** *Reaction pathway and STM measurements of the fully reacted hyperbenzenes. (Reprinted with permission from Angew. Chem. Int. Ed. [71])*

also investigated the stepwise reaction of the precursors into polyfluorene chains by tip-modified AFM measurements with a *CO*-tip [73], imaging precursor molecules, metal-mediated intermediates as well as the final polymer. The stepwise reaction of two precursor molecules with metal-organic intermediate states was also investigated by Zint *et al.* in 2017, utilizing STM, AFM with *CO*-modified tips along with DFT calculations of the reaction [74]. Choosing the right precursor, even doped GNRs can be synthesized as shown by Pawlak *et al.* in 2020 [10]. They utilized brominated *tetrabenzophenanzine* precursor molecules and surface-promoted reactions to create highly *N*-doped porous GNRs on *Ag*(111).
Taking on-surface chemistry a step further not only polymers and 2D networks can be synthesized.

1.3.2.2 Cyclodehydrogenation and synthesis of Graphene Nanoribbons

By choosing the right precursor molecules graphene nanoribbons (GNR) can be created with different edge structures depending on the precursor. The influence of the edge state on the electronic and magnetic properties is of much interest in the research

of Quantum dots [75] and engineering of components for microelectronics (e.g. GNR field-effect-transistors) [76].
In 2010 Cai *et al.* produced a 7-carbon atoms wide GNR with armchair (AGNR) edge configuration from *dibromo-dianthryl* precursor molecules and a chevron-type GNR from *dibromo-tetraphenyltriphenylene* precursors [9] (Fig. 1.6) with high yields. In both cases, the cyclodehydrogenation reaction occurs at high temperature between opposing hydrocarbon atoms that are sterically frustrated. In a first step the opposing hydrogen atoms are cleaved from the carbon atoms before in the second stage a covalent bond is created (second step in the reaction pathway in Figs. 1.6**a** and **b**).
Not only GNRs with armchair edges (Fig. 1.6**a**), or modifications of armchair edges

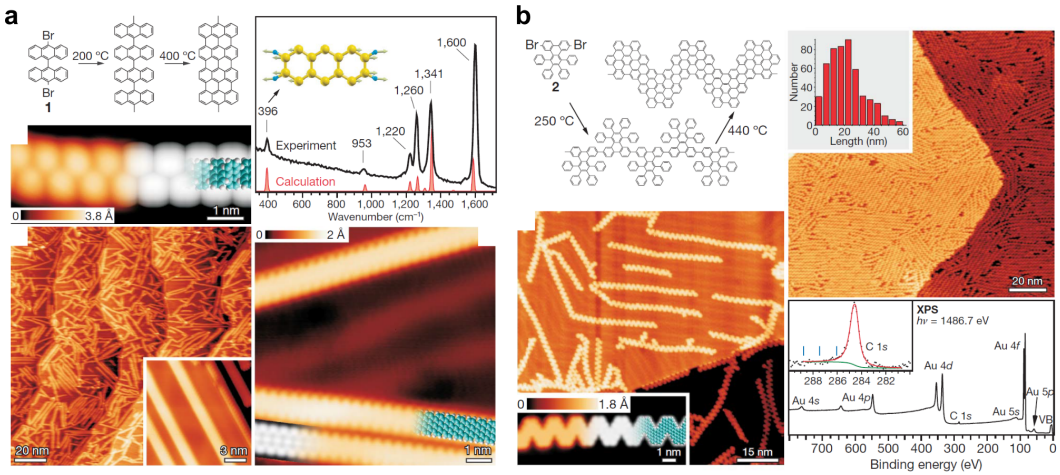

Figure 1.6: ***Precise synthesis of GNRs on Au***(111)**.** ***a,*** *Synthesis and measurements of a 7-AGNR.* ***b,*** *Reaction pathway, STM measurements and XPS data of chevron-like GNRs. (Reprinted with permission from Nature [9])*

(Fig. 1.6**b**), can be created, but also zigzag edges (ZGNR). In 2016 Ruffieux *et al.* produced a 6-ZGNR using a modified anthracene precursor [11] (Fig. 1.7**a**). They first used a U-shaped *dibenzo[a,j]anthracene* precursor (**1**) in a preliminary study to exemplify the snakelike polymer formation before further modifying the precursor molecule with a *bimethyl-bithenyl* group in the center of the U-shaped anthracene backbone (**1a**) to fill the gaps. The resulting polymer (Fig. 1.7**b** left) was further annealed at higher temperatures yielding the fully conjugated ZGNR (Fig. 1.7**b** right and bottom).
In recent years on-surface synthesis with cyclodehydrogenation has been used to create fullerenes [77], nanographenes [78], doped GNRs [12], alternating 7/9-AGNRs [79] and long AGNRs for use in friction experiments [1]. In 2018 Gröning *et al.* synthesized edge-extended 7-AGNR-S(1,3) nanoribbons for research in topological quantum phases [80]. Recently Sun *et al.* (2020) created a narrow width-modulated pyrene-based GNR (pGNR) with a ultralow bandgap where its charge carriers behave as massive dirac fermions [81].
These polymeric molecules can be envisioned to be used as flexible ultrathin wires in organic microelectronics. Characterization of on-surface synthesized molecules can therefore be performed using AFM to shed light onto adsorption and friction mechanics

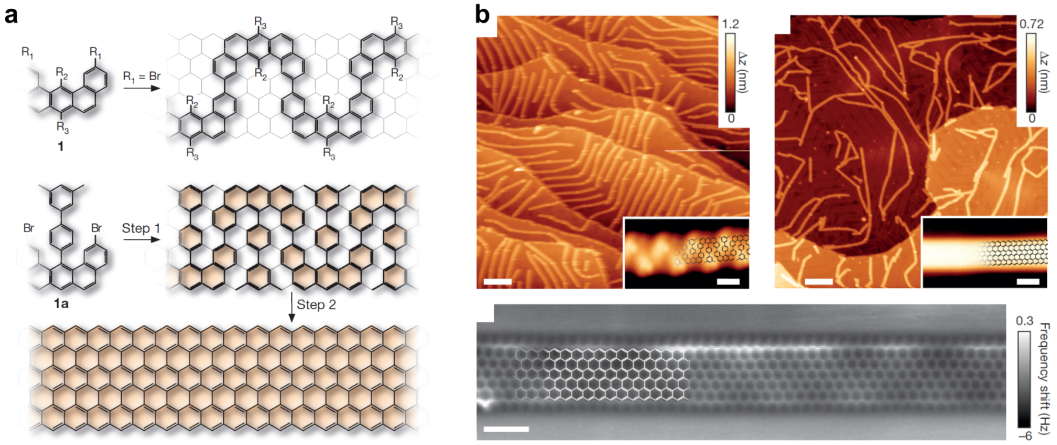

Figure 1.7: ***On-surface synthesis of a ZGNR. a,*** *Reaction pathway towards ZGNRs.* ***b,*** *STM images of the molecules after Ullmann-polymerization (left) and after cyclodehydrogenation (right). Bottom: AFM image with CO-tip of the fully synthesized ZGNR. (Reprinted with permission from Nature [11])*

of moving molecules, electronic properties and conductance of physisorbed molecular chains suspended between tip and surface as well as intramolecular processes.

1.3.3 Molecular manipulation

1.3.3.1 Cryo-force spectroscopy of organic molecules

Force spectroscopy at cryogenic temperatures enables for extraction of adsorption-energies [82] and -forces [83] of molecules and intra-molecular processes such as rotation around bonds [84]. To measure these, the oscillating tip of the sensor (FM-AFM Mode) is positioned directly over the end of the molecule or polymer to-be-lifted and slowly approached onto the surface, reducing tip-sample separation. During approach, when the tip comes into range of the attractive forces of the molecule, the frequency shift (Δf, Eq. 2.15) becomes negative. The creation of a bond between molecule and tip subsequently results in a sudden jump in frequency shift (and tunnelling current for conductive molecules). The tip and bonded molecule are then slowly retracted, recording the frequency shift as a function of the distance retracted (or approached for molecules already lifted). Depending on the molecule lifted, the $\Delta f(z)$ graph can exhibit different features, ranging from repeating dips and ridges with characteristic separation lengths for GNRs [85] to detachment events that resemble a stick-slip motion of the adsorbed polymer [19] (Fig. 1.8) and exponentially decaying Δf signals with random detachment events recorded for single-strand DNA molecules [22]. The lifting experiments are usually performed, until either the molecule completely desorbs from the surface, or the bond connecting tip and molecule ruptures. Both are characterized by a sudden drop in frequency shift to $\Delta f = 0$ Hz with constant baseline.

Over the last years cryo-force spectroscopy with AFM has been used in the research of many different molecules. In 1997 Rief *et al.* used an AFM to unveil the conformational changes and increasing stiffness upon elongation of a long polysaccharide molecule [83].

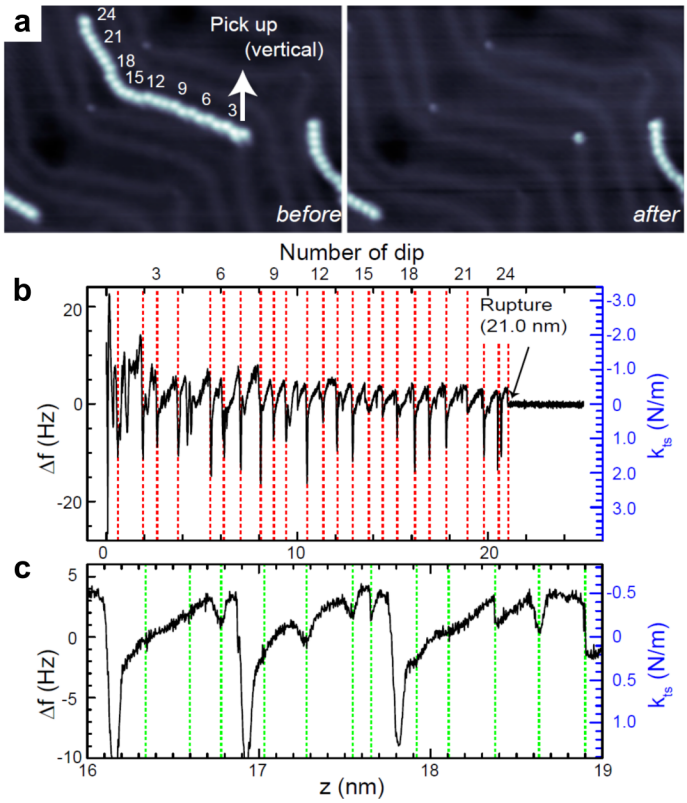

Figure 1.8: ***Cryo force spectroscopy of poly-dibromoterfluorene molecules.*** ***a,*** *STM measurements of the same area on the surface before and after the lifting experiment. The molecule is initially oriented along the fcc valley of the* $Au(111)$ *herringbone-reconstruction.* ***b,*** $\Delta f(z)$ *trace recorded during vertical lifting of the polymer from the arrow in* ***a****.* ***c,*** *Magnification of the* Δf *trace for* $z = 16 - 19$ nm. *(Reprinted with permission from PNAS [19])*

later in 2009 Lafferentz *et al.* probed the conductance of a conjugated polymer and its dependence on the length of the molecule [72] using a polyterfluorene molecule (the same molecule was later utilized by Kawai *et al.* to quantify the molecule-surface interaction and forces [19]). Using cryo force-spectroscopy the binding energies and van-der-Waals potentials between PTCDA (NTCDA and TTCDA respectively) molecules and the underlying surface were unveiled by Wagner *et al.* in 2012 [82] (and 2014 [86] respectively). Later in 2016 Pawlak *et al.* lifted a porphyrin derivative off a $Cu(111)$ surface using the tip of the AFM [87] for single-molecule friction experiments.

1.3.3.2 Experiments on suspended polymeric molecules and ribbons

Two factors impacting our everyday life are material wear and degradation, and therefore friction and the decay of electronic properties.

Friction experiments. To understand the first process, sliding experiments with suspended GNRs (Fig. 1.9**a**, performed by Kawai *et al.* in 2016 [1]), polymers and single molecules (Fig. 1.9**b**, reported by Pawlak *et al.* in 2016 [87]) can be performed. Similar to cryo force-spectroscopy experiments of the previous chapter, molecules can be picked up and lifted to the targeted height utilizing the tip of an AFM. Afterwards, the molecule is dragged (forward motion) and pushed (backward motion) over the sample surface by moving the tip in the desired direction, recording the resulting Δf. Lifting the molecule further (therefore increasing tip-sample separation), this process can be repeated several times as long as the tip-molecule bond persists. Height dependent friction -traces (Figs. 1.9**a** and **b** bottom) and -maps (Fig. 1.9**b** middle) can be acquired. Discrepancies between forward and backward motion, as well as periodicity and modulation of the traces can give information on the commensurability of molecule and surface as well as friction forces and energies [19] arising from the forces discussed in Chapter 2.1.2. An example of low friction, or superlubricity, is pictured in Fig. 1.9**a**, whereas high friction with stick-slip motion is shown in Fig. 1.9**b**.

Electronic characterization. As for the second effect, the electronic properties of molecules, conductance measurements of suspended static molecules as well as conductance during sliding experiments can be envisioned.
In the first case, the molecule is lifted to the desired height and the differential conductance versus bias voltage is recorded (STS spectroscopy), representing the local density of states (LDOS) of the suspended molecules. With this method, in 2009, Lafferentz *et al.* investigated the dependence of conductance of the polymer on the length of the molecule by varying the lifting height [72].
In the second case, the tunnelling current during sliding of the molecule at the desired height is recorded. By applying no bias voltage (*i.e.* $V_{\mathrm{Bias}} = 0$ V) the electronic forces are minimized, and any occurring tunnelling current during the polymer motion is induced by the oscillation of the molecule due to oscillations of the AFM tip.

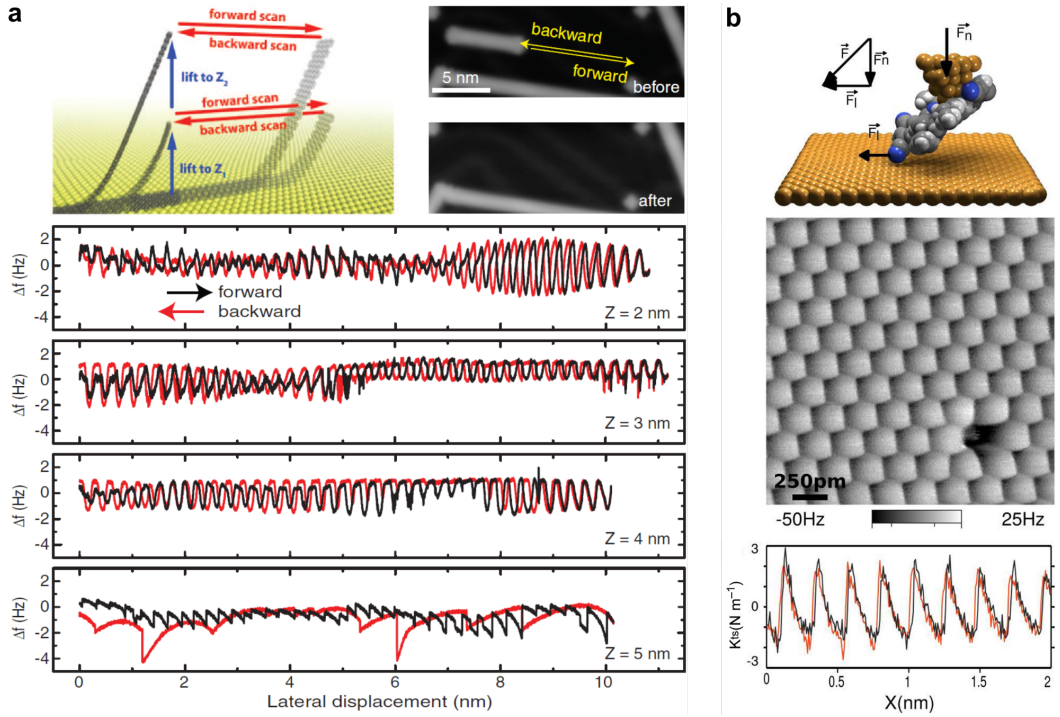

Figure 1.9: ***Friction experiments on GNRs and single molecules.*** ***a,*** *Dependence of frequency shift Δf on the lifting height for $z = 2-5$ nm. Top left: illustration of the lateral manipulation. Top right: STM image before and after the experiment.* ***b,*** *Single molecule friction experiment with a porphyrin-terminated tip. Top: illustration of the experiment with the molecule in direct contact with the Cu(111) surface. Middle: $\Delta f(x, y)$ maps acquired in constant height mode. The atomic lattice of Cu(111) is reproduced in the friction map. Bottom: Tip-sample stiffness k_{ts} corresponding to one line in the map revealing stick-slip events. (Reprinted with permission from Science [1] and ACS Nano [88] respectively.)*

2 Experimental Methods

2.1 Scanning probe microscopy

2.1.1 Scanning Tunneling Microscopy

Theory

Invented in 1982 by Ch. Gerber, G. Binnig and H. Rohrer [14, 15], Scanning Tunneling Microscopy (STM) is able to image the surface by tunnelling electrons from tip to sample when applying a bias between tip and surface (Fig. 2.1). This tunnelling current between two metals was first hypothesized by James Bardeen [89] in 1961. It was predicted that the wavefunction Ψ of the electrons from the tip can penetrate the energetic barrier of the vacuum between tip and sample and reach into the substrate. An electron-wavefunction obeys the Schrödinger Equation described as follows:

$$\left(-\frac{\hbar}{2m_\mathrm{e}}\frac{\partial^2}{\partial z^2} + U(z) - E_\mathrm{n}\right)\psi_\mathrm{n}(z) = 0 \tag{2.1}$$

where $\psi_\mathrm{n}(z)$ is the electron-wavefunction in z-direction (direction from tip to sample), $U(z)$ is the energy barrier of the vacuum, m_e the mass of an electron and E_n the eigenenergy of the electron-wavefunction. Neglecting the electron-electron interaction, treating the electron-wavefunction inside tip and substrate as a travelling wave and as a decaying wave inside the vacuum-barrier with dampening coefficient $\kappa = \frac{\sqrt{2m(U(z)-E)}}{\hbar}$ as well as defining the Energy barrier $U(z)$ as:

$$U(z) = \frac{\Phi_\mathrm{s} + \Phi_\mathrm{t}}{2} + \frac{eV_\mathrm{Bias}}{2} \tag{2.2}$$

with Φ_s and Φ_t the workfunction of sample and tip respectively, the tunnelling current in z-direction can be approximated as:

$$I(z) \propto \exp\left(-A\sqrt{\Phi}z\right) \tag{2.3}$$

$\Phi \approx \frac{\Phi_s+\Phi_t}{2}$ describing the average workfunction of tip and sample (Fig. 2.1**b**) and $A = 2\sqrt{\frac{2m_e}{\hbar^2}}$ a constant. Equation 2.2 shows that the energy barrier $U(z)$ can be modified by applying a bias voltage V_{Bias} between tip and sample. By increasing(decreasing) V_{Bias} the difference in E_F levels of tip and sample is increased(reduced), increasing(decreasing) the potential difference between tip and sample and ultimately the tunneling probability for electrons from tip to sample, enhancing or dampening the resulting tunneling current. As shown in equation 2.3, the tunnelling current further depends exponentially on the tip-sample separation (z) resulting in a high sensitivity of STM for small tip-sample separations.

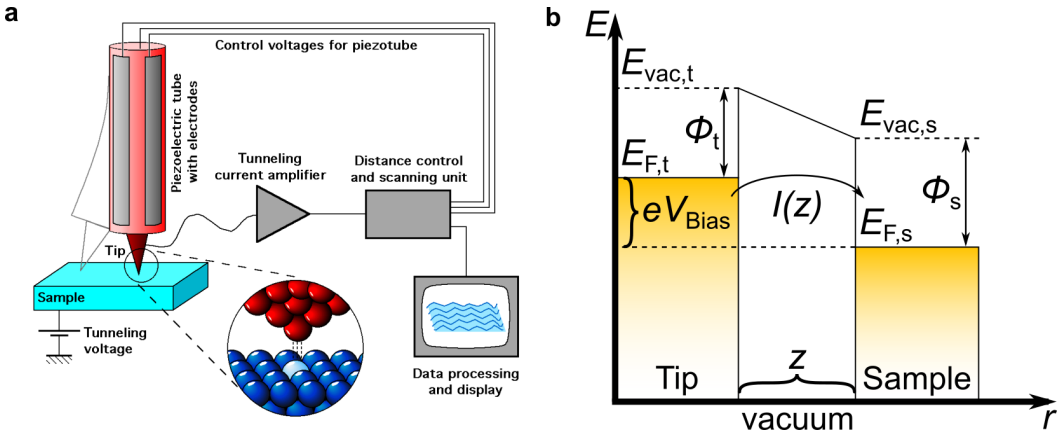

Figure 2.1: ***Work principle of the scanning tunneling microscope. a,*** *When applied with a bias voltage between tip and sample a tunneling current arises. The current is amplified and recorded by feedback electronics which both adjusts the lateral and vertical position of the tip using the piezoelectric tube as well as sends the changes of the tunneling current to the data processing/display electronics (Reprinted with permission from M. Schmid, TU Wien [90]).* ***b,*** *Schematic energy diagram with workfunctions Φ, vacuum barrier between tip and sample and tunneling current $I(z)$ after a bias voltage V_{Bias} is applied. $E_{\text{F,t/s}}$ denotes the Fermi energy level and $E_{\text{vac,t/s}}$ the vacuum energy level for tip/sample.*

Implementation

From equation 2.3 it can be seen, that the tunneling current for an applied bias voltage V_{Bias} changes upon variation of the tip-sample separation z, increasing for smaller z and decreasing for larger z, with the changes in z arising due to the variation of the surface morphology while scanning. The tip sample separation z can manually be reduced/increased via a piezoelectric tube (PZT) above the sensor, visible in Fig. 2.1**a**, that is able to extend/shrink depending on the voltage applied to the designated contact. The PZT is also used to change the lateral (x, y) position of the sensor on the surface by bending in the desired direction upon receiving a voltage on the corresponding contacts. The resulting tunneling current however has to be electronically amplified in order for changes to be detectable due to its small magnitude. To increase

the current recorded by decreasing z and simultaneously decrease the noise detected, the STM is usually operated in ultra high vacuum (UHV). Since the STM relies on a current tunneling from tip to sample (or vice versa), the samples to be measured have to be conducting, *e.g.* metal samples. With a current between tip and sample the STM can now be operated either in constant height or constant current mode.

Constant height. In the constant height mode the tip scans the surface at a predefined height processing the changing tunneling current directly into a representation of the surface. An advantage of this method lies in the speed of the measurements since only the current has to be recorded. The problem of this working principle however arises from danger of crashing the tip into the surface if the sample has big changes that exceed the predefined height (*e.g.* steep step-edges or defects), damaging tip (blunting of the apex), sensor and sample in the process.

Constant current. A safer way is the constant current mode, where the current between tip and sample is kept at a predefined value (I_{setpoint}) using feedback electronics. The electronics detect changes in tunneling current $I(z)$ due to the surface morphology and modify the tip-sample separation z accordingly by extending/shrinking the PZT until $I(z) = I_{\text{setpoint}}$. The adjustments to the current with respect to I_{setpoint} are recorded and translated into a representation of the surface. Since the tunneling current can only be altered as fast as the electronic systems permit, constant current mode is slower than constant height albeit being safer for tip, sensor and sample.

2.1.2 Atomic Force Microscopy (AFM)

Another research tool for the investigation of samples in UHV with atomic resolution is the atomic force microscope (AFM). It was invented by G. Binnig, C. Quate and Ch. Gerber [16, 17] in 1986. In contrast to STM, where the surface is imaged by tunneling a current from tip to sample, the AFM utilized the deflection of a cantilever (usually quartz, SiO_2) caused by the surface morphology while scanning the tip of the cantilever over the surface. This deflection is induced by interaction forces between tip and sample. A schematic drawing of the working principle is shown in Fig. 2.2**a**. This deflection was first measured by placing a STM tip over the cantilever, screening the changing tunnelling current in the junction. Today, the deflection of the cantilever is detected by reflecting a laser from the back of the cantilever onto a four-region photo-diode (Fig. 2.2**a**). The resulting signal from the photo-diode can then be used for the feedback electronics to adjust the (x, y, z) position of the cantilever as well as for displaying the surface via data processing.

The forces acting on a cantilever and tip (Fig. 2.2**b**) in vacuum can be described as:

$$F_{\text{ts}} = F_{\text{chem}} + F_{\text{el}} + F_{\text{vdW}} \tag{2.4}$$

with F_{chem} the chemical forces, F_{el} the electrostatic forces and F_{vdW} the van-der-Waals (vdW) forces. These forces act on different length-scales, starting from short-range (few Å) for F_{chem} to long-range (few nm) for F_{vdW} with F_{el} acting on short- and long-

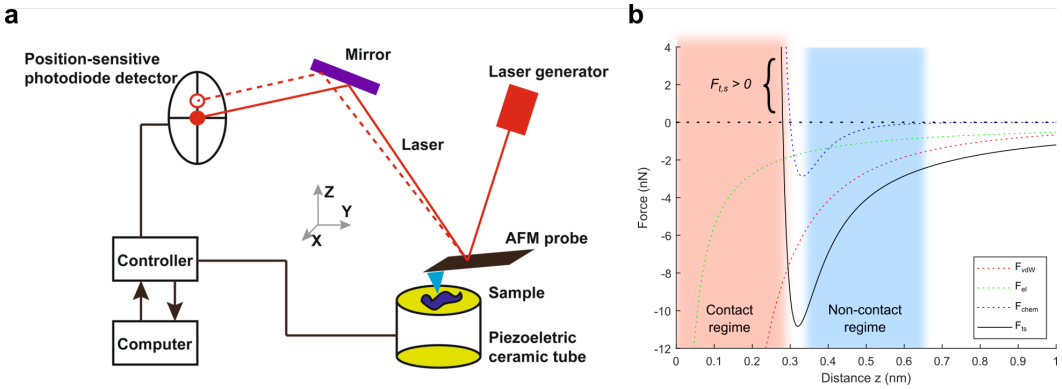

Figure 2.2: ***Work principle of the atomic force microscope.*** ***a****, Schematic drawing (Reprinted with permission from Journal of Nanobiology [91]).* ***b****, Interacting forces between tip and sample according to equation 2.10 (fitting parameters:* $\sigma = 300$ pm*,* $R = 20$ nm*,* $E_{\mathrm{Bond}} = 2$ eV*,* $A_{\mathrm{H}} = 1.25$ eV*,* $V_{\mathrm{Bias}} = 1$ V*).*

range tip-sample distances.

Chemical forces. For molecular manipulation and lifting experiments the chemical forces are of utmost importance, since a bond has to be created between tip and molecule. The interaction of two atoms that are in close proximity can be expressed by the Lennard-Jones (LJ) potential [92]:

$$U_{\mathrm{LJ}} = -\frac{E_{\mathrm{Bond}}}{\sigma}\left(2\left(\frac{\sigma}{z}\right)^{6} - \left(\frac{\sigma}{z}\right)^{12}\right) \tag{2.5}$$

$$F_{\mathrm{LJ}} = -\frac{\partial}{\partial z}U_{\mathrm{LJ}} = -\frac{12\,E_{\mathrm{Bond}}}{\sigma}\left(\left(\frac{\sigma}{z}\right)^{7} - \left(\frac{\sigma}{z}\right)^{13}\right) \tag{2.6}$$

E_{Bond} being the energy needed for bond creation and σ the distance, where Pauli repulsion and vdW-attraction equilibrate. The potential consists of two parts. The z^{-12} term empirically describes the short-range Pauli-repulsion of two atoms that arises due to repulsion between the atom cores whereas the z^{-6} term expresses the long-range forces that include the vdW forces between two atoms.

Electrostatic forces. The electrostatic contribution F_{el} to the total forces, arises due to potential differences between tip and sample, since they are characterized by different intrinsic electrostatic potentials. The junction can then be treated as a plate capacitor [93], with a distance dependent capacitance $C(z)$:

$$F_{\mathrm{el}} = -\frac{1}{2}\frac{\partial}{\partial z}C(z)V_{\mathrm{Bias}}^{2} \tag{2.7}$$

Taking into account the spherical geometry of the tip with radius R, equation 2.7 can be simplified to:

$$F_{\mathrm{el}} = -\pi\varepsilon_{0}\left(\frac{R^{2}}{z(z+R)}\right)V_{\mathrm{Bias}}^{2} \tag{2.8}$$

ε_0 denoting the vacuum permittivity.

Van-der-Waals forces. These forces describe the long-range interaction between all matter. They are comprised of interaction between macroscopic bodies, in our case uncharged atoms or molecules, and can be divided in three components. First the interaction between permanent dipole moments (Keesom force), second the interaction between a permanent dipole and an induced dipole or multipole (Debye force) and third between spontaneously induced fluctuating multipoles (London dispersion force) [94]. This third contribution, the London dispersion force is the dominating force of the vdW interactions. In 1937 Hamaker theorized that the vdW interaction of an agglomeration of atoms forming an object with radius R exerts a force on an object in distance z such as:

$$\begin{aligned} U_{\mathrm{vdW}} &= -\frac{A_{\mathrm{H}} R}{6z} \\ F_{\mathrm{vdW}} &= -\frac{\partial}{\partial z} U_{\mathrm{vdW}} = -\frac{A_{\mathrm{H}} R}{6z^2} \end{aligned} \tag{2.9}$$

with A_{H} the Hamaker constant that takes into account the material of the interacting objects. Apart from the electrostatic forces that can be increased by applying a bias voltage, the vdW forces are the main forces acting on the tip of an AFM at large tip-sample distances.

Summing up all interactions mentioned above, the total force can be defined as

$$F_{\mathrm{ts}} = -\frac{12\ E_{\mathrm{Bond}}}{\sigma}\left(\left(\frac{\sigma}{z}\right)^7 - \left(\frac{\sigma}{z}\right)^{13}\right) - \pi\varepsilon_0\left(\frac{R^2}{z(z+R)}\right)V_{\mathrm{Bias}}^2 - \frac{A_{\mathrm{H}} R}{6z^2} \tag{2.10}$$

A plot of F_{ts} is shown in black in Fig. 2.2**b** along with all components (F_{chem}, F_{el} and F_{vdW}). From equation 2.10 it becomes evident that in order to be sensitive to the short-range forces a sharp tip apex with a small radius (minimizing F_{el} and long-range F_{vdW}) is crucial. As pictured, the interaction force can be divided into two areas, where $F_{\mathrm{ts}} > 0$ is defined as the contact region and $F_{\mathrm{ts}} < 0$ the non-contact regime. Both regions can be used for AFM experiments with several working modes in each area of the force-graph. In contrast to STM however the curve is non-monotonic which is challenging to properly feedback (two solutions possible as setpoint).

Contact mode. The simplest of the measurement methods is contact mode, marked on the left side of the graph in Fig. 2.2**b**, where $F_{\mathrm{ts}} > 0$. Here the tip of the cantilever is brought in direct contact with the sample and therefore bends according to the morphology when moving over the surface. While scanning, either the height can be kept constant (similar to constant height mode of the STM) or the force that bends the cantilever according to the morphology. Both methods however are invasive and therefore have the intrinsic flaw, that both tip and sample are damaged in the process.

Non-contact mode. In order to minimize alterations or damage to the sample the cantilever scans the surface at a predefined height z (non-contact mode, blue area in Fig. 2.2**b**). It can then either kept static, only deflecting according to the forces acting on the tip (static non-contact mode), or can be oscillated over the sample (dynamic non-contact mode). Since in static non-contact measurements the cantilever has to equilibrate in every measurement point in order to accurately detect F_{ts} this method requires slow scan-speeds and measurements therefore take long time. For faster and non-invasive measurements dynamic non-contact mode is used, with modulation of either the oscillation frequency (FM-AFM) or the oscillation amplitude (AM-AFM). In FM-AFM the cantilever is excited on its fundamental resonance frequency with a PZT and the changes to the oscillation frequency due to the interaction with the surface dynamically detected using feedback-electronics. The resulting signal from the feedback can be used to adjust the tip-sample separation as well as display the sample via image processing of the data. The resonance frequency of the cantilever purely depends on the material and geometry used and is given by [95]:

$$f_0 = \frac{1}{2\pi}\sqrt{\frac{k^\star}{m^\star}} = 0.162\frac{t}{L^2}\sqrt{\frac{Y}{\rho}} \tag{2.11}$$

with $k^\star$ the effective spring constant of the cantilever, $m^\star$ the effective mass, Y the Youngs modulus of the cantilever, L the length, t the thickness and ρ the mass density. When brought into close proximity of the surface, the frequency changes due to the forces acting on the tip and induce a frequency shift and a change of the effective spring constant (k_{ts} being the spring constant of tip-sample interaction)

$$f = f_0 + \Delta f \tag{2.12}$$

$$k^\star = k + k_{\mathrm{ts}} \tag{2.13}$$

If the interaction strength of tip and sample is very small compared to the spring constant of the cantilever, the frequency shift can be approximated by

$$\Delta f = \frac{f_0}{2k}k_{\mathrm{ts}} = -\frac{f_0}{2k}\frac{\partial}{\partial z}F_{\mathrm{ts}} \tag{2.14}$$

with F_{ts} derived from equation 2.10. During one oscillation cycle however the force gradient $\frac{\partial}{\partial z}F_{\mathrm{ts}}$ and therefore k_{ts} changes significantly. To take the changes into account perturbation theory can be used [95]. Averaging over one oscillation cycle, the frequency shift can be calculated as:

$$\Delta f = -\frac{f_0}{kA^2}\left\langle F_{\mathrm{ts}}z'\right\rangle \tag{2.15}$$

where A denotes the oscillation amplitude and z' the vertical deflection. As can be seen in Fig. 2.3**a** by tracking the resonance frequency f_0 using the frequency shift Δf as input to a phase-lock-loop (PLL) system, the interaction forces acting on the tip can be extracted (equation 2.15). A negative Δf occurs due to attractive forces acting on the sensor whereas a positive Δf due to repulsive forces respectively. For AM-AFM

the cantilever is exited not at resonance, but close to it. Interaction with the sample then induces a change in oscillation amplitude, as seen in Fig. 2.3**b** that can be tracked using the PLL system, analogous to FM-AFM.
In both cases, FM-AFM and AM-AFM, the sensor-sample separation can subsequently be adjusted to keep the tip-sample separation constant (constant force AFM) or the sensor is kept at the initial z-setpoint regardless of the topography of the sample (constant height AFM).

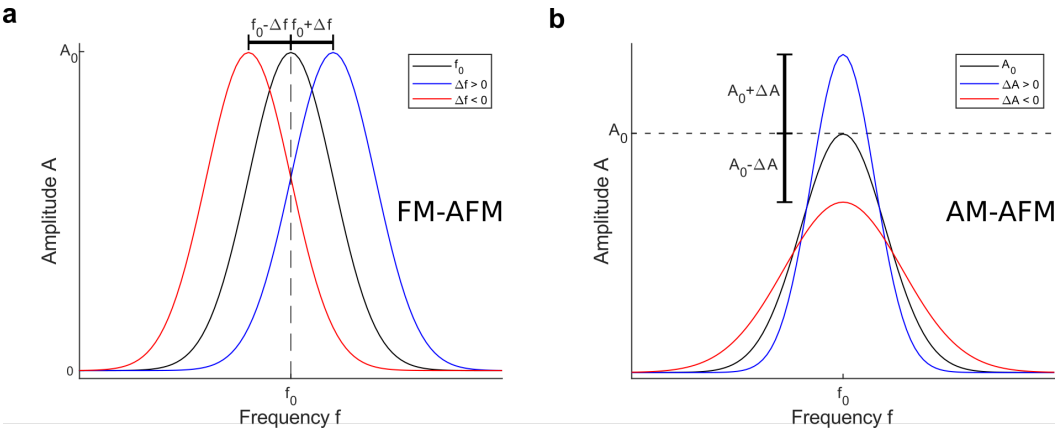

Figure 2.3: ***Comparison of FM-AFM and AM-AFM.*** *Influence of* F_{ts} *on* ***a,*** *the resonance frequency and* ***b,*** *the oscillation amplitude.*

2.1.3 qPlus sensor configuration: combined STM and AFM

Both measurement techniques, the STM and AFM, have their advantages and drawbacks. While STM allows fast measurement speed and probing of the electronic structure of the sample, AFM provides atomic resolution on non-conductive samples such as organic molecules and is sensitive to interaction forces between tip and sample/molecule. For AFM usually soft and long cantilevers are used, making them susceptible to faint interaction forces but also sudden changes of the forces and therefore prone to snapping into contact, damaging sample and tip. Due to the soft character of the sensor it is also prone to increased noise detection. The increased sensitivity to interaction forces and resolution however requires slower scanning speeds compared to STM.

In 1998 Giessibl *et al.* used quartz tuning forks, similar to tuning forks used in watch-making industry, as force sensors for AFM measurements [97, 98]. A schematic drawing of a tuning fork sensor (later qPlus) is shown in Fig. 2.4**a** where one prong is fixed to a support while a tip for sensing interaction forces is attached to the free prong. Since quartz (SiO_2) is a piezoelectric material the free prong can be mechanically excited via one set of electrodes while the deflection and change to the oscillation frequency due to interaction forces acting on the attached tip can simultaneously be read out with another set. Choosing a conducting tip material with a wire attached to a third electrode (visible in Fig. 2.4**b**) the tuning fork can simultaneously be used for

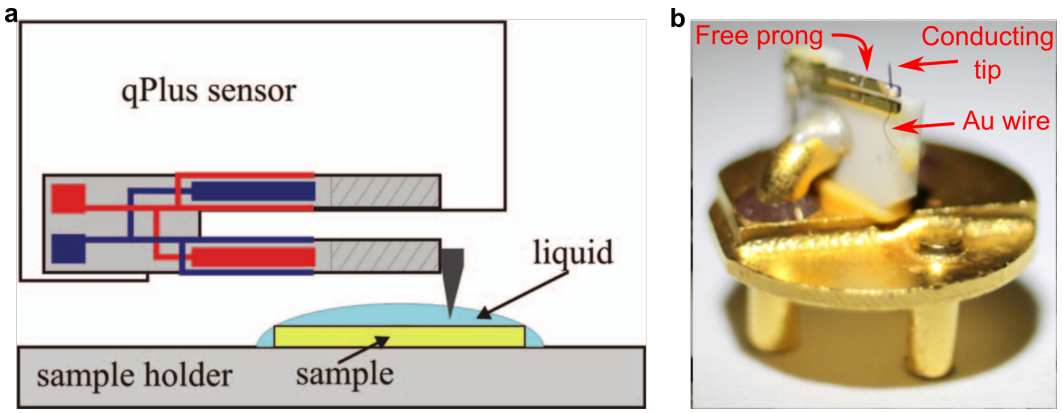

Figure 2.4: ***Combining STM and AFM into one tuning-fork sensor.*** ***a,*** *Schematic drawing of the qPlus sensor (Reprinted with permission of Review of Scientific Instruments [96]).* ***b,*** *Sensor mounted onto a support and tripod for use in UHV systems.*

AFM and STM measurements without the need for an exchange of the sensor. It also enables for subsequent scanning tunneling spectroscopy (STS) and force spectroscopy measurements respectively without the risk of losing the position to be measured. Both methods give local information of the sample surface with STS probing the electronic structure in form of the local density of states (LDOS) [99] by measuring the gradient of the current in response to a bias sweep, and force spectroscopy being able to sense changes in the interaction forces due to a bias sweep [100, 101, 102]. In this work STS and resulting LDOS is used to identify the highest occupied molecular orbital (HOMO) and lowest unoccupied molecular orbital (LUMO).

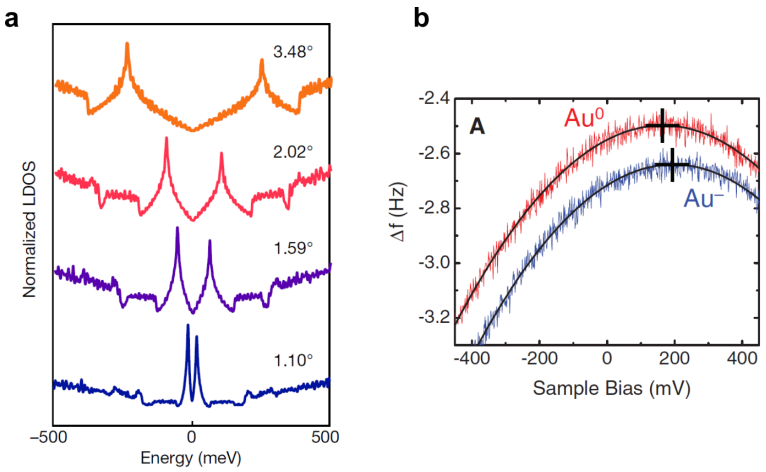

Figure 2.5: ***Examples of STS and Force spectroscopy.*** ***a,*** *STS spectra of twisted bilayer graphene under different rotational angles between the layers.* ***b,*** *Force spectroscopy measurement showing charging of a Au surface adatom on NaCl/Cu(111). (Reprinted with permission from Nature [103] and Science [102] respectively)*

2.2 Ultra-high-vacuum system at low temperature

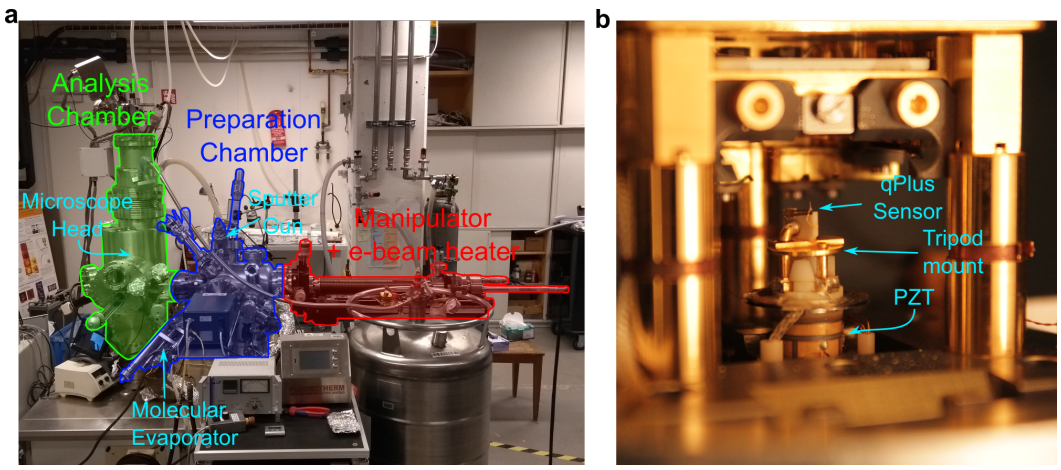

Figure 2.6: ***LT-UHV System with qPlus STM/AFM sensor.*** ***a,*** *The analysis chamber (green) houses the cryostats for liquid nitrogen and helium, as well as the microscope head.* ***b,*** *Microscope head with PZT and qPlus sensor mounted on the tripod for contacting the electrical contacts.*

Precise high resolution STM and AFM measurements require ultra clean conditions of the environment for the sample preparation as well as low temperatures and pressures for the sensor to be able to approach the surface as close as possible with minimal noise level therefore further increasing resolution. In this study a microscope build by Scienta Omicron GmbH[1] with a combined STM/AFM sensor in the qPlus configuration [97] in ultrahigh vacuum (UHV) and at low temperatures (LT) is used. The sensor and sample are kept at $T = 4.8$ K whereas the rest of the system is at room temperature. To realise this temperature discrepancy and minimize pollution during measurements the system is divided into two chambers, the analysis chamber (AC, shown in Fig. 2.6**a** in green) with pressures of $p_{\mathrm{AC}} \sim 10^{-12}$ mbar and preparation chamber (PC, $p_{\mathrm{PC}} \sim 10^{-10}$ mbar, shown in Fig. 2.6**a** in blue) separated by a manual gate valve. The samples can be transferred with the manipulator shown on the far right of Fig. 2.6**a** in red.

Preparation Chamber. The PC, highlighted in Fig. 2.6**a** in blue, is pumped by a combination of scroll-prepump, turbo-pump, ionic pump and titanium-sublimation pump (TSP) that results in a base pressure of $p_{\mathrm{PC}} \sim 10^{-10}$ mbar. It is used to clean the samples, evaluate the evaporation rate of molecules sublimated from a molecular powder and evaporate the molecules to be investigated onto the sample. The samples are cleaned in the PC with a sputter-gun by ion-sputtering with Ar^{+}-ions and thermal annealing directly on the manipulator (red), as discussed later (Chapter 2.3). The molecules are evaporated using a Knudsen cell from Kentax GmbH[2] (molecular

[1] https://scientaomicron.com/en
[2] https://www.kentax.de

evaporator) and the evaporation rate checked with a quartz-microbalance (QMB).

Analysis chamber. Measurements are performed at a pressure of $p_{\mathrm{AC}} \sim 10^{-11}$ mbar in the analysis chamber (Fig. 2.6**a**, highlighted in green) that hosts N_2 and H_2 cryostats for cooling the sample and microscope head to $T = 4.8$ K. The pressure is realized by the pumps of the PC as well as a second set of ionic pump and TSP. Furthermore the low temperature of the cryostat bind additional atoms in the AC. In the front a wobble stick is used to transfer samples from the manipulator to a carousel, for sample and sensor storage, and into the microscope. The low temperature is realised by use of a two step system, that is visible in Fig. 2.6**b** in the form of gold walls. The outer cryostat is connected to a reservoir that is filled with liquid nitrogen ($T_{\mathrm{N_2}} = 77$ K), whereas the reservoir of the inner cryostat is filled with liquid helium at a temperature of $T_{\mathrm{He}} = 4.25$ K. The discrepancy between T_{He} and T_{AC} is caused by heat transfer from microscope head. The system stays at constant low temperature for 17 hours before it has to be refilled again. The microscope head that is situated in the inner cryostat is dampened by springs that can be locked to transfer samples and sensors and an eddy-current damping system to minimize vibrations and facilitate high resolution. The microscope is operated by a Nanonis RC5 controller from Specs GmbH[3] along with an in-house build controller to drive the stepmotor used for the coarse approach of the sensor onto the sample as well as for the fine control of the tip using the PZT.

Fast entry lock. To introduce samples, sensors and metal-evaporators into the system, a fast entry lock (FEL) is used connected to the PC. It is pumped by a pre-pump/turbo-pump combination and reaches $p_{\mathrm{FEL}} \sim 10^{-7}$ mbar. FEL and PC are separated by a gate valve.

2.3 Preparing Ag and Au samples

In the experiments, two metals, purchased from MaTeck GmbH[4], were used as substrate for the self assembled network (Chapter 3) and polymerization reactions (Chapters 4 and 5), a silver single crystal ($Ag(111)$) and a gold single crystal ($Au(111)$) respectively, both with a [111] surface direction. Both samples were cleaned by repeating cycles of Ar^+-ion sputtering, for $\Delta t_{\mathrm{sputter}} = 10$ mins at a partial pressure of $p \approx 5 \cdot 10^{-6}$ mbar, and subsequent thermal annealing via e-beam heater for $\Delta t_{\mathrm{anneal}} =$ 15 mins. For the $Ag(111)$ sample the annealing was performed reaching a surface temperature of $T_{\mathrm{Ag}} \approx 500$ ℃. The $Au(111)$ sample was annealed at a temperature of $T_{\mathrm{Au}} \approx 490$ ℃.

For sputtering, an ion gun was used (schematic shown in Fig. 2.7**a**). The introduced Ar-gas with a partial pressure of $p \approx 5 \cdot 10^{-6}$ mbar is ionized and forms a plasma inside the coil. The ions of the plasma are subsequently extracted by a pinhole-anode, collimated by electric and magnetic lenses and accelerated onto the sample surface with

[3]https://www.specs-group.com/specs/products/
[4]https://www.mateck.com

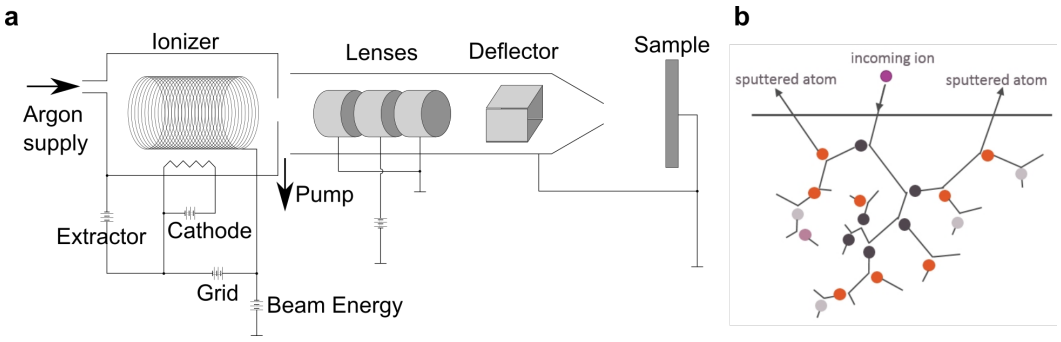

Figure 2.7: ***Sample cleaning by ion sputtering.*** ***a****, Schematic of a sputter gun used for the cleaning.* ***b****, Collision cascade created by elastic scattering of the incident* Ar^+ *[104]*

a kinetic energy of $E_{\text{kin}} = 1$ keV. Upon arriving at the sample the accelerated ions impact the surface, are reflected and start collision cascades (Fig. 2.7**b**) by transferring kinetic energy to the surrounding atoms. Ultimately, if the kinetic energy transferred to the surface atoms exceeds the binding energy of the surrounding atoms, they desorb from the sample leaving vacancies and defects in the surface.
The sample, cleaned by ion sputtering and leaving behind a rough surface is annealed at high temperatures to promote surface diffusion of metal atoms, evening out defects and creating large monoatomic terraces. The annealing is performed by directing a beam of electrons onto the back of the sample, extracted from a coil underneath the sample-holder.

2.3.1 Silver single crystals: fcc structure and surface state of Ag(111)

Silver has a face-centered-cubic (fcc) bulk crystal structure with the [111] surface orientation a closely-packed hexagonal geometry. The step height from one layer to the next is $\Delta h_{\text{Ag}} \approx 230$ pm. A clean surface with an extended terrace and two step edges can be seen in Fig. 2.8**a**. Along the lower step-edge in the bottom-right corner two defects can be spotted, pinning this particular edge in place in return hampering edge diffusion during the annealing process.
The surface is additionally characterized by a Shockley-like surface state [105] (SS) at $E_{\text{SS}} = -63$ meV. The unbound electrons at the surface create a 2D-electron gas that is confined between the vacuum and the bulk band-gap with the energy band created by the 2D-electron gas not crossing the Fermi level E_{F}. The effect of the 2D gas is only visible when scattering surface electrons at adsorbates, defects and step-edges. Fig. 2.8**b** pictures a close-up of the clean $Ag(111)$ surface with defects (green arrow) and adsorbed CO-molecules (blue arrow). The surface state is reflected by these obstacles and creates a standing wave pattern in close proximity that can be seen.

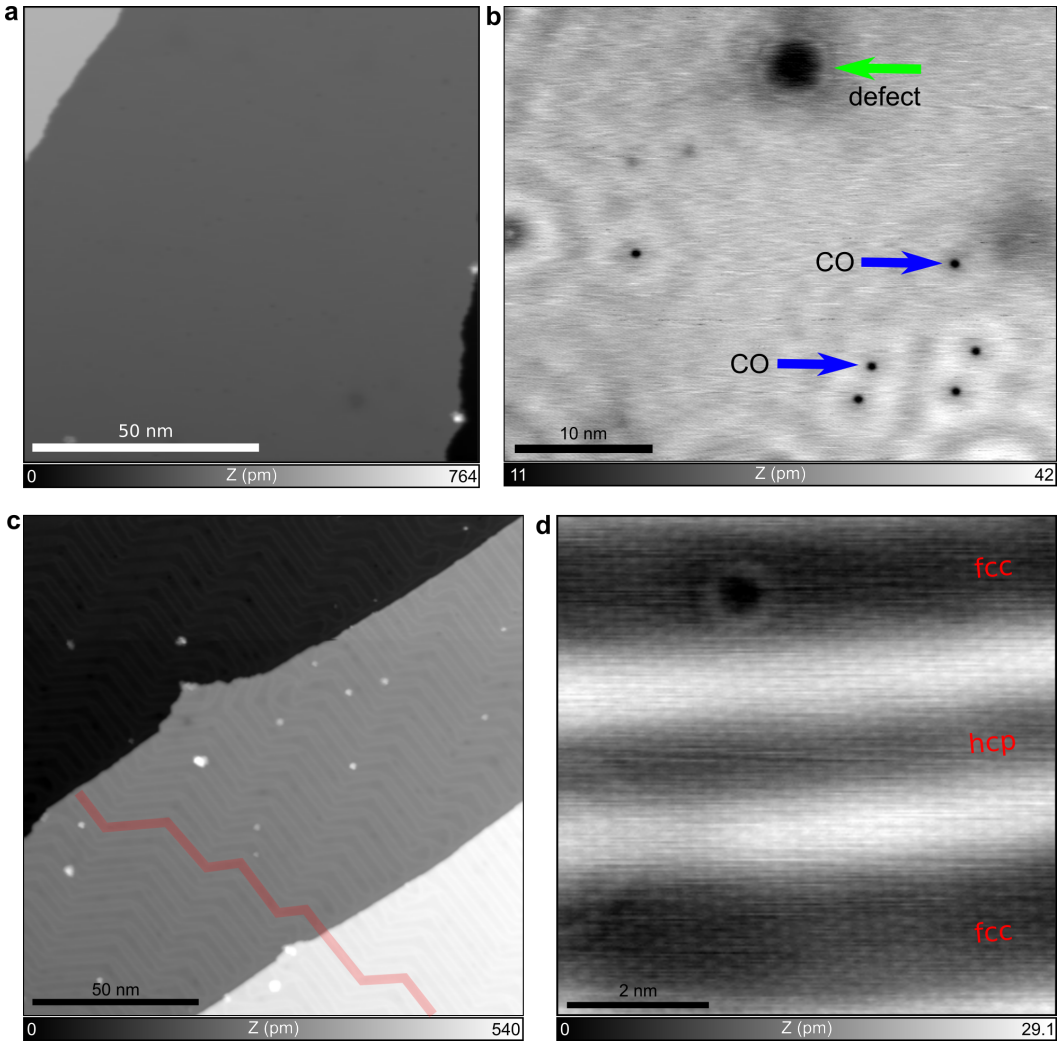

Figure 2.8: ***The pristine Ag***(111) ***and Au***(111) ***surfaces.*** ***a,*** *STM measurement of the Ag*(111) *surface showing two step edges.* $(I_{\text{setpoint}} = 1\ \text{pA}, V_{\text{Bias}} = -1\ \text{V})$. ***b,*** *Detailed view of the surface wit the surface state electrons being reflected on adsorbed CO molecules* $(I_{\text{setpoint}} = 1\ \text{pA}, V_{\text{Bias}} = -20\ \text{mV})$. ***c,*** *STM measurement of the Au*(111) *surface showing several step-edges along with a screw dislocation.* $(I_{\text{setpoint}} = 1\ \text{pA}, V_{\text{Bias}} = -100\ \text{mV})$ ***d,*** *Detailed view of the surface reconstruction.* $(I_{\text{setpoint}} = 1\ \text{pA}, V_{\text{Bias}} = -10\ \text{mV})$

2.3.2 The Gold surface and its Au(111) surface reconstruction

Similar to silver, the bulk gold is a fcc crystal with a hexagonal surface geometry in the [111] plane (visible in Fig. 2.8**c**). The step height is $\Delta h_{\text{Au}} \approx 230$ pm as well, due to the similar size of the atoms (Au: $r_{\text{vdW}} = 166$ pm, Ag: $r_{\text{vdW}} = 172$ pm). As can be seen in Figs. 2.8**c** and **d**, $Au(111)$ has a meandering surface reconstruction that is created by saturation of dangling bonds of the surface atoms to minimize energy. The surface reconstruction roughly follows the $[11\bar{2}]$ direction, going from top left in Fig. 2.8**c** to the bottom-right (highlighted in red). The surface reconstruction is also

visible in Fig. 2.8**d** in the form of white horizontal stripes.
The surface reconstruction also has an impact on the crystal structure on the surface. The valleys in between the stripes are alternating between an fcc structure in the wider part, and hexagonal-closed-packed (hcp) in the narrow space between two ridges (annotated in Fig. 2.8**d**).

2.3.3 Molecular evaporation

The molecular powders are evaporated onto the surface in UHV by physical vapor deposition (PVD) [106] in the form of molecular beam epitaxy (MBE) with a Knudsen Cell (TCE-BSC, Kentax UHV[5]) [107, 50]. The powders are heated in a quartz crucible using a resistive heater to their respective sublimation temperatures, previously determined by means of a QMB. The sublimated molecules are focused by a shutter with a small hole giving precise control over the layer thickness. The molecular beam is directed onto the cleaned pristine sample where the molecules adsorb on the surface. The evaporation temperatures for each molecule, determined beforehand with a QMB, is listed in Tab. 2.1.

2.3.4 Polymerization by thermal annealing

Polymerization of the precursors is achieved by on-surface Ullmann-coupling through, as in the cleaning step of the surfaces, thermal annealing of the sample. The Ullmann-polymerization with *Br*-terminated precursor molecules is a two-step on-surface reaction [62].
Upon annealing a coordination bond between *Br* atoms of the molecules and surface metal atoms is created, mediated by lone-pair electrons of the *Br* (Fig. 2.9 step I). When provided with sufficient energy, *e.g.* by thermal annealing, the *Br* is cleaved from the molecule, forming a *Mol-M-Br* complex (step II) that dissociates into *Mol*• radicals with an unsaturated bond (step III). With the *Br*• of another precursor Br_2 molecules are formed. Two *Mol*• radicals can finally form a dimer (step III $\rightarrow$ IV). The excess charge of the molecules when forming the dimer is compensated by the positively charged metal substrate. This process is performed as long as precursor molecules are present that can form *Mol*• radicals.
The Br_2 molecules from the polymerization reaction either stay adsorbed on the surface, coordinating along the polymers, defects and step-edges or if provided with enough energy desorb from the surface.

[5] www.kentax.de

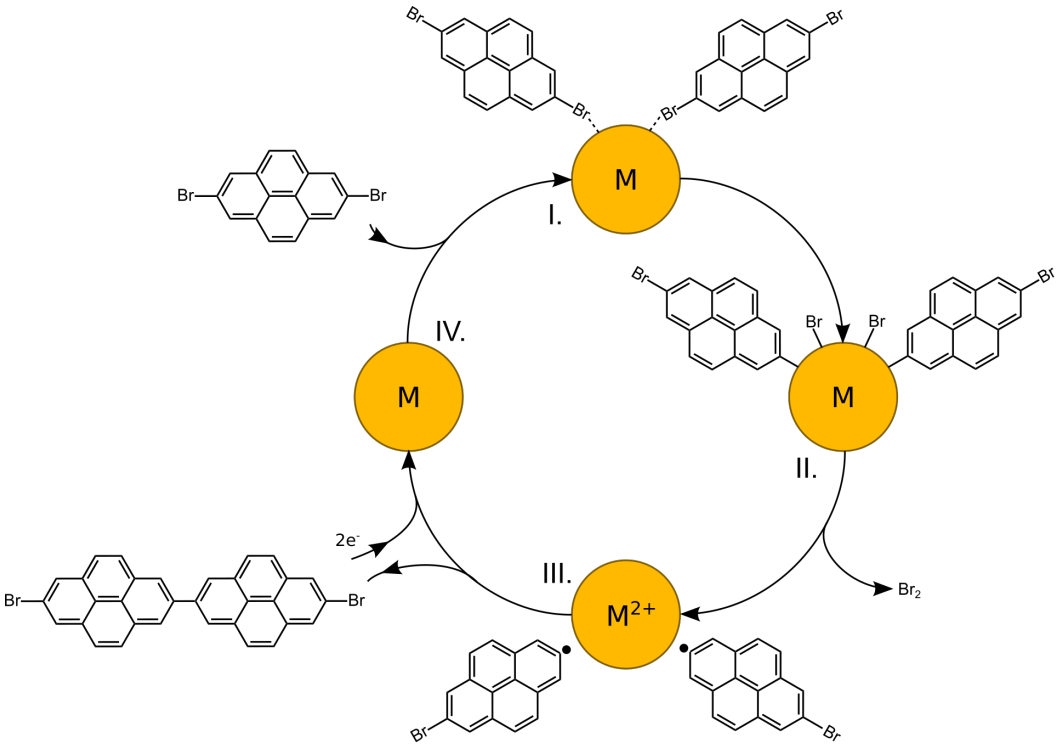

Figure 2.9: ***Ullmann-polymerization by the example of*** $2,7$***-dibromopyrene.*** *Precursor molecules bind to a surface atom at their Br terminated end (I). The Br atoms are cleaved from the precursors (II) and either desorb or diffuse on the sample. Finally a chemical bond is created between the remaining precursor radicals, forming a dimer (III → IV).*

2.4 Tip preparation for high resolution STM/AFM-imaging at LT

Before inserting the sensors into the microscope head it is advisable to sharpen the tips since the initial tip apex is not small enough for high resolution imaging (see Fig. 2.10**a**). This can be done by focussed ion beam (FIB) milling using *Ga*, *Ne* or *He* ions. The beam of high energy ions is able to remove atoms from the target by impacting into the surface transferring energy in inelastic collisions to the surrounding surface atoms that are then able to desorb. In contrast to ion sputtering with a sputter gun the beam from FIB is more controllable due to being highly collimated.
The sharpening of the chemically etched tips is performed top down from the tip of the sensor. The result is shown in Fig. 2.10**c** in the bottom area of the image. The tip was first milled from outside to inside leaving the inner core untouched. The radius of the milling was then subsequently reduced as well as the milling depth resulting in a tip apex of $R \approx 15$ nm.
During measurements it can become necessary for the tip to be sharpened again due to blunting of the apex. Two methods can be used to re-prepare the tip, first tip indentation and second bias pulse. For tip-indentation the tip is pushed into the

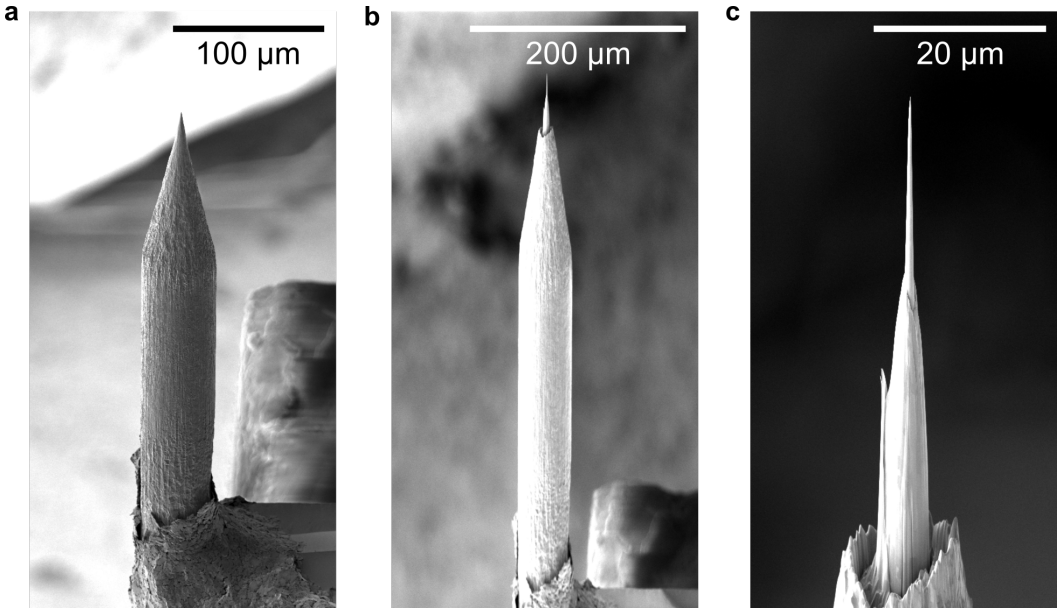

Figure 2.10: ***Scanning electron microscopy images of sensor tips. a,*** *Before and* ***b,*** *after ion milling. The tip apex is drastically reduced in the process.* ***c,*** *Detailed view of the tip apex with the concentric milling areas dividing the tip.*

surface of a clean spot of the sample and subsequently retracted. During indentation any adatoms and molecules are transferred onto the surface and are adsorbed. Upon retraction the atoms of the tip will rearrange when the contact to the surface is broken creating a clean and sharp tip. For the second method, a short bias voltage is applied between tip and sample, potentially blasting adatoms and molecules from the tip, and additionally reshaping the tip. The downside of both methods lies in the destruction of the surface for the indentation and in blasting fragments from the tip onto the surface in the tip vicinity.
The resolution of AFM can even be further enhanced to subatomic resolution by picking up a carbon-monoxide molecule (CO) from the surface. This reduces the tip apex to the size of a single atom, minimizing F_{vdW} and F_{el}, whereupon the tip-sample distance can be further reduced, enhancing the sensitivity to F_{chem}. This method enables AFM to image intramolecular bonds [108] as pictured in Figs. 2.11**c** and **d**, determining the adsorption geometry of molecules [18], the bond-order of aromatic molecules [109] and even ascertaining the charge-state of an atom in a molecule [21].

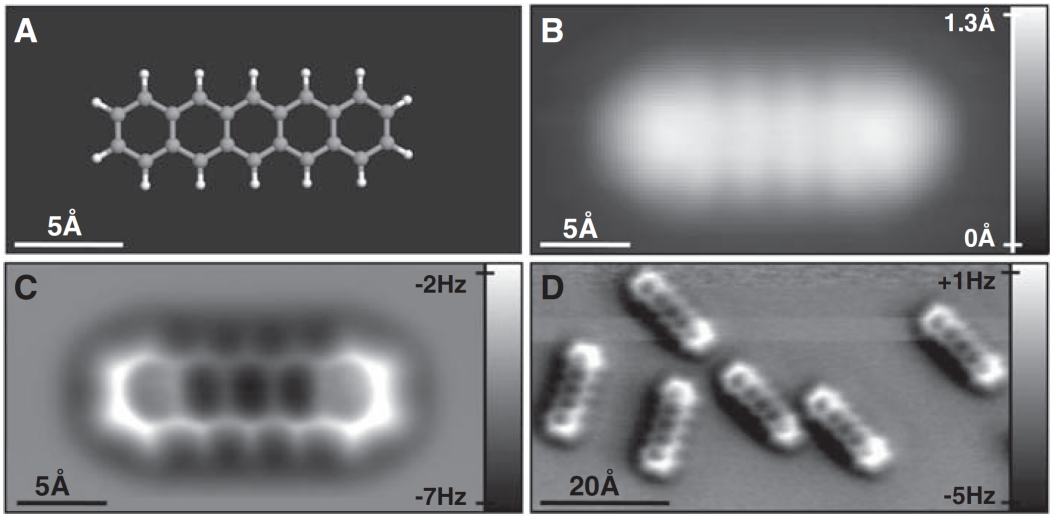

Figure 2.11: ***CO-AFM imaging of Pentacene molecules on Cu***(111)***.*** ***a,*** *Ball-and-stick representation of the Pentacene molecule.* ***b,*** *STM image of a single Pentacene molecule.* ***c-d,*** *FM-AFM constant height measurements of Pentacene molecules with CO-modified tip. (Reprinted with permission from Science [108])*

2.5 Molecules for assemblies and polymerizations

Molecule	T_{evap} (℃)	Molecular weight ($^{g}/_{mol}$)
2,7-dhp	125	234.25
2,7-dbp	110	360.05
1,6-dbp	135	360.05
2,7-cpaa	135	384.07

Table 2.1: ***Overview of molecules used in the experiments.*** *Evaporation temperatures along with the molecular weight.*

The molecules used as precursors, listed in Tab. 2.1 and Fig. 2.12, are aromatic organic molecules based on benzene-rings that are capable of π-electron conjugation [110]. Here adjacent carbon atoms bonded by a σ-bond share valence electrons due to overlap of the p-orbitals of sp^2-hybridized carbon atoms forming a π-bond, resulting in a double bond between the two atoms. In a system of alternating sequences of single- and double bonds the overall energy of the molecule can be lowered by delocalizing π-electrons over the p-orbitals of neighbouring atoms in the sequence increasing the stability of the molecule drastically.

2.5.1 2,7-dihydroxypyrene

In the family of pyrene based precursor molecules, *2,7-dihydroxypyrene* (*DHP*) is the only molecule used without halogen substitutes but with hydroxyl-groups in para-positions. This firstly prevents polymerization of the molecules and secondly paves

the way for coordinated hydrogen-bonds between monomers. A Kekulé-drawing of the molecular structure is depicted in Fig. 2.12**b**. The four fused benzene rings form a geometrical diamond-like structure with a fully conjugated π-electron system delocalized over the rings. As can be seen from the HOMO in Fig. 2.12**b** the oxygen atoms join the conjugation of the extended π-system, injecting electrons into the aromatic rings, compared to the pure pyrene molecule (Fig. 2.12**a**). The LUMO on the other hand is barely changed in comparison to pyrene.

2.5.2 2,7-dibromopyrene

Substitution of the para position in the pyrene molecule to bromine (*Br*) results in *2,7-dibromopyrene* (*27DBP*), a schematic shown in Fig. 2.12**c**. Due to the high electronegativity of bromine, electrons are pulled out of the aromatic system, weakening the π-conjugation (shown in the HOMO depiction of Fig. 2.12**c**). Similar to *DHP* the LUMO of *27DBP* is unchanged in form, albeit being decreased in size. The weakening of the π-system destabilizes the molecule making it a good candidate for polymerization reactions, since the cleavage of the halogens with subsequent bond formation between two precursors restores the aromatic system and lowers the overall energy of the molecule. Providing the precursor molecules with enough energy in form of heat, *i.e.* annealing the surface with the evaporated molecules, the *Br*-atoms can be cleaved from the molecule and a simple poly-(2, 7-pyrenylene) polymer is formed.

2.5.3 1,6-dibromopyrene

In contrast to *DHP* and *27DBP*, substitution in *1,6-dibromopyrene* (*16DBP*) occurs in the ortho position resulting in a chiral molecule. Fig. 2.12**d** shows the Kekulé-drawing along with the HOMO and LUMO. As can be seen, the HOMO of *16DBP* resembles the HOMO of the pure pyrene again, only being slightly deformed in the direction of the *Br* substituents. Again as for *27DBP*, the withdrawal of electrons from the aromatic system towards the *Br* enables an easy cleavage and following polymerization.

2.5.4 2,7-dibromocyclopenta[h,i]aceanthrylene

Out of the precursor molecules used, *2,7-dibromocyclopenta[h,i]aceanthrylene* (*CPAA*) is the only one not based on pyrene. The anthracene backbone is expanded off-center by two five-member rings, with substituted *Br* in position 2 and 7. A schematic drawing along with the HOMO and LUMO of the molecule is shown in Fig. 2.12**e**. As can be seen, the HOMO is concentrated along the axis spanned by the five-member rings and the *Br*-groups. In contrast to the HOMO, the LUMO is evenly distributed over the whole molecule. Similar to the case of *27DBP* the shift of the orbitals in the direction of the halogens weakens the stabilization and energy minimization of the conjugated aromatic system, which enables the easy severing of the *Br* atoms from the precursor, resulting in a *CPAA*-polymer.

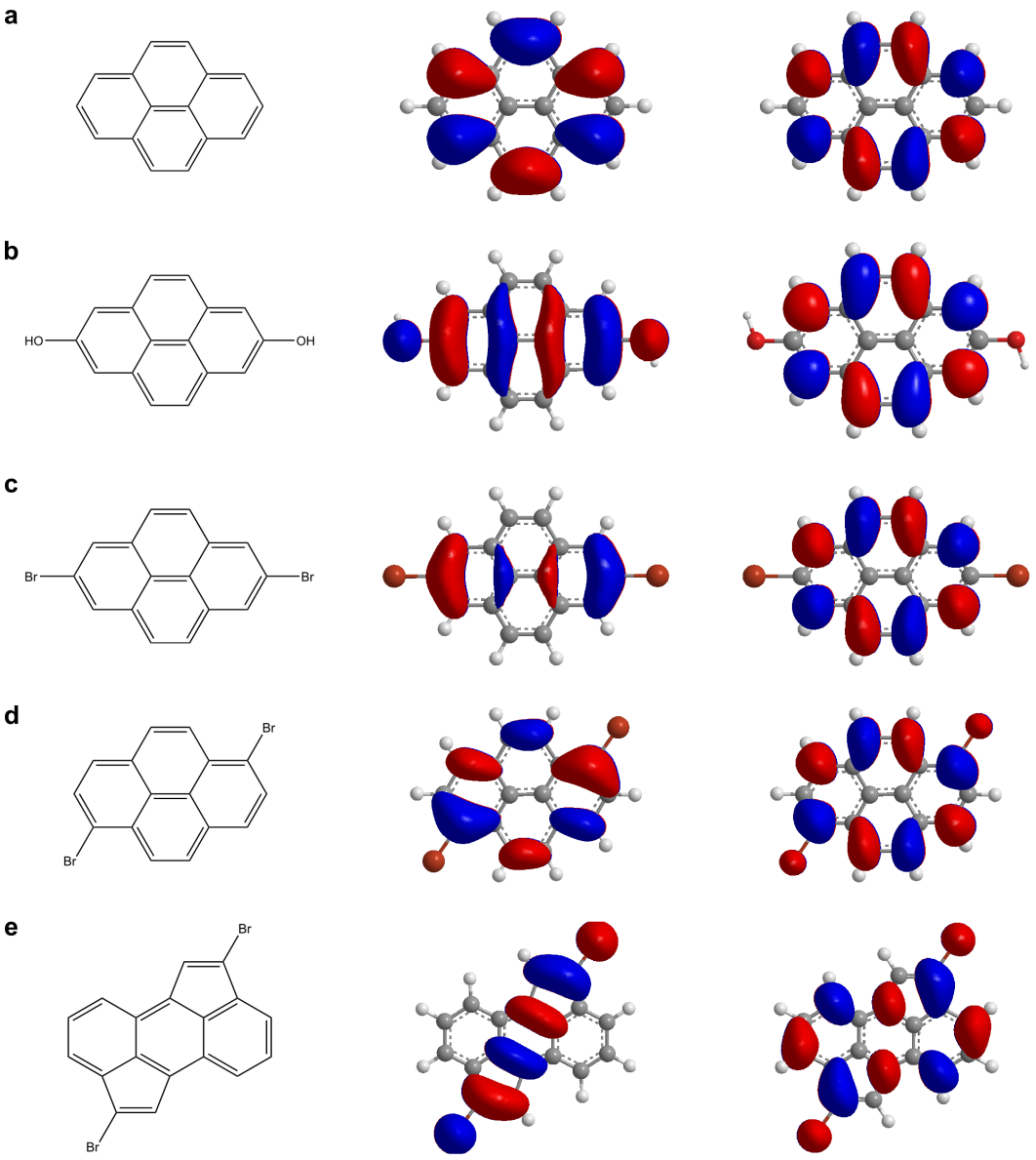

Figure 2.12: ***Kekulé-Drawing of precursor molecules along with the HOMO and LUMO.*** ***a****, pure pyrene.* ***b****, DHP.* ***c****, 27DBP.* ***d****, 16DBP.* ***e****, CPAA. (Acquired with ChemDraw 3D)*

2.6 Molecular Manipulation

2.6.1 Implementation of cryo-force spectroscopy

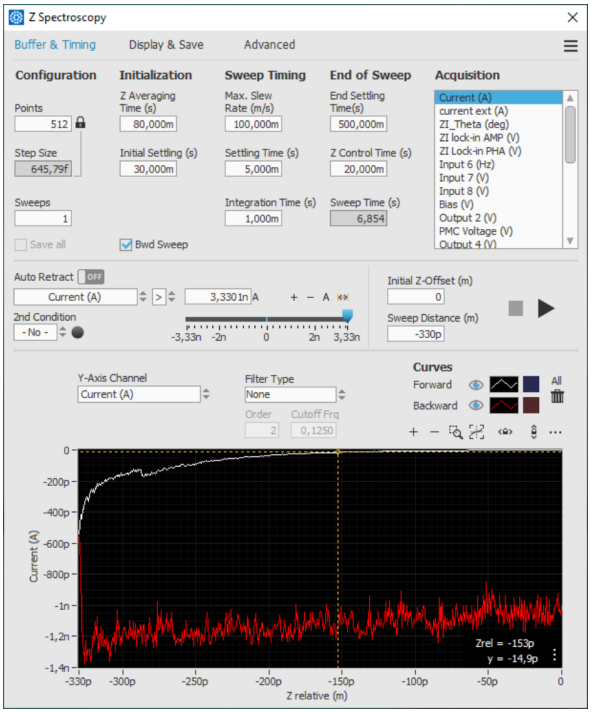

Figure 2.13: ***Nanonis z-spectroscopy tool.***

For the cryo-force spectroscopy the z-spectroscopy tool from Nanonis RC5 is used (Fig. 2.13). The sensor is oscillated at $f_0 = 26/24$ kHz (for Chapter 4 and 5 respectively) with oscillation amplitudes of $A_0 = 50$ pm and $V_{\text{Bias}} = 0$ V. For the manipulation the tip is positioned right above the last atom of the molecule and vertically approached until a sudden change in Δf is registered signaling the creation of a molecule-tip bond. The tip is subsequently retracted from the surface, peeling the molecule off the sample. The resulting pulling speeds are $v \approx 50/8.3$ pm s^{-1} with resolutions of $\approx 5.86/0.98$ pm pixel^{-1} at 5120/10240 pixels total (Chapter 4 and 5).

Part II

Experimental Results and Discussion

3

Quantum confinement in nanoporous molecular networks

Confinement of Shockley state (SS) surface electrons of noble metals such as *Ag* and *Cu* to form quantum dots (QD) has already been achieved by Crommie *et al.* in 1993 [111] through atom-by-atom manipulation into quantum corals using an STM tip. Other groups later employed self-assembled monolayers (SAM) and metal-organic frameworks (MOF) [13, 25, 57]. However, all experiments to date report on either isolated quantum dots or arrays of homogeneous confined states that form electronic bands in the LDOS by inter-dot coupling. The coupling strength and electronic structure of the confinement in the latter case has so far only been tuned via the precursor molecules of the assembly and therefore the boundaries separating the QDs. A direct control of behaviour and characteristics of the QDs has not been possible until now due to lack of precise local gating.
Here a combined STM/AFM sensor in the qPlus configuration was used to investigate the inter-dot coupling of homo- and heterogeneous quantum dot arrays (QDAs) formed by self-assembly of 2, 7-*dihydroxypyrene* (DHP) on Ag(111). The electronic structure of the QDs in two distinctly different arrays along with single electron tunneling into the confined states and inter-dot tunneling rates were determined using an AFM tip for local gating and finally compared to one another.

3.1 2,7-dihydroxypyrene on Ag(111)

The DHP precursor molecules, a schematic shown in Fig. 3.1**b**, were evaporated onto the *Ag*(111) surface in UHV conditions as introduced in Chapter 2.3.3. They assemble into two nanoporous networks, denoted as α- and β-phase. STM measurements of the α- and β-phase are respectively pictured in Figs. 3.1**c-e**.
The two phases are depicted in **c** on the same surface without intermixing with **d** and **e** showing single measurements of the respective assemblies. The α-phase can be characterized by a more dense packing compared to the β-phase judging from the detailed insights into the assemblies (Figs. 3.1**d** and **e**). The α-phase is constructed from a homogeneous array of purely hexagonal pores with lattice parameters $a_\alpha \approx 24$ Å, each

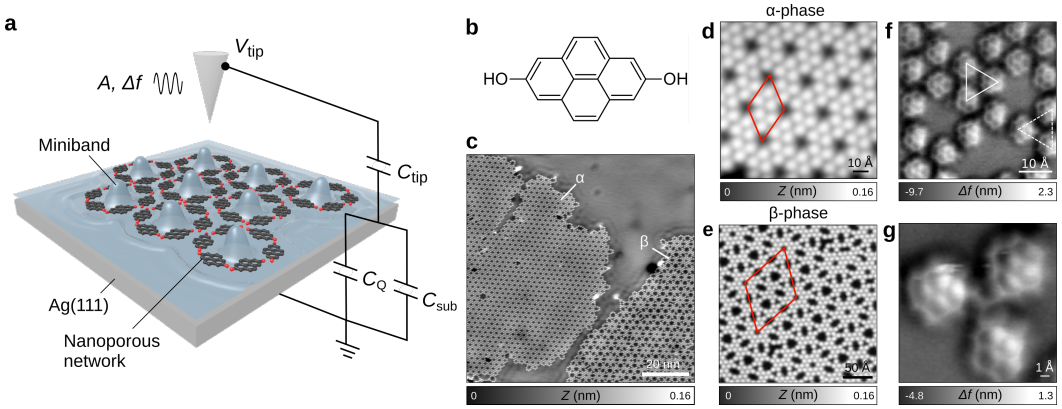

Figure 3.1: ***Mechanical coupling with an array of coupled quantum dots. a,*** *Schematic drawing of the coupled tip-sample system. The tip oscillates over the nanoporous molecular network that confines the surface electrons.* C_{sub} *and* C_{tip} *denoting substrate and tip capacitances respectively,* C_{Q} *the quantum capacitance resulting from the "miniband" of the QD-array.* ***b,*** *Structural drawing of the* $2,7$*-dihydroxypyrene (DHP) molecule.* ***c,*** *STM measurement depicting the* α*- and* β*-arrays self-assembled from DHP molecules on* $Ag(111)$*.* ***d-e,*** *Detailed images of* α*- and* β*-assemblies. (*$I_{\mathrm{Setpoint}} = 1$ pA, $V_{\mathrm{Bias}} = -80$ mV*)* ***f-g,*** *CO-tip modified AFM images of six- and nine-member pores along with a trimer (dashed line in* ***f****).*

pore with diameter $d_6 \approx 7.5$ Å consisting of six DHP molecules with a separation of two molecules between pores ($d_{\mathrm{wall}} \approx 10$ Å). The β-assembly on the other hand is comprised of three-, six-, eight- and nine-member cavities forming an intricate hexagonal network with lattice parameter $a_\beta \approx 87$ Å.

Evaluation of the bonding motif of the assemblies is performed by constant height FM-AFM with a *CO*-terminated tip (chapter 2.4). The α-assembly of hexagonal six-member cavities is governed purely by *C-H··O-C* hydrogen bonds between peripheral hydrogens in ortho position and hydroxyl-groups of neighbouring precursor molecules, forming trimers with $\pm 4°$-rotated units (highlighted by the solid triangle in Fig. 3.1**f**). The six-member cavities in the β-assembly show a similar bonding pattern to the ones in the α-array. However all other moieties, the three-, eight- and nine-unit pores, most likely form due to deprotonation of the hydroxylic end-groups of DHP resulting in either metal-ligand interactions with the metal surface (Fig. 3.1**g**) with the silver adatom in the middle of the three molecules, or hydrogen bonds between $C\text{-}O^- \cdots H\text{-}C$. Nevertheless the primary pattern that leads to the different pores and the high crystallinity of the assembly is a trimer of three molecules, shown in dashed lines in Fig. 3.1**f**.

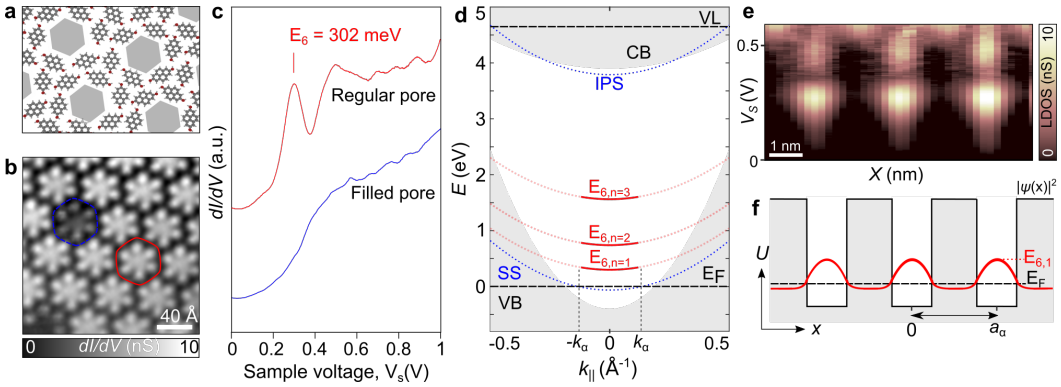

Figure 3.2: ***Electronic properties of the α-quantum dot array.*** ***a,*** *Schematic model of the α-array.* ***b,*** *$dI/dV(X,Y)$ map at $E_6 = 302$ meV illustrating the confinement of surface electrons in each pore as bright features (red highlight) in contrast to extinguished pores resulting from trapped CO molecules inside the pore (blue highlight).* ***c,*** *Differential conductance point spectra ($dI/dV(V)$) measured in the center of the red and blue highlighted pores in* ***b****. Resonance peak at $E_6 = 302$ meV showing the discrete energy level of the QDs.* ***d,*** *Illustration of the surface projected electronic band structure of the α-array on $Ag(111)$. The Shockley state (SS, dashed blue line) at $E_0 = -68$ meV and image potential state (IPS, dashed blue line) at $E_{\mathrm{IPS}} = +3.9$ eV are in the band gap between lower and upper sp-band of the $Ag(111)$ surface (at $E = -0.4$ eV and $E = 3.9$ eV respectively). The α-QDA induces an energy band at $E_6 = +0.3$ eV.* ***e,*** *$dI/dV(X,V)$ cross section acquired along three hexagonal pores of the α-QDA.* ***f,*** *Kronig-Penney model of the periodic potential $U(X)$ of the α-array. The wave-function $|\psi|^2$ corresponding to the lowest eigenenergy is represented by the red line.*

3.2 Electronical properties of the homogeneous α-quantum dot array

Using STS the electronic properties, representing the LDOS, of the QDA is investigated. Fig. 3.2**c** shows the spectra measured in the center of a hexagonal pore in the α-array, highlighted in red in Fig. 3.2**b**. A resonance peak at $E_{\mathrm{i=6}} = +302$ meV can be observed (i representing the amount of sides of the pore), that is not present in the pristine $Ag(111)$ surface state (SS $Ag(111)$: $E_{\mathrm{SS}} = -68$ meV). This resonance peak is a result of the surface electrons being confined into the cavity. Bright contrasts delocalized over the whole cavity can be spotted when acquiring dI/dV maps at E_6 (Fig. 3.2**b** red hexagon). Additionally highlighted in blue in Fig. 3.2**b**, some pores appear dark compared to the surrounding cavities, a result of trapped CO molecules in the pore. The dI/dV spectra measured in the center of these pores, shown in Fig. 3.2**c** in blue, exhibit no resonance peak in the scan-range, a result of either the absence of confined electrons due to trapped CO or a shift to higher energies. These dark pores however are only few, amounting to only 1% compared to the pristine cavities.
The electronic band structure of the α-array can be approximated by two-dimensional hexagonal cavities separated by infinite potential walls and parabolic dispersion in

k-space. The energy levels $E_{6,\mathrm{n}}$ can be expressed as:

$$E_{\mathrm{n}} = E_0 + \frac{n^2\hbar^2k^2}{2m^*} \tag{3.1}$$

with $E_0 = -0.068$ eV the lowest energy of the SS band, $m^* \approx 0.47\ m_0$ the effective mass of the confined electrons according to Angular resolved photo-electron spectroscopy (ARPES) measurements on similar porous systems [57] and n the integer denoting the electronic band. The projected band structure according to Eq. 3.1 is plotted in Fig. 3.2**d**, with $E_{6,\mathrm{n}=1-3}$ in comparison to the valence band (VB), the SS, the conduction band (CB) and the image potential state (IPS) of $Ag(111)$. The energy of the first confined state can therefore be approximated as $E_{6,1} = +0.49$ eV, being considerably larger than the value obtained in the experiment ($E_{6,\mathrm{exp}} = +0.302$ eV). In our ansatz however we assumed infinite walls separating the QDs, which does not reflect the experimental conditions, with the walls being finite and approximated as ~ 0.75 eV. The $E_{6,n}$ are delocalized in k-space between $\pm k_\alpha$ with $k_\alpha = \pi/a_\alpha = 0.08$ Å^{-1}. The position of the IPS at $E_{\mathrm{IPS}} = +3.9$ eV is extracted from Gundlach oscillations recorded by STS (Fig. 3.3).

The high purity and reproducibility of the states in the α-assembly is demonstrated in

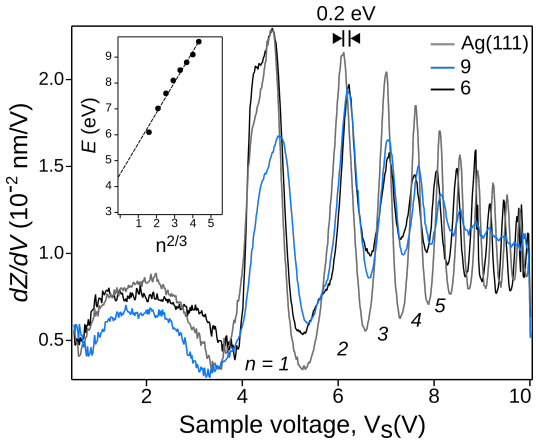

Figure 3.3: ***Field emission resonance tunneling spectra,*** *for six- and nine-member pores in the β-assembly as well as for the pristine $Ag(111)$ surface.*

Fig. 3.2**e** that depicts experimental LDOS(X, V) measurements across three neighboring pores. The α-QDA can therefore be modelled in a Kronig-Penney (KP) potential as a series of identical quantum wells of same size, coupled through the barrier wall (Fig. 3.2**f**). As a result of the strong coupling between the QDs the wavefunctions $|\psi|^2$ overlap and possibly create an "empty" miniband.

3.3 Electronical properties of the heterogeneous β-quantum dot array

As compared to the α-array, the β network consists of a heterogeneous assembly of varying pore size, ranging from three- pores, to six-, eight- and nine-membered cav-

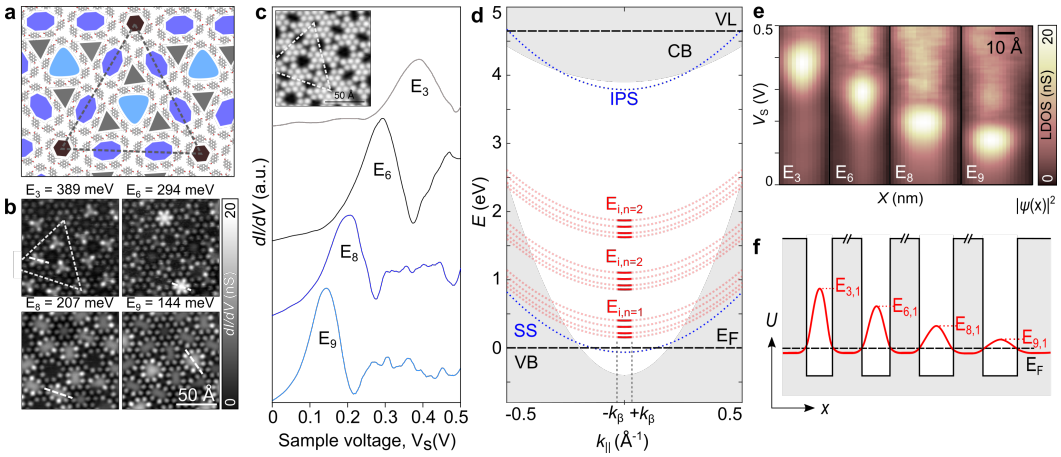

Figure 3.4: ***Electronic properties of the*** β***-quantum dot array.*** ***a,*** *Model of the assembly forming four types of cavities, three- (gray), six- (black), eight- (dark blue) and nine-membered (light blue). The dashed triangle showing the same structure as in b and c.* ***b,*** dI/dV*-maps at the eigen-energies of the cavities.* ***c,*** dI/dV *point-spectra acquired at the center of each cavity-type, resonance peak positions at* $E_3 = 389$ *meV,* $E_6 = 294$ *meV,* $E_8 = 207$ *meV and* $E_9 = 145$ *meV respectively. Inset showing the STM topography measurement corresponding to* dI/dV*-maps in b.* ***d,*** *Projected electronic band structure of the* β*-assembly.* ***e,*** $LDOS(X, V)$ *cross-section measurements along the dashed lines of b highlighting the highly localized confined states.* ***f,*** *KP-model of the wave-function overlap in a series of different pores.*

ities (*i.e.* $i = 1, 6, 8, 9$). They are highlighted in a schematic model of the assembly in Fig. 3.4**a**, in gray, black, dark blue and light blue respectively. Four different eigen-energies $E_{\mathrm{i},1}$ resulting from the different confinement area can be extracted from dI/dV measurements in the center of each pore. As depicted in Fig. 3.4**c** these eigen-energies are $E_{3,1} = 389$ meV for the three-member, $E_{6,1} = 294$ meV for the hexagonal six-membered, $E_{8,1} = 205$ meV for the eight-member and $E_{9,1} = 145$ meV for the nine-membered cavity respectively. LDOS maps at these eigen-energies are shown in Fig. 3.4**b** revealing bright contrasts in the corresponding pores and highlighting the spatial confinement of the wave-functions. In contrast to the α-array ($E_6 = +302$ meV) the energy of the hexagonal pores in the β-assembly is lowered by $\Delta E \approx 7$ meV. This is a result of the surface electrons not being confined as strongly as in the homogeneous α-assembly (despite the domain walls being identical with a width of two molecules) due to the influence of the eight-membered pores ($E_{8,1} = 205$ meV) surrounding this hexagonal cavity (Fig. 3.4**a**). Noteworthy is the peak width of $E_{6,1}$ in the β-array (~ 120 meV) that is much wider compared to $E_{6,1}$ of the α-assembly (~ 60 meV), further suggesting a weaker confinement and higher probability for electron tunneling between cavities in the β-phase. Analogous to the α-array, Fig. 3.4**d** shows a schematic of the band structure of the β-assembly with the four $E_{\mathrm{i},1}$ eigen-energies of the cavities above E_{F} ranging from $+140 - 400$ meV and situated in k-space between $\pm k_\beta = \pi/a_\beta = 0.03$ Å^{-1} (with $m^* = 0.47\ m_0$). A representation of the $\mathrm{LDOS}(X, V)$ in form of a cross-section is pictured in Fig. 3.4**e** showing the confined localization of

the ground states, with Fig. 3.4**f** depicting the KP-model of the wave-function $|\psi|^2$ as a series of potential wells getting wider with increasing pore dimensions.

3.4 Mechanical dissipation

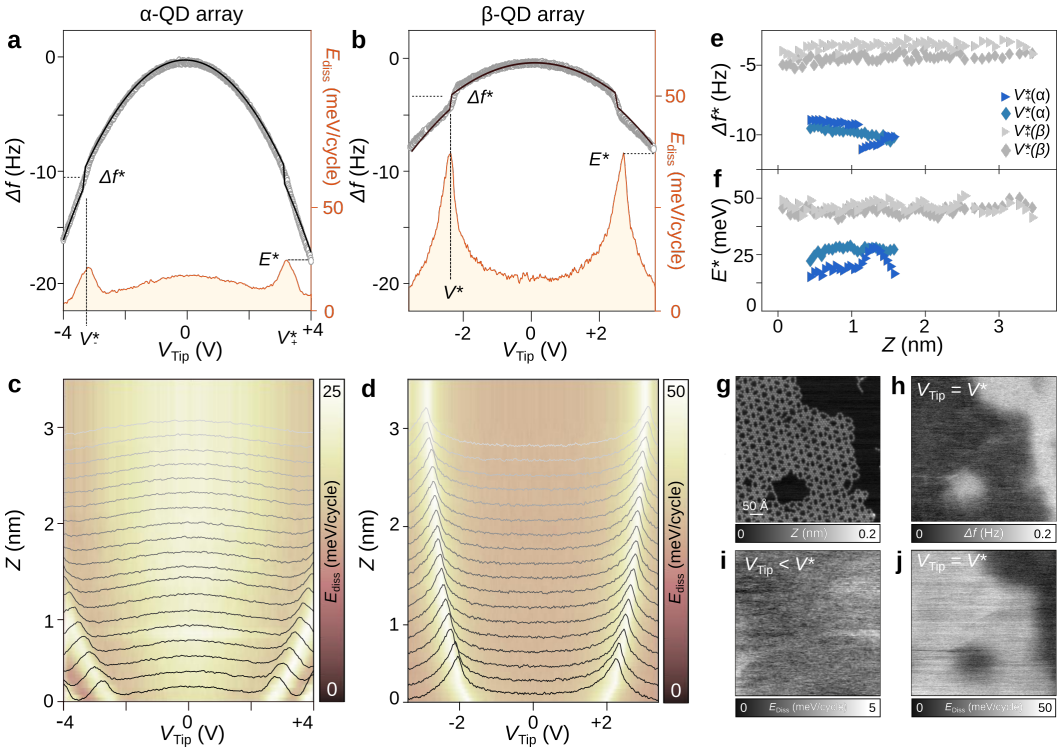

Figure 3.5: ***Mechanical dissipation of both QDAs using electrostatic force spectroscopy.*** ***a-b,*** *Single-point measurement of force $\Delta f(V)$ (gray) and corresponding $E_{\mathrm{Diss}}(V)$ (orange) for the α- and β-QDAs. Relative tip-sample separation is $z = 0.36$ nm. Positions of jumps Δf^* are associated with dissipation peaks E^* at tip voltage V^* (black graph: $\Delta f(V)$ fit using the quantum capacitance model).* ***c-d,*** *$E_{\mathrm{Diss}}(V, z)$ versus tip-sample separation Z for the α- and β-QDA respectively. Sharp bright lines correspond to E^* peaks with $E_{\mathrm{Diss}}(V)$ graphs superimposed.* ***e-f,*** *Magnitudes of Δf^* and E^* for increasing tip-sample separations (z). α/β-QDAs are marked in blue/gray triangles and diamonds respectively. Triangles/diamonds correspond to positive/negative V^*.* ***g,*** *STM topography of the β-QDA.* ***h,*** *Δf and* ***j,*** *E_{Diss} measurements of the same area as* ***g*** *at tip voltage V^*, showing mechanical dissipation above the molecular array.* ***i,*** *E_{Diss}-map at constant-height revealing vanishing E_{Diss} for $V_{\mathrm{tip}} \neq V^*$.*

Electrostatic force-spectroscopy was used to measure the mechanical dissipation over both QDAs (Figs. 3.5**a** and **b**). The graphs depict $\Delta f(V)$ (plotted in gray) and the corresponding mechanical energy dissipation E_{Diss} (in orange) point-spectra measured over the α- and β-QDAs respectively, at a tip-sample distance of $\Delta z = 306$ pm. Clearly

visible in both measurements at threshold tip voltages $\pm V^*$ are sudden transitions in the frequency shift (Δf^*) and dissipation peaks E^*.

A model accounting for the quantum capacitance C_Q of the miniband created by

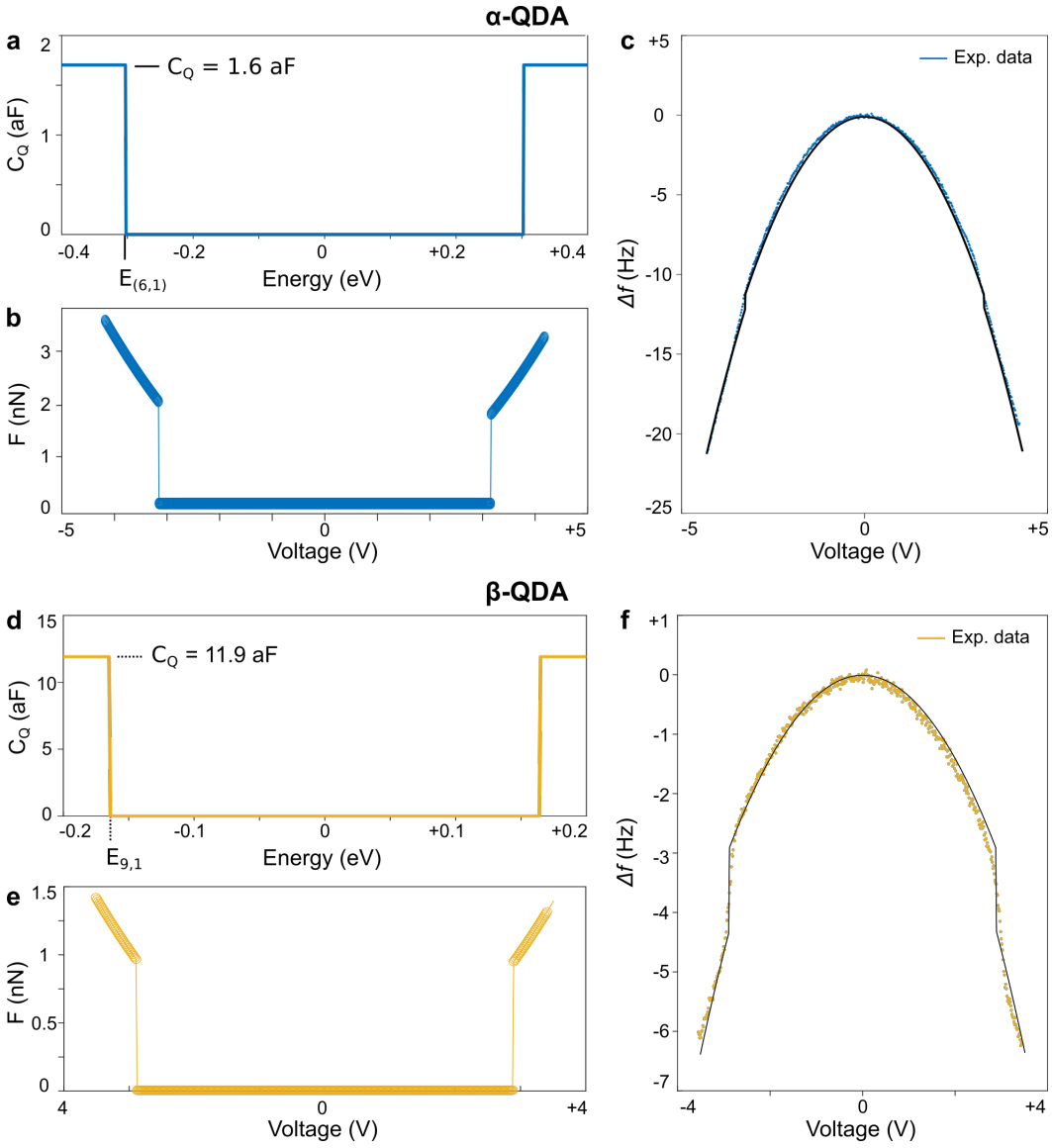

Figure 3.6: ***Quantum Capacitance extracted from*** $\Delta f(V)$ ***spectra.*** *Quantum capacitance* C_Q *for* ***a,*** *the* α *and* ***d,*** β*-QDA respectively. Heaviside function jumps at lowest energy,* $E_{6,1}$ *for the* α*-array and* $E_{9,1}$ *for the* β*-array. Step heights are* $C_{Q,\alpha} =$ 1.6 aF *and* $C_{Q,\beta} = 11.9$ aF. $F_{\text{elec}}(V)$ *for* ***b,*** *the* α *and* ***e,*** β*-QDA according to Miyahara et al. [112].* $\Delta f(V)$ *measurement and fit using the quantum capacitance model for* ***c,*** *the* α *and* ***f,*** β*-QDA.*

the QDs of both assemblies is used in conjunction with the substrate- (C_{sub}) and tip-capacitance (C_{tip}) to reproduce the acquired experimental $\Delta f(V)$ data. The quantum capacitance results from the lower levels of the LDOS near the Fermi

level E_{F} and can be expressed as [113]:

$$C_{\mathrm{Q}} = \rho(E)e^2 = \frac{m^* e^2}{\pi\hbar^2} \tag{3.2}$$

with $\rho(E) = {}^{dn}/_{dE}$ the density of states (DOS) for carrier charge e and concentration n. For metals with a two-dimensional electron gas (2DEG), the DOS is given as $\rho(E) = {}^{m^*}/_{\pi\hbar^2}$. C_{Q} is therefore not only a result of the state dispersion (m^*) being quantized but also of the tunneling between QDs. The model is shown in Figs. 3.5 **a** and **b** in black as an overlay of the experimental data, with a schematic drawing of the capacitance model in Fig. 3.1**a**.

To calculate C_{Q} a heaviside function with step at the lowest eigen-energy $\pm E_{\mathrm{i},1}$ of both α- and β-assembly is used (Figs. 3.6**a** and **d**). From the fitting of $\Delta f(V)$ (visible in Figs. 3.6**c** and **f**) the quantum capacitance C_{Q} can be extracted as $C_{\mathrm{Q}}^{\alpha} = 1.6$ aF nm^{-2} and $C_{\mathrm{Q}}^{\beta} = 11.9$ aF nm^{-2} respectively. As can be seen in Figs. 3.5**a** and **b** every sudden change Δf^* is followed by an strong increase in E_{Diss} with dissipation peaks of $E_{\alpha}^* = 20$ meV cycle^{-1} for the α- and $E_{\beta}^* = 40$ meV cycle^{-1} for the β-QDA in comparison to the undisturbed state of the sensor ($E_{\mathrm{ini}} = 15$ meV cycle^{-1}) at the contact potential difference (CPD). Plotting $E_{\mathrm{Diss}}(Z, V)$ for increasing tip-sample separations (Figs. 3.5**c** and **d** for α- and β-QDA) shows bright lines that correlate to the E^* peaks for both QDAs.
In force spectroscopic measurements, the dependency of E_{Diss} on the height above the substrate is usually attributed to C_{sub} and C_{tip}, whereas the position of $V^* = E_{i,1}\frac{C_{\mathrm{tip}}+C_{\mathrm{sub}}}{C_{\mathrm{tip}}}$ is dependent on the lowest eigen-energy $E_{\mathrm{i},1}$ and the inverse ratio of tip-capacitance to the capacitance of the measurement system (C_{tip} and C_{sub}).
According to Hudlet *et al.* [93], C_{tip} can be calculated as:

$$C_{\mathrm{tip}} = 2\pi\varepsilon_0 R \cdot \ln\left(\frac{(z - z_0) + R(1 + \sin\theta_0)}{(z - z_0)}\right) + C_0 \tag{3.3}$$

with ε_0 the vacuum permittivity, R the tip-radius, the tip apex aperture $\theta_0 = 10°$ and C_0 a constant. It is also worth noting that the position of the IPS of $Ag(111)$ ($V_{\mathrm{IPS}} = \pm 4$ V) is the limiting factor for measuring V^* which would also create additional mechanical dissipation [114]. Despite the IPS inducing mechanical dissipation, it decays swiftly with increasing tip-sample separations and therefore does not influence the E^* peaks.
For both phases, as visible in Figs. 3.5**e** and **f**, the magnitude of E^* as well as Δf^* persists over the entire measurement range of tip-sample separations, *i.e.* $\Delta z \leq 1.5$ nm for the α-QDA (blue) and $\Delta z \leq 3.5$ nm for the β-assembly (gray) respectively, as well as for both polarities of V^* (triangle for positive, diamond for negative polarity). The measured data is subsequently in opposition to works that previously reported on the Coulomb blockade of 0D-systems as in quantum dots or single molecules [115, 116, 117, 118, 119]. There, single-electron tunneling events between the confined states and the tip are the main mechanism behind the force jumps and dissipation peaks, where the signal of the dissipation is directly dependent on the tunneling

rate Γ between tip and sample and swiftly decays with increasing Δz. These tunneling events would also be visible in constant-height dissipation measurements as Coulomb-rings with the diameter changing depending on the (x, y, z) position of the AFM tip. Judging from Figs. 3.5**g-j**, no Coulomb-rings are present in neither Δf nor E_{Diss} measurements when scanning at the threshold voltages V^* (Figs. 3.5**h** and **j** respectively). The frequency shift as well as the mechanical dissipation are homogeneous over the whole assembly, changing contrast when scanning over the pristine $Ag(111)$ surface, and even vanish when scanning away from V^* (Fig. 3.5**i**). Single-electron tunneling from tip to single QDs and the consistent magnitude of E^* for large ranges of Δz can therefore be ruled out as the underlying mechanism. Instead, tunneling events between substrate and the two-dimensional confined states or inter-dot tunneling processes may be induced by the gate voltage of the tip and can be detected by force spectroscopy due to local changes of the sample capacitance.

In order to rationalize the tunneling mechanism a periodic KP potential $U(x)$ is

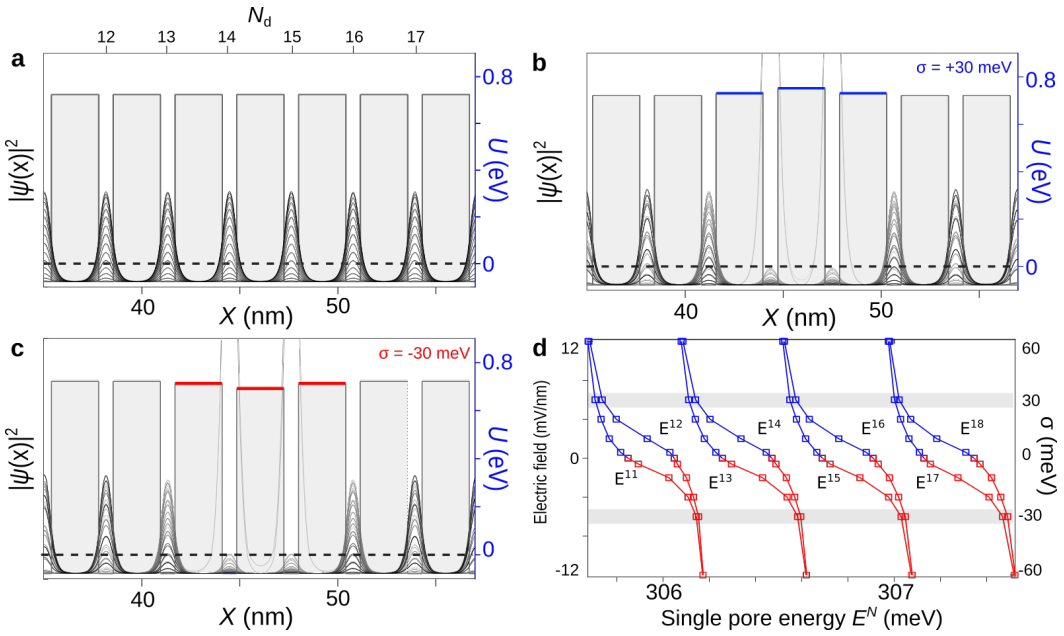

Figure 3.7: ***Local perturbation of the Kronig-Penney model.*** ***a,*** *Delocalization of the wave-functions $|\psi|^2$ of an array comprising $N_{\mathrm{d}} = 30$ QDs. The axis on the right denotes the KP potential $U(x)$ with the bottom of the wells at -0.3 eV and the top at 0.75 eV.* ***b-c,*** *Effect of the perturbation $\sigma = \pm 30$ meV above QDs 13 to 16 on the wave-functions for positive (blue) and negative (red) perturbation respectively.* ***d,*** *Evolution of eigen-energies E^N of single QDs upon perturbation σ.*

used for a 1D sequence of $N_{\mathrm{d}} = 30$ QDs with dimensions of the α-assembly. The array is then subjected to a local perturbation $\pm\sigma$ and the ground state wave-functions ψ_{n} calculated by solving the Schrödinger equation. The resulting probability density $|\psi(X)|^2$ for all QD-wave-functions is pictured in Figs. 3.7**a-c** (cropped to the middle, $N_{\mathrm{d}} = 11 - 18$) with **b** and **c** showing the probability density under the influence of the perturbation $\sigma = \pm 30$ mV. Using $m^* = 0.47\ m_0$ the mean eigen-energy is calculated

as $E_{6,1} = 0.308$ eV and in good agreement with the experimental value. The perturbation $\pm\sigma$ of the potential $U(x)$ is used as an estimation of the local electric field caused by the influence of the tip that is situated above QDs 13 to 16. In the simulation the perturbation is analogous to a polarization of the *DHP* molecules of the nanoporous networks, induced by the proximity to the electric field of the tip. Figures 3.7**b** and **c** show the resulting densities $|\psi(X)|^2$ under influence of positive (blue) and negative (red) perturbation respectively. For both polarities σ, the probability densities $|\psi_\mathrm{n}|^2$ remain delocalized yet below the perturbation (QDs 14 and 15) there is a significant decline in $|\psi|^2$. With increasing σ the confined states corresponding to $E^N_{6,1}$ are pushed towards lower energies eventually dropping below E_F initiating a charge transfer between the confinement and the electron reservoir of $Ag(111)$. This evolution of the eigen-energies influenced by σ is depicted in Fig. 3.7**d** for cavities $N_\mathrm{d} = 11 - 18$. A continuous transition from a discrete to a degenerate energy configuration of neighbouring QDs when crossing $\sigma = \pm 30$ meV, the critical perturbation analogous to a transverse electric field of 6 mV nm^{-1} marked in gray, can be observed. This degeneracy of paired neighbouring QDs can be rationalized as a quantum phase transition caused by charging of the cavities below the tip ultimately redistributing all $|\psi|^2$ across the assembly albeit the mean energy only changing by $\Delta E = \pm 0.3$ meV due to σ.
Finally, after rationalizing the mechanism, the tunneling rates $\Gamma_{\alpha/\beta}$ of the pores can be extracted [116, 120] from the dissipation energy E_Diss extracted from the measured excitation amplitude:

$$E_\mathrm{Diss} = \frac{\pi k A^2}{Q}\left(\frac{A_\mathrm{exc} - A_\mathrm{exc,0}}{A_\mathrm{exc,0}}\right) \tag{3.4}$$

$$\Gamma_{\alpha/\beta} = 4\pi^2 k A^2 \frac{\delta f^{\alpha/\beta}}{E^{\alpha/\beta}_\mathrm{Diss}} \tag{3.5}$$

with $k = 1800$ N m^{-1} the spring constant of the qPlus sensor, $A = 70$ pm the oscillation amplitude, Q the quality factor of the sensor. The values for E_Diss and δf are extracted from $E_\mathrm{Diss}(\Delta f)$ plots for $\pm V^*$, E_Diss being the maximum of the curve and δf the FWHM. The resulting tunneling rates are summarized in Table 3.1.

These tunneling rates likely represent inter-dot tunneling processes in combination

	δf^- (Hz)	E^-_Diss (meV)	Γ^- (kHz)	δf^+ (Hz)	E^+_Diss (meV)	Γ^+ (kHz)
α array	2.9	14	450	3.2	18	386
β array	1.78	49	79	1.58	51	69

Table 3.1: ***Tunneling rates*** Γ ***according to eq. 3.5 along with parameters to calculate them.*** *Additional parameters:* $f_\alpha = 25.6$ kHz, $Q_\alpha = 5791$, $f_\beta = 25.59$ kHz, $Q_\beta = 7272$.

with tunneling of surface electrons into the delocalized states of the QDA or only either of these processes. Furthermore, the α-QDA has a six times higher tunneling rate ($\overline{\Gamma_\alpha} \approx 420 \cdot 10^3$ Hz) compared to the β-assembly ($\overline{\Gamma_\beta} \approx 65 \cdot 10^3$ Hz), resulting in lower mechanical dissipation and a lower quantum capacitance.

4

Dibromopyrene precursors for the synthesis of chains and GNRs on Au(111)

The results presented in Chapters 4.1.1 to 4.1.3 have been published in the journal Nano Letters[1] [84]. Figures are reproduced with permission from the American Chemical Society.

As a standard model in chemistry and bio-chemistry pyrene has many different uses depending on the substituents in ortho- or para position, be it as a chromophore in photochemistry [121, 122], as a base-substitute in the research of energy transfer for DNA-pyrene oligomers [123] or, as previously shown, as a building block for quantum dot arrays (Chapter 3). Here pyrene is used for its ability to form straight polymers as well as its possibility for the creation of width-modulated graphene nanoribbons (GNRs). These organic molecules are used to investigate the mechanical properties and surface interaction of polymeric molecules and to benchmark the sensitivity of cryo-force spectroscopy.

4.1 2,7-dibromopyrene

4.1.1 Adsorption and synthesis of poly(2,7)-pyrenylene chains

Poly-pyrenylene chains were synthesized from *2,7-dibromopyrene* (27DBP) precursor molecules using on-surface Ullmann-coupling through thermal annealing. A schematic representation of the precursor along with the reaction scheme is shown in Fig. 4.1**a**, where the *Br* dissociate from the molecule leaving a radical that can bond to another radical. The reaction occurs as long as there are precursors in the vicinity to react with. Since the monomers are only bonded by *C-C* single bonds, which reduces the out-of-plane and in-plain stiffness, the chains are more flexible compared to GNRs. Their

[1] Pawlak, R.; Vilhena, J. G.; D'Astolfo, P.; Liu, X.; Prampolini, G.; Meier, T.; Glatzel, T.; Lemkul, J. A.; Häner, R.; Decurtins, S.; Baratoff, A.; Pérez, R.; Liu, S.-X.; Meyer, E. Sequential Bending and Twisting around C–C Single Bonds by Mechanical Lifting of a Pre-Adsorbed Polymer, *Nano Lett.* **20**, 1, 652-657 (2019).

rigidity comes from several parallel double bonds, as well as the extended π-electron system. In contrast to other experiments on *e.g.* dimethyl-substituted polyfluorene from *dibromoterfluorene* [19, 72, 124] both reacted poly-pyrenylene polymers and unreacted 27DBP precursors adsorb flat in the fcc-valleys of the $Au(111)$ surface. The flat adsorption of poly-pyrenylene and 27DPB can be resolved by *CO*-tip modified FM-AFM (Figs. 4.1**b** and **d**) as a uniform contrast in the AFM images. From the high resolution AFM images in Fig. 4.1**d**, single bonds connecting pyrene-monomers can be confirmed. Upon annealing the molecules form long physisorbed chains aligned along the $[11\bar{2}]$ direction, a result of the *Br* atoms being in para position of the 27DBP precursors (Fig. 4.1**c**). The adsorption strength of the poly-pyrenylene chains on the surface is low enough to be easily manipulated using the AFM tip, shown in Fig. 4.2.

In order to complement the experimental data acquired and to understand the un-

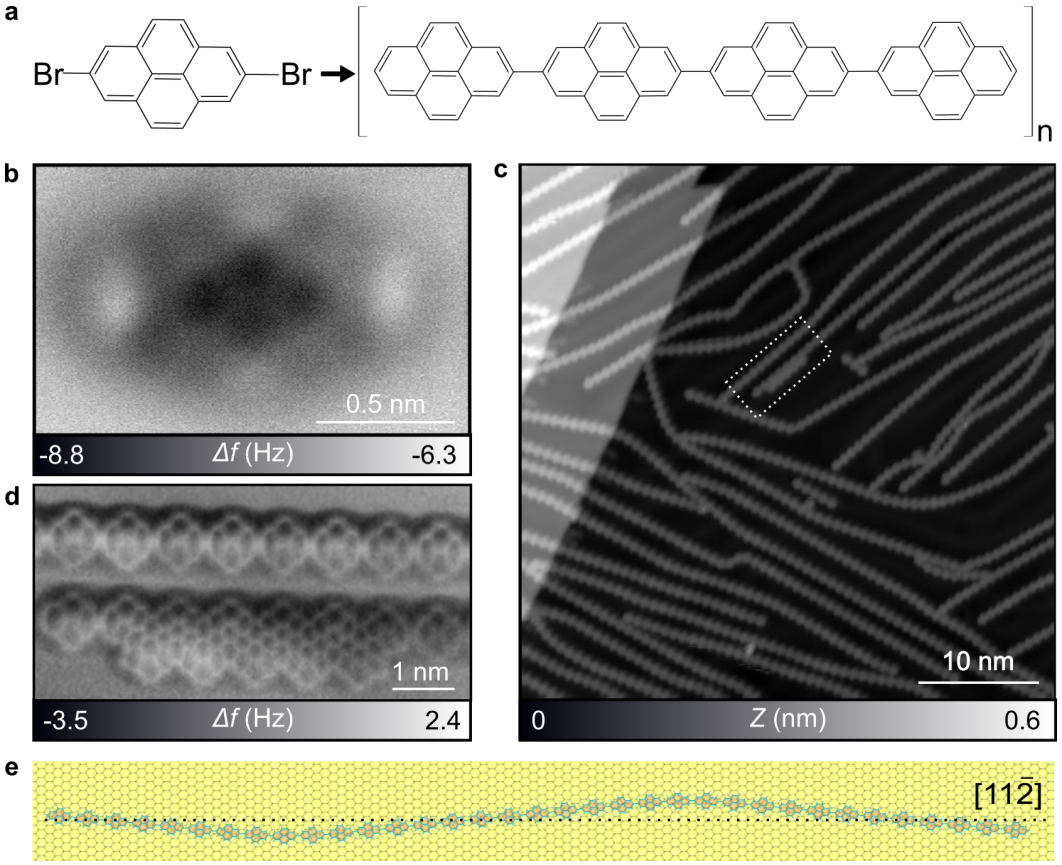

Figure 4.1: ***Adsorption of poly(2,7)-pyrenylene chains on Au(111). a,*** *Reaction scheme for the on-surface Ullmann-polymerization of DBP.* ***b,*** *CO-FM-AFM measurement of the precursor molecule. (f_0 = 24.6 kHz, A_0 = 50 pm, V_{Bias} = 0 V)* ***c,*** *STM image of polymerized single chains along with a fused double polymer creating a GNR with alternating zig-zag and armchair edge (highlighted with dotted rectangle). (I_{setpoint} = 10 pA, V_{Bias} = −1.6 V)* ***d,*** *CO-FM-AFM image of the area marked in* ***c.*** ***e,*** *Adsorption configuration obtained from temperature quenched MD simulations on $Au(111)$. Initial adsorption straight along direction $[11\bar{2}]$ direction.*

derlying mechanics, quantum mechanical (QM) and molecular dynamics (MD) simulations were performed. By comparing the distances between adsorbed monomers, the intermolecular length of $L_{\mathrm{MD}} = 860$ pm is in good agreement with the value extracted from AFM images ($L_{\mathrm{AFM}} = 840$ pm). Fig. 4.1**e** shows a simulation of a polymer that was initially adsorbed along the $[11\bar{2}]$ direction of the $Au(111)$ surface. After thermal quenching, the polymer relaxes and bends in the adsorption plane which minimized the overall energy of the molecule. The bending observed in the MD simulation can also be seen in the experimental STM data (Fig. 4.1**c**). The in-plane bending arises due to variations in bond angles between adjacent subunits, a result of the monomers choosing a better polymer-surface registry. The adsorption geometries for poly-pyrenylene chains gained from simulations and experiments are in contrast to previous experiments on armchair GNRs adsorbing straight along the $[10\bar{1}]$ directions [1] but in agreement with previous experiments on polyfluorene molecules on $Au(111)$ [19]. Compared to poly-pyrenylene and polyfluorene molecules, GNRs have less internal degrees of freedom (DoFs) due to multiple single- or double bonds connecting monomer units, making them sturdier and therefore less likely to bend.

After confirming the ability to easily manipulate poly-pyrenylene chains on the sur-

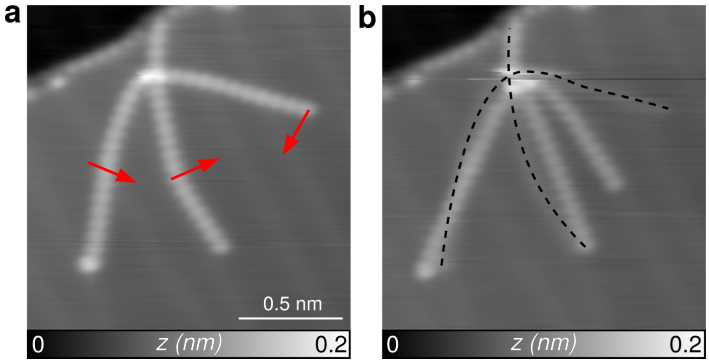

Figure 4.2: ***Lateral manipulation of poly-pyrenylene chains induced by the tip.*** ***a,*** *STM topography image of two polymers crossing one another. Red arrows denote tip movement to manipulate the chains laterally.* ***b,*** *STM image acquired after the manipulation. Initial positions of the chains are marked in dashed lines.*

face, experiments to unveil the adsorption and desorption mechanics, as well as mechanical stability of these polymers can be envisioned.

4.1.2 Cryo-force spectroscopy and the mechanical response

A poly-pyrenylene chain of $n = 35$ pyrene units was lifted from the surface at one end using the tip of an AFM. STM topography images of the polymer are shown in Fig. 4.3**a**, the top depicting the area before and bottom after the experiment. The STM picture after the lifting experiment clearly shows the absence and therefore complete desorption of the polymer from the surface. During the lifting the resulting Δf versus lifting height z was recorded (equivalent to effective stiffness of the system $k_{\mathrm{eff}}(z)$). The experimental lifting trace is plotted in Fig. 4.3**b**. Periodic dips (dashed lines) in

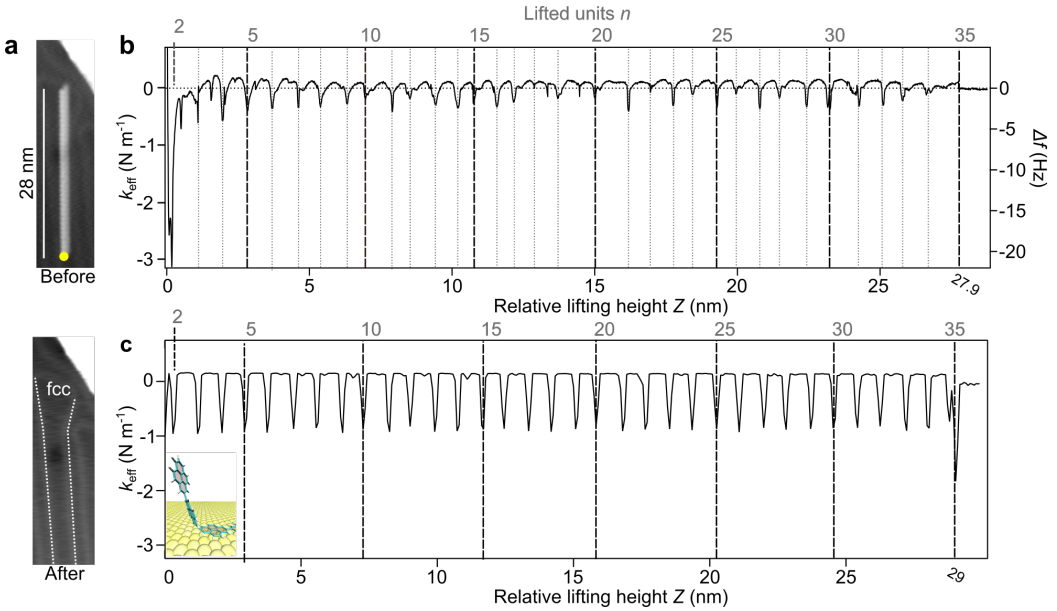

Figure 4.3: ***Lifting of a poly(2,7)-pyrenylene chain and the resulting mechanical response.*** ***a,*** *Top: STM topography of a $n = 35$ monomer long poly-pyrenylene chain close to a step-edge before the lifting. The polymer adsorbed roughly along the fcc valley of the herringbone reconstruction. Bottom: STM topography image after the lifting experiment.* ***b,*** *$k_{\mathrm{eff}}(z)$ ($\propto \Delta f(z)$) trace recorded during lifting, showing monomer detachment events as dips. Complete polymer detachment at $z_{\mathrm{off}} = 27.9$ nm and $n = 35$.* ***c,*** *Simulated and smoothed $k_{\mathrm{eff}}(z)$ trace reproducing the detachment events from the experiment. Analogous complete chain detachment at $z_{\mathrm{off}} = 28.6$ nm and $n = 35$.*

the signal are attributed to detachment events of single monomers. For $z \leq 1.5$ nm k_{eff} falls below 1 N m^{-1} due to additional electrostatic (F_{el}) and Van-der-Waals (F_{vdW}) interaction between tip and sample. Attribution of single monomer detachment events of the first two units is therefore difficult. For $z \geq 1.5$ nm the signal becomes regular with a maximum $k_{\mathrm{eff}} = 0.2$ N m^{-1}, which corresponds to an intact but weak tip-molecule bond and a flexible axial stiffness along the backbone of the polymer. As a result the polymer favors an almost frictionless sliding movement across the surface of the $Au(111)$ sample. Reaching $z_{\mathrm{off}} = 27.9$ nm the molecule completely desorbs from the surface (signal $k_{\mathrm{eff}} = 0$ N m^{-1}) resulting in a average detachment length of $\Delta l_{\mathrm{lift}} = {}^{z_{\mathrm{off}}}/_{33} = 840$ pm (when starting at $n = 2$).

A steered MD simulation for the lifting of a poly-pyrenylene chain consisting of 35 monomers from an unreconstructed $Au(111)$ surface (Fig. 4.3**c**) yields a similar $k_{\mathrm{eff}}(z)$ trace to the experimental data. A harmonic spring with stiffness k_{tip} is used to model the bond between tip and polymer. The carbon in para position of the first pyrene-monomer is fixed in lateral (x and y) directions with freedom of movement in the vertical (z) direction, while bound to a virtual atom moving along z with constant velocity. The resulting lifting trace $k_{\mathrm{eff}}(z)$ replicates the $n = 33$ monomer detachment

events with a full detachment of the polymer at $z_{\text{off}} = 28.6$ nm. The resulting average detachment length of $\Delta l_{\text{sim}} = {}^{z_{\text{off}}}/_{33} = 870$ pm is comparable with the experimental ($\Delta l_{\text{lift}} = 840$ pm) and calculated ($L_{\text{MD}} = 860$ pm) value.

Taking a closer look at the detachment traces two alternating detachment lengths L^+ and L^- can be distinguished. A close up view for detachments of units $n = 7-13$ is depicted in Fig. 4.4**a**, where the alternating spacings can be extracted as $L^+ \approx 920$ pm and $L^- \approx 770$ pm. The simulation (Figs. 4.4**b-d**) illustrates the normal force $F(z)$ acting on the tip (**b**), the effective stiffness $k_{\text{eff}}(Z) = {}^{\text{d}F}/_{\text{d}z}$ (**c**) and the rotation ϕ between consecutive monomers (**d**). Similar to the experimental data, alternating detachment lengths $L^+ = 920$ pm and $L^- = 770$ pm can be extracted. A difference is also visible in Fig. 4.4**d** for the rotational angles of just-lifted odd (purple) and even (turquoise) monomers ($\phi_{\text{n}-1} = +30°$ or $-20°$ respectively). Judging from a top-down point-of-view (Figs. 4.4**e** and **f**) the twist angles of just lifted monomers seem indistinguishable (albeit the opposing sign). Right before lifting however, even monomers already rotate about $-8°$ which combines with the $\phi = -20°$ rotation upon desorption, ultimately resembling the rotation of odd monomers.
Additionally to the rotation of $\phi = \pm 30°$ with respect to their internal axis, the lifted monomers are also inclined by 30° with respect to the surface normal. While pursuing the lifting, monomers rotate further into equilibrium angles of $\phi = \pm 40°$ along their axis. The maximum inclination angle is 10° with respect to the surface normal resulting in a straight sequence of monomers rotated from unit to unit. The energy gain upon rotation of the monomers on one hand and remaining faint attraction between molecule and surface on the other hand causes incomplete rotations of $\phi = \pm 30°$ (as opposed to the equilibrium angles) which results in steric hindrance of hydrogen atoms of adsorbed and lifted monomers (highlighted in red in Figs. 4.4**e** and **f**).
The origin behind alternating detachment lengths is illustrated in Fig. 4.4**b** where the increasing $F(z)$, dropping upon detachment of the monomers (with almost constant slope across the graph) is higher for L^+ ($\overline{F_{L^+}(z)} = 0.4$ nN), compared to L^- ($\overline{F_{L^-}(z)} = 0.38$ nN). By integrating the area under $F(z)$ from drop to peak, the incrementing work which corresponds to the monomer detachment energy can be calculated. A work-energy of $\Delta E_{\text{L}^+} = 180$ kJ mol^{-1}, and $\Delta E_{\text{L}^-} = 146$ kJ mol^{-1} respectively, can be extracted, drastically surpassing the energy gain $\Delta E_{\text{rot}} = 8$ kJ mol^{-1} upon rotation of the just-lifted monomer. The detachment energy however is comparable to the energy gain upon desorption ($\Delta E_{\text{des}} = {}^{(E_{\text{chain}} - E_{\text{ads}})}/_{35} = 137$ kJ mol^{-1} from simulation).

The difference in energy cost from lifting between even and odd monomers, results in the different alternation of L^+ and L^-. The detachment energy is strongly localized between adsorbed (n) and lifted ($n-1$) monomers, analogous to the case of interlocked parts of molecular machines [125, 126]. The difference between even and odd monomers is further visible in the movement of the sterically unhindered hydrogen atoms (ortho-hydrogen H_1 or H_2, opposite the area marked in red in Figs. 4.4**e** and **f**), depicted in Figs. 4.4**g** and **h**. They move along the least corrugated $[\bar{1}01]$ (for purple, odd monomers) and $[0\bar{1}1]$ (for turquoise, even units) directions of $Au(111)$. The trajectories show the hydrogen atoms first moving away from the axis created by initial polymer

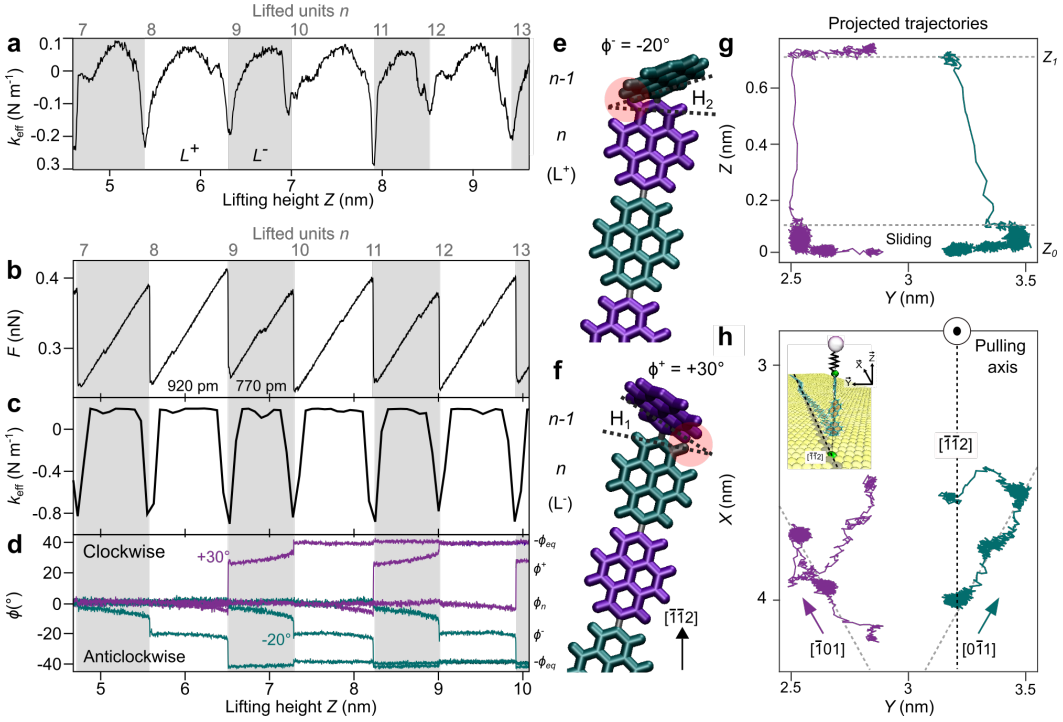

Figure 4.4: ***Origin of mechanical twists and alternating detachment spacings.*** ***a,*** *Close-up of the detachment events in experimental $k_{\text{eff}}(z)$ for units $n = 7-13$, showing alternating detachment lengths $L^+ = 920$ pm in white and $L^- = 770$ pm in gray.* ***b,*** *Simulated normal force $F(z)$,* ***c,*** *Related k_{eff} and* ***d,*** *Rotational angle between the planes of consecutive monomers.* ***e-f,*** *Snapshot of MD simulation prior to detachment of even/odd monomers n, rotating clockwise/anticlockwise due to steric hindrance of just-lifted unit $n-1$ (highlighted in red).* ***g-h,*** *Projected trajectories of hydrogen atoms H_2 (purple, $n = 9$) and H_1 (turquoise, $n = 10$),* ***g,*** *Showing the movement before and* ***h,*** *after successful detachment of the respective monomer. The higher F maxima and therefore longer L^+ for odd n is a result of the units sliding along equivalent Au(111) directions before detachment and the difference in offset relative to the pulling axis.*

alignment and lifting point before moving back towards it. Lateral forces are induced by this asymmetry of the movement causing a modulation in inclination for the bond between units n and $n-1$. After detachment of the first monomer, the desorbed units become almost vertical, in contrast to the gradual bending of fused GNRs [1, 85]. The asymmetric bending of the *C*-*C* bonds therefore most likely induces the alternation in L^+ and L^- as well as the differences in the corresponding force maxima.

4.1.3 Sliding segment of the polymer during lifting

We now consider the sliding segment of the polymer that undergoes a stick-slip motion. The alternation in L^+/L^- for the lifting of the complete 35-monomer long polymer is illustrated in Fig. 4.5**a** for the experimentally acquired data and **b** for the MD simu-

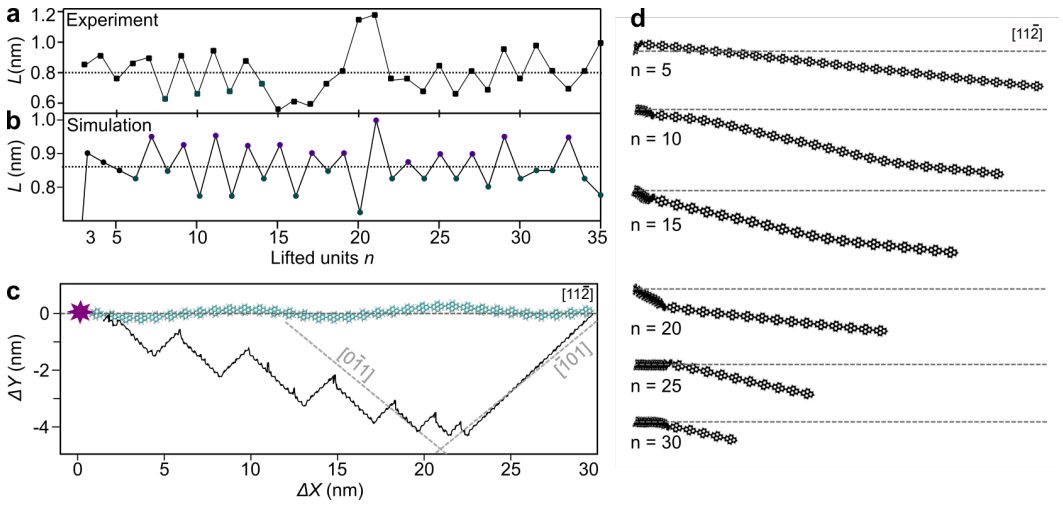

Figure 4.5: ***Polymer motion during the lifting experiment. a-b,*** *Experimentally and simulated detachment lengths versus lifted units for a $n = 35$ monomer long poly-pyrenylene chain.* ***c,*** *Movement trace of the last carbon atom of the tail. For the first six units the polymer deviates from initial symmetric configuration and the tail moves along $[\bar{1}01]$ direction. For following detachment events monomers move along and change between equivalent $[\bar{1}01]$ and $[0\bar{1}1]$ directions of Au(111) towards the lifting point (purple star) but rotated in relation to the initial configuration.* ***d,*** *Snapshots of the configuration during the lifting after desorption of n units. Dense areas on the left show already lifted inclined monomers and signify the shifting of detachment points.*

lation. For $n = 22 - 30$, the alternation is preserved albeit showing irregularities at the end of the lifting range. The motion of the last unit of the polymer during this lifting process is depicted in Fig. 4.5**c**. During the lifting of the first six monomers the sliding polymer rotates into a symmetry-broken configuration with the tail moving in the $[\bar{1}01]$ direction. Upon further lifting, the sliding of the tail varies between two favored directions ($[\bar{1}01]$ and $[0\bar{1}1]$). Snapshots of the polymer configuration, and adsorption direction during the lifting, for several monomer configurations are depicted in Fig. 4.5**d**. The adsorbed polymer undergoes multiple adjustments to optimize surface registry, therefore minimizing energy: First, a lateral shift of the detachment point away from the initial axis. Second, introduction of in-plane bending of the molecule and third, rotation of the polymer away from the $[11\bar{2}]$ direction. The direction of the tail rotation is initialized upon desorption and twist of the first monomer (Fig. 4.6). A clockwise rotation of the first monomer (Fig. 4.6**b**) induces steric repulsion of the hydrogen atoms marked with red arrows, therefore pushing the molecule and tail along the $[10\bar{1}]$ direction (Fig. 4.6**a** bottom, black). An anticlockwise rotation of the first unit (Fig. 4.6**c**) introduces steric hindrance in the positions marked in green, resulting in a rotation and tail movement in the $[1\bar{1}0]$ direction (Fig. 4.6**a** top, purple). The deviation away from the initial axis becomes more evident comparing the configuration of the polymer after lifting of the first unit (Fig. 4.6**d**) and after lifting four monomers (**e**).

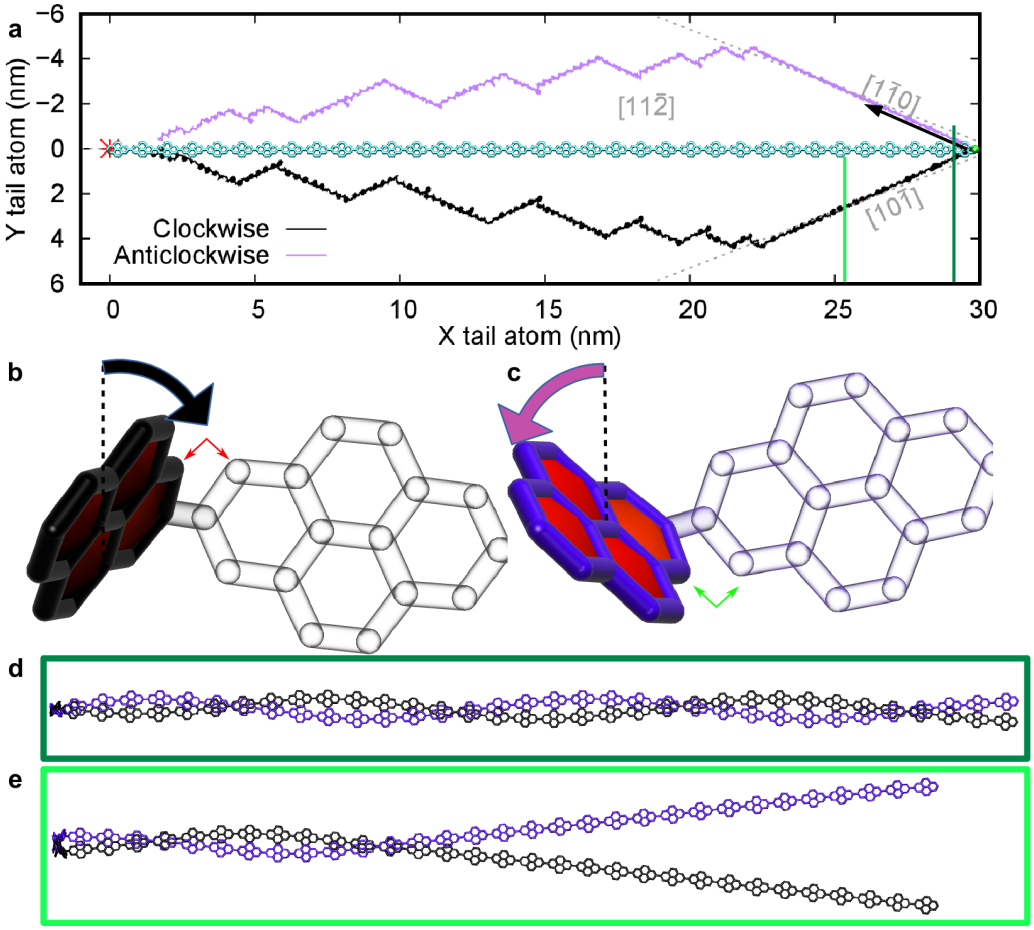

Figure 4.6: ***Impact of first unit rotation upon lifting on polymer movement. a,*** *MD simulated tail movement and initial configuration of a $n = 35$ monomer poly-pyrenylene chain during lifting. Magenta/black trace corresponds to the tail trajectory when the first unit rotates anticlockwise/clockwise respectively.* ***b-c,*** *Schematic drawing of the effect of rotation on the movement of the still-adsorbed units.* ***d-e,*** *Top-down snapshot for first unit lifted, and four monomers lifted respectively.*

With the polymer tail easily sliding across the surface, following the detachment point, sliding experiments of suspended polymers are realizable.

4.1.4 Sliding of a single poly-pyrenylene

In a second experiment, a 10-monomers long polymer is dragged over the $Au(111)$ surface at constant height while recording k_{eff}. The initial configuration of the polymer used is depicted in Fig. 4.7**g**. The molecule was lifted from the end marked in yellow and dragged forth and back along the fcc valley of the herringbone reconstruction, for several parallel lines. Figures 4.7**a** and **d** depict the resulting $k_{\text{eff}}(x, y)$ maps (friction maps) at small ($z = 360$ pm) and larger ($z = 510$ pm) tip-sample separations respectively. The experiment was complemented by all-atom MD simulations.

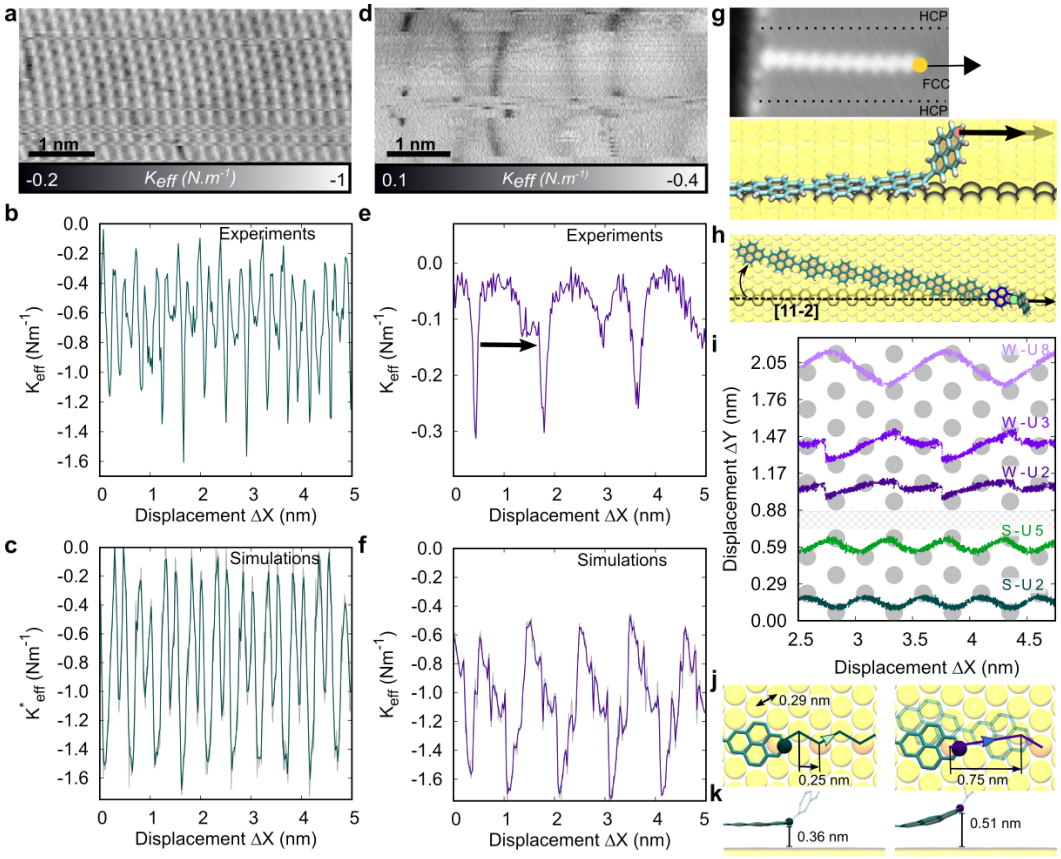

Figure 4.7: ***Slithering motion of a*** $n = 10$ ***monomer long poly-pyrenylene chain.*** *Experimental* $k_{\text{eff}}(x, y)$*-maps for* ***a,*** *The strong (SC) and* ***d,*** *Weak (WC) contact regime. Experimental* k_{eff}*-traces for* ***b,*** *SC and* ***e,*** *WC are extracted from the friction maps and compared to simulated* k_{eff}*-traces (****c,*** *SC and* ***f,*** *WC).* ***g,*** *STM image of the initial configuration of the polymer (top) with a representative side-view (bottom).* ***h,*** *Illustration of the rotation of the polymer during lifting.* ***i,*** *Trajectories of the para-carbon atom of monomers two and five in the strong regime (bottom, S-U2 and S-U5 in green), and units two, three and eight in the weak regime (W-U2, W-U5 and W-U8, in purple).* ***j,*** *Top-view of the intermediate sliding steps in the strong (left) and weak (right) regime with* ***k,*** *Corresponding side-view.*

The low-z separation can be characterized by a strong molecule-surface interaction (strong contact regime, SC). Fig. 4.7**a** shows a repeating pattern of bright features separated by darker areas. The distance between bright features ($d_{\text{SC}} = 0.22$ nm) can be obtained from a $k_{\text{eff}}(\Delta x)$-trace (Fig. 4.7**b**) extracted from the friction map. The increases and decreases of k_{eff} can be attributed to pinning and unpinning events of the polymer on the sample lattice [1, 19, 22, 84]. The extracted sliding distance d_{SC} however is much smaller compared to any of the surfaces periodicities, *i.e.* $d_{\text{SC}} < d_{\text{Au-Au}} < d_{[11\bar{2}]}$ with $d_{\text{Au-Au}} = 0.28$ nm the distance between Au atoms and $d_{[11\bar{2}]} = 0.5$ nm the $[11\bar{2}]$ lattice periodicity.
The MD simulations show a similar k_{eff} behavior, with minima/maxima attributed

to stick-slip events (Fig. 4.7**c**). A comparable sliding distance $d_{\mathrm{SC}} < d_{\mathrm{Au-Au}}$ can be observed from $k_{\mathrm{eff}}(\Delta x)$. Analogous to the tail movement during lifting (Chapter 4.1.3, Fig. 4.6) the polymer rotates $10 - 13^{\circ}$ away from its initial configuration (Fig. 4.7**h**) upon lifting of the first monomer. Simultaneously the pyrenylene subunits move in a zig-zag fashion on the surface following the superlubric/compact directions [127] that are rotated by $\pm 30^{\circ}$ with respect to the sliding direction. This behavior is known as directional locking [128, 129, 130]. The trajectories of the monomers on the surface, illustrated in Figs. 4.7**i** (bottom) and **j** (left), exemplify the zig-zag motion of the monomers moving first diagonally away from the the sliding axis before returning back on the subsequent slip.
This off-axis zig-zag motion results in a small slip-distance $d_{\mathrm{SC}}^{\mathrm{MD}} \approx d_{[11\bar{2}]}/2 = 0.25$ nm. The undulating motion of the monomers across the lattice has already been theoretically predicted for other molecular chains [131]. Comparing the sliding of monomers spatially separated, it becomes evident that the motion of the polymer has an internal phase shift with respect to the sinusoidal motion of the subunits throughout the whole polymer. The dark and light green lines in Fig. 4.7**i** bottom show the trajectories of the second and fifth pyrenylene unit that are in anti-phase to one another. This undulation with internal phase-shift between neighboring monomers strongly resembles the sidewinding motion of snakes on low-friction surfaces [132, 133, 134]. This slithering motion where waves propagate along the body/polymer results in the cancellation of transverse force components and therefore in only a forward motion. In the case of the poly-pyrenylene chain minimizing sliding and static friction.

Increasing the tip-sample separation to the weak contact (WC) regime, *i.e.* $z = 510$ pm, leads to a significant change in the $k_{\mathrm{eff}}(x, y)$-maps (Figs. 4.7**d** and **e**) now featuring long and irregular jumps in contrast to the short stick-slip events. The accompanying MD simulation of k_{eff}, illustrated in Fig. 4.7**f**, shows a periodicity between jumps of $d_{\mathrm{WC}} = 1$ nm, comparable to experimental data (arrow in Fig. 4.7**e**). In the weak regime, each monomer behaves differently and the resulting movement trajectories of consecutive pyrenylene units can not as easily be inferred as in the strong contact regime (Fig. 4.7**i** top, purple, versus bottom, green). In contrast to monomers at the end of the polymer that perform a series of double-jumps in the compact directions of the $Au(111)$ sample, *i.e.* W-U8 in Fig. 4.7**i** (top), pyrenylene units close to the lifted and pulled head-molecule move more irregular over the surface (W-U2/U3). The different dynamics in the SC- and WC-regime are the result of torsion between consecutive monomers, favoring 40° in the gas-phase as opposed to $\sim 0^{\circ}$ for flat lying pyrenylene units adsorbed on the surface. In the SC-regime the second monomer is still adsorbed flat on the surface (Fig. 4.7**k** left) resulting in a near zero torsion angle between monomers two and three. Lifting the first pyrenylene unit, the weak regime increases the torsional angle between U2 and U3, allowing the molecule to slide away from the pulling direction (Fig. 4.7**j** left). Increasing the lifting height of the polymer can therefore directly impact the movement dynamics of the whole adsorbed chain, similar to the "rolling" effect in the sidewinding movement of snakes [133].

To investigate the impact of molecular flexibility on the backward dynamics, the

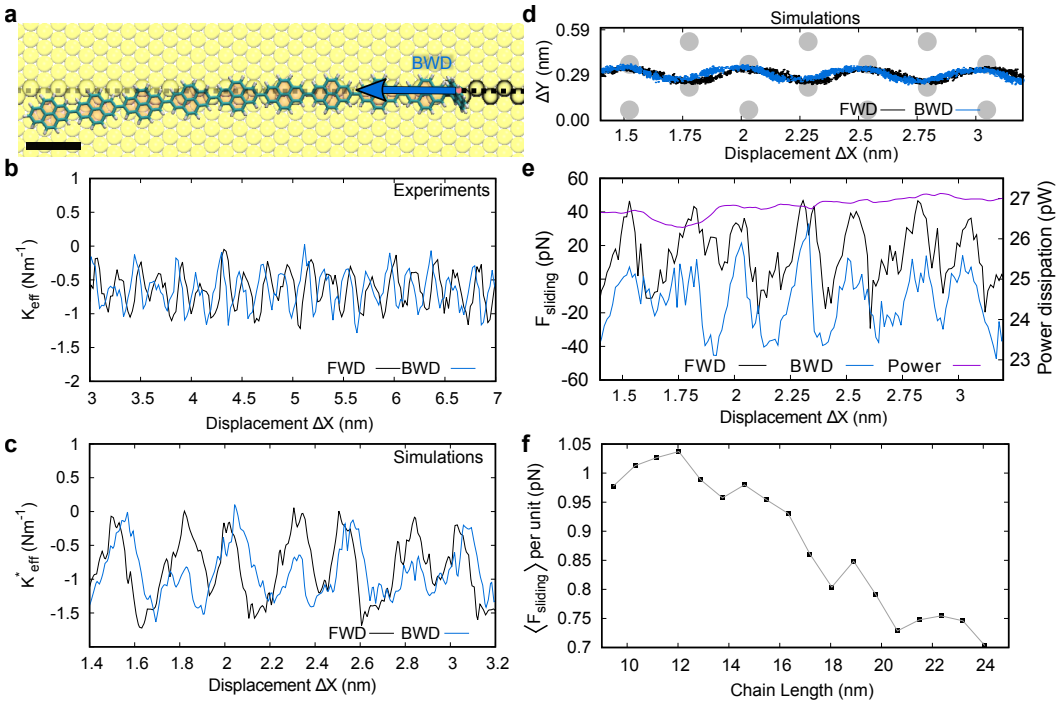

Figure 4.8: ***Flexible superlubricity during backward sliding motion.*** ***a,*** *Snap-shot of the backward motion of the polymer.* ***b-c,*** *Experimental and simulated $k_{\mathrm{eff}}(x)$-traces of the forward (FWD) and backward (BWD) motion.* ***d,*** *FWD/BWD trajectories of the para-carbon of the second monomer.* ***e,*** *Sliding-force traces and corresponding power dissipation during FWD/BWD motion.* ***f,*** *Average friction-force per monomer versus polymer length.*

movement of the tail in the backward motion is examined in Fig. 4.8. The resulting $k_{\mathrm{eff}}(\Delta x)$-trace for the backward movement, in conjunction with the forward trace, is shown in Fig. 4.8**b**, while simulated traces are depicted in Fig. 4.8**c**. Comparing the traces to data previously obtained on GNRs [1], only a small hysteresis between forward and backward motion is visible. This small hysteresis suggests a smoother sliding for poly-pyrenylene than for GNRs. A snap-shot of the simulated backward motion is shown in Fig. 4.8**a**. Despite the high in-plane flexibility of the polymer, the simulation reveals a "tail-first" motion of the chain (pushing the tail), in contrast to a flip or rotation of the tail by 180°, along with the preservation of the monomer undulation on the surface. Comparing forward and backward motion of U2 (Fig. 4.8**d**), the trajectories are almost identical resulting in the small hysteresis of the k_{eff}-trace
Judging from the low magnitude of the friction force (F_{sliding}), illustrated in Fig. 4.8**e**, and similar traces for forward and backward motion, we infer that poly-pyrenylene chains move back and forth across the surface with ultra-low friction. The static friction force of roughly $F_{\mathrm{sliding}} = 35 \pm 10$ pN is similar to the case of GNRs on $Au(111)$ [1], despite the sliding motion of poly-pyrenylene being in a higher friction direction [127]. In contrast to the structural superlubricity of GNRs, where friction forces are cancelled due to the molecular rigidity preventing establishment of registry with the surface lat-

tice [135, 1, 136, 130, 137], removing the rigidity constraint in single bonded polymers results in an ultra-low friction regime for soft molecules, paving the way for reversible nano-motion.
Superlubricity can further be characterized by asymptotically vanishing friction forces with increasing contact area (already verified for GNRs up to 25 nm in length [1]). For poly-pyrenylene chains, the simulated average friction force for polymers with lengths from 9 to 24 nm is shown in Fig. 4.8**f**. Analogous to superlubric GNRs, the sliding friction of poly-pyrenylene chains decreases with increasing polymer length implying a reduction of the forces needed for unpinning an atom of the molecule from the surface. This superlubricity stems from the capability of the polymer to adapt its surface registry during the motion by minimizing interaction forces with the surface through conformation adaption. This is in direct contrast to conventional structural superlubricity [1, 130, 135, 136, 137].

As a result of the incommensurability of organic molecules, such as poly-pyrenylene chains, and the $Au(111)$ surface, two major effects can be observed in the MD simulation: 1) introduction of mechanical stress into the molecular system due to the surface periodicity and 2) asynchronous excitation/de-excitation of the internal degrees of freedom (DoF) during the sliding movement.
The first effect can be understood by considering the equilibrium in-plane angle between the first two monomers adsorbed flat on the surface in the SC regime (Figs. 4.9**a** and **b**). The oscillating deviation from the equilibrium angle by $\Delta\theta_{\mathrm{U2-U3}} = \pm 0.75°$ into two metastable configurations clearly indicates the whole polymer being under constant strain that only disappears when $\Delta\theta = 0°$. The sliding forces (F_{sliding}) and work-energies ($\mathrm{W}_{\mathrm{sliding}}$) at positions where $\Delta\theta = 0°$ decrease, indicating a slipping motion and therefore relaxation of the molecule.
The effect of the internal DoF is also visible when comparing angles separated over a large distance. Fig. 4.9**b** depicts the in-plane angles between monomers two and three ($\Delta\theta_{\mathrm{U2-U3}}$, black) as well as between monomers five and six ($\Delta\theta_{\mathrm{U5-U6}}$, gray) being laterally shifted to one another. In addition to the lateral shift, $\Delta\theta_{\mathrm{U5-U6}}$ shows a higher deviation from the equilibrium angle compared to $\Delta\theta_{\mathrm{U2-U3}}$ resulting in the dynamical cancellation of most of the lateral forces. Comparing the lateral shift of the angle oscillations of all monomer junctions in MD simulations with varying polymer length revealed no synchronization or asynchronization regardless of polymer length. It can therefore be rationalized that the polymer sliding over the surface is an adaptive process. The aforementioned incommensurability of poly-pyrenylene and the underlying $Au(111)$ surface therefore leads to local bending of the junctions with the corresponding lateral shifts of angle oscillations between spatially separated junctions becoming incoherent.

The impact of the internal DoF on the sliding friction forces on $Au(111)$ for rigid (purple) and flexible (black) poly-pyrenylene chains is depicted in Fig. 4.9**c**. The flexibility of the sidewinding motion compared to the stability of a rigid slider results in 1) a decrease of the slip periodicity, 2) a substantial reduction of the F_{sliding} magnitude as well as 3) a higher average F_{sliding}. The increase of slip length in the case of the

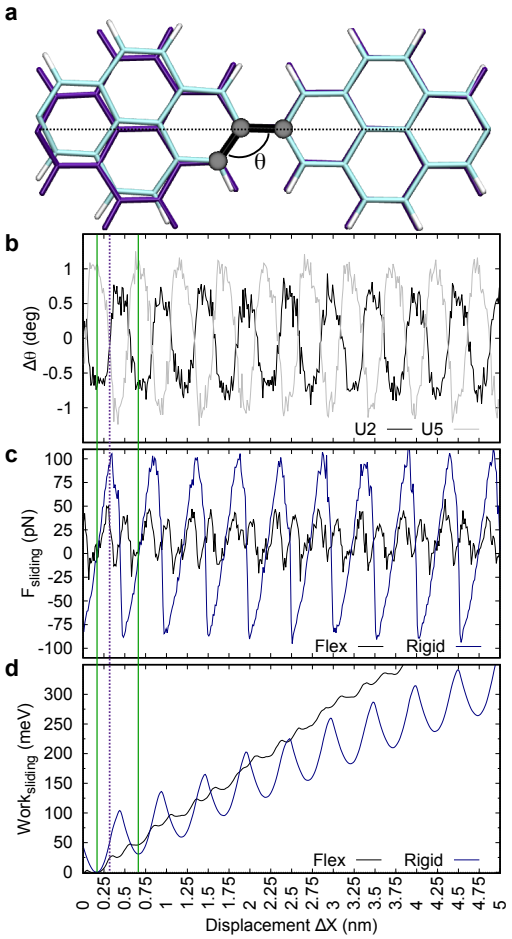

Figure 4.9: ***Correlation between bending angles, slip dynamics and energy dissipation of a deca-pyrenylene sliding over*** **Au**(111)***.*** ***a,*** *Bending angle θ between units two and three. Purple represents the straight and cyan the bend configuration during the sliding.* ***b,*** *$\Delta\theta$ evolution during sliding motion for U2 (between monomers two and three) and U5 (units five and six).* ***c,*** *Friction force for a rigid and flexible polymer with* ***d,*** *Work required for the motion of the polymer.*

rigid slider is a direct consequence of the polymer rigidity, imposing the polymer to only move along the $[11\bar{2}]$ sliding direction (where $d_{[11\bar{2}]} = 2 \times d_{\mathrm{SC^{MD}}}$). On the other hand sidewinding breaks down this sliding motion into smaller slips, reducing the overall energy barrier required to move the molecule. This subsequently decreases the amount of pyrenylene-atoms to be unpinned from the surface and therefore decreases the forces required to move the polymer. The chain bending related to the surface lattice also has an impact on the total strain that can be restored in the case of the flexible molecule, in contrast to a rigid polymer. When the polymer is straightened at the onset of slip events, due to the pull of the AFM tip (*i.e.* $\Delta\theta = 0°$), the mechanical strain on the junctions due to bending is decreased (F_{sliding} and $\mathrm{Work}_{\mathrm{sliding}}$ decreasing at the purple line in Figs. 4.9**b-d**). The bending energy therefore reduces the work required for unpinning poly-pyrenylene atoms. The kinetic energy from slip events is

partly recovered and converted into conformational adaption of the junction. In the slipping process however some energy dissipates into vibrations of the molecule coupled to the $Au(111)$ surface (Fig. 4.9**d**). In the case of the rigid polymer some of the energy introduced for the polymer movement is recovered after each slip event whereas in the case of the flexible molecule less than 10% is recovered over shorter slip periods. Sidewinding motion of the polymer thus reduces diffusion barriers by jumping into local minima and energy barriers thanks to the flexibility of the molecule. Compared to the case of the rigid slider, the sidewinding motion has a higher energy dissipation for slip events due to spatially delocalized out-of-phase bending of the polymer and vibrational coupling to the surface.

4.2 1,6-dibromopyrene

To emphasize the difference of a rigid slider compared to a flexible sidewinding motion a pyrene-based precursor was used to create GNRs with two bonds connecting the pyrene monomers, therefore removing internal DoFs.

4.2.1 Bottom-up synthesis

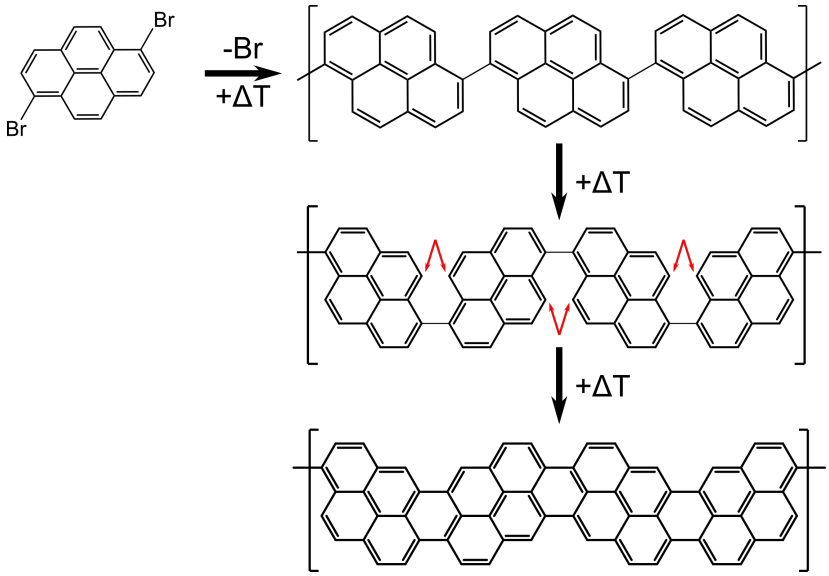

Figure 4.10: ***Reaction pathway of*** $(1,6)$***-dibromopyrene.*** *16DBP precursors create a poly(1,6)-pyrenylene chain. With more energy every second monomer flips and a pGNR is finally synthesized.*

With *Br* atoms in ortho position, as opposed to para position for the creation of poly-pyrenylene chains, a pyrene-based GNR (*pGNR*) can be synthesized (Fig. 4.10). In a first step a chiral poly-pyrene chain is formed with bonds connecting monomers in a diametrical ortho position. In a second step, adding more energy in form of heat will flip every second unit of the polymer creating a meta-stable configuration (Fig. 4.10

middle). With sufficient energy the metastable polymer is able to undergo cyclodehydrogenation at the sterically hindered hydrocarbons (red arrows), to finally create *C-C* bonds and a pGNR (Fig. 4.10 bottom). This reaction was first reported by Sun *et al.* [81] and was reproduced on *Au*(111).
The precursor molecules were evaporated onto a pristine *Au*(111) surface where they self-assembled into small molecular sheets (Fig. 4.11**a**). Upon thermal annealing, pGNRs are synthesized by on-surface Ullmann-polymerization. STM and AFM images of the pGNRs are shown in Figs. 4.11**b** and **c** respectively. Bigger (red arrow) and smaller grooves (green) along the molecules can be spotted in the STM and AFM measurements that are also visible in the scheme of Fig. 4.10 bottom.

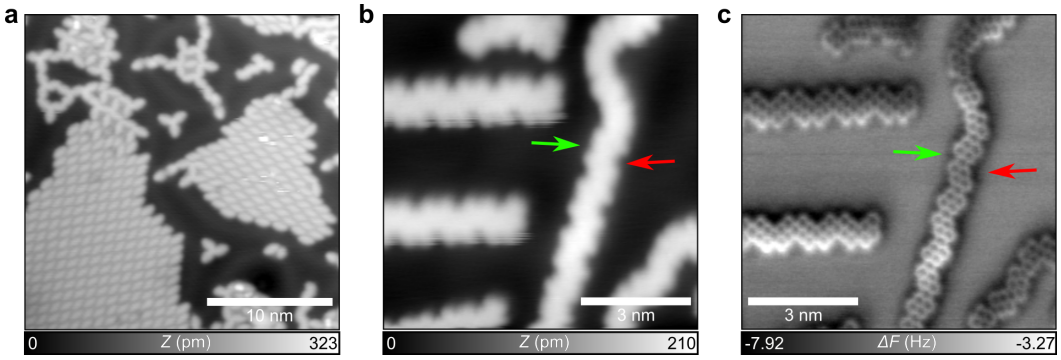

Figure 4.11: ***(1,6)-dibromopyrene precursors and the synthesis of pGNRs.*** *STM image of* **a,** *The precursors after evaporation on* Au(111) *and* **b,** *Fully synthesized pGNRs. (*$I_{\text{setpoint}} = 1$ pA*,* ***a****:* $V_{\text{Bias}} = -1$ V ***b****:* $U_{\text{Bias}} = 200$ mV*)* ***c,*** *AFM measurement with CO-modified tip of the area in* ***b****. (*$f_0 = 25.5$ kHz*,* $A_0 = 50$ pm*,* $Q = 7988$*)*

The atomic structure of the pGNRs is resolved by AFM using *CO*-terminated tips (Fig. 4.11**c**), which allows for extraction of a monomer length of $L \approx 540$ pm.

4.2.2 Sliding of suspended pGNRs

To explore the sliding characteristics of pGNRs, an eight-monomers long pGNR was lifted to a height z from the surface (Fig. 4.12**a**, lifted at the end highlighted in green). The pGNR was then pulled/pushed along the valley of the herringbone reconstructed *Au*(111). The recorded stiffness $k_{\text{eff}}(x, y)$-maps for forward and backward motion are shown in Fig. 4.12**c** respectively. The k_{eff}-maps strongly differ between both directions except for $z = 400$ pm, where forward and backward motion appear similar, signifying reversibility of the pulling motion at this specific height. The maps clearly show a strong evolution of the friction patterns while increasing tip-sample separation, even within the distance of a single monomer ($0 < z \leq 550$ pm). In comparison to the sliding of poly-pyrenylene chains, where an increase of tip-sample separation of only $\Delta z = 150$ pm completely modifies the polymer sliding from a strong stick-slip to a nearly frictionless motion (Figs. 4.7**a** and **d**), the same tip-sample separation z does not decrease the friction of the pGNR as much (i.e. $z = 100$ pm versus $z = 250$ pm or

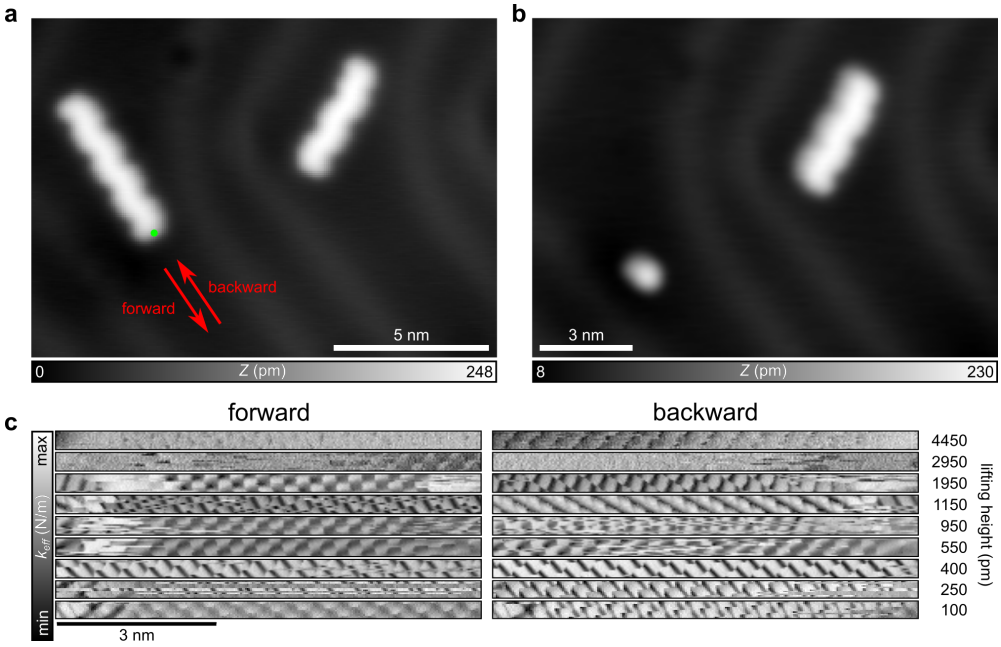

Figure 4.12: ***Sliding of suspended pGNRs.*** *STM image of the area around the pGNR* ***a,*** *before and* ***b,*** *after the sliding of the ribbon in the direction of the red arrows (*$I_{\text{setpoint}} = 1$ pm, $V_{\text{Bias}} = -0.8$ V*).* ***c,*** $k_{\text{eff}}(x, y)$*-maps of forward and backward sliding motion at different tip-sample separations. (*$f_0 = 23.76$ kHz, $A_0 = 50$ pm, $Q = 12863$*)*

$z = 400$ pm versus $z = 550$ pm).

Despite the pGNR being lifted by half its length ($z = 1950$ pm), the atomic pattern in the k_{eff}-maps can still be spotted. Only for tip-sample separations $z \geq 2950$ pm, the contrast mostly vanishes, a result of a weak molecule-surface interaction and mostly low-friction movement of the pGNR similar to the findings of Kawai *et al.* [1].
Only when the molecule is nearly desorbed from the surface ($z \geq 4450$ pm), and the tip drags the tail of the pGNR over the sample, a $k_{\text{eff}}(x, y)$-map similar to the weak regime of the sliding of a poly-pyrenylene chain (Fig. 4.7**d**) can be observed in the forward motion. The $k_{\text{eff}}(x, y)$-maps for the backward motion on the other hand show a stick-slip pattern due to a difference in adsorption angles between forward and backward motion. In contrast to the sliding in the weak interaction domain of poly-pyrenylene chains, this featureless map in the forward direction mostly results from the small interaction area with the surface. The backward k_{eff}-map results from pushing the pGNR which, due to the rigidity of the molecule, jumps from one adsorption site to the next.

As shown, the removal of internal DoFs completely changes the sliding behavior of molecules, despite the base unit of pyrene being the same in the case of poly-pyrenylene and pGNR sliding. The pGNR is unable to improve its surface registry by undulation which results in a higher measurable friction even for small molecule-surface interaction areas.

5 Monomer stabilization of mechanically lifted CPAA-polymers

A peculiar interaction of surface and molecules is the ability of the surface to stabilize compounds otherwise not stable in gas-phase. This can be used for the bottom-up on-surface synthesis [138] of molecules that are classically not achievable with top-down processes, *i.e.* molecules that are under internal sterical stress. Here the surface adsorption energy overcomes the rotational energy that is caused by steric hindrance of opposing hydrogen atoms. After synthesis and in-situ characterization of the molecule with STM and AFM, cryo-force spectroscopy, an established technique to measure the surface interaction of molecules such as polymeric chains [19, 22, 83, 88] and graphene nano ribbons [1], can be used to determine the stability of the compound. To complement the experimental data Molecular Dynamics (MD) simulations of the lifting process can be used to gain further insight into the mechanisms governing the behaviour of the molecule.

5.1 Ullmann-coupling of CPAA precursors

Using *1,6-cyclopenta[h,i]aceanthrylene* (CPAA) precursors the polymers were synthesized on *Au(111)* by on-surface Ullmann-coupling through thermal annealing. The reaction pathway is schematically depicted in Fig. 5.1. As can be seen, two bond configurations are possible with either the anthracene backbones parallel to each other, or every second unit flipped by 180° forming a zig-zag polymer.

The polymerized molecules are shown in Fig. 5.2**a**. Winding and interlinking polymers with bigger and smaller grooves along the edges can be spotted that follow the herringbone reconstruction. Two different sizes of grooves can be attributed to the parallel and antiparallel bond configurations. When looking at the *CO*-AFM measurement (Fig. 5.2**b**), two interlinking polymers with changing bonding motifs are shown along with four *Br* adatoms (bright dots) decorating the edge of the horizontal polymer (marked with red arrows).

The internal structure of each unit obtained by AFM with *CO* modified tip is visi-

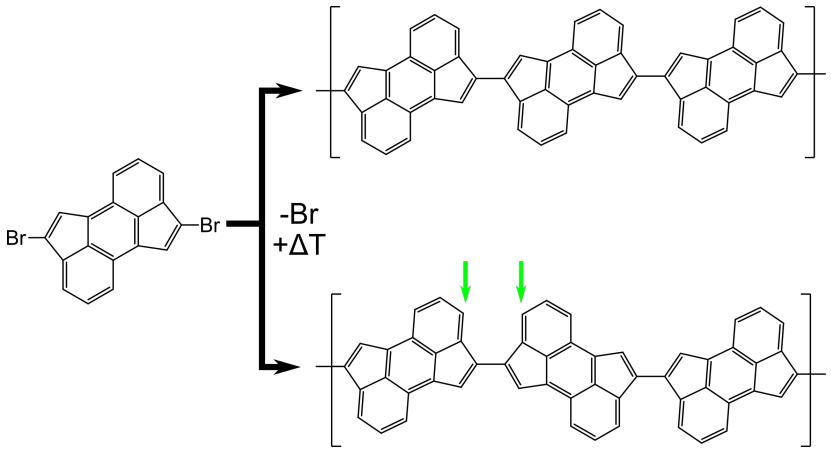

Figure 5.1: ***Reaction pathway for the synthesis of CPAA polymers.*** *On the left is the Br_2-CPAA precursor molecule that is used for the Ullmann-polymerization reaction when provided with sufficient energy in the form of thermal energy. On the right the two possible conformations with an all parallel configuration at the top and alternating sequence at the bottom. Green arrows indicate the opposing hydrogen atoms responsible for the steric repulsion.*

ble, each consisting of the aforementioned anthracene backbone with fused pentacene rings on each side. A detailed view of the bond configurations is pictured in Fig. 5.2**c** and **e** along with Kekulé-drawings of the structures for the parallel and antiparallel sequences respectively. A gas-phase molecular-dynamics (MD) simulation was performed, tracking the rotational energy ΔE_{rot} upon rotation around the bond connecting two monomers and depicted in Fig. 5.2**d**. Starting from $\varphi_0 = 0°$ in the parallel configuration, the molecule rotates out into $\varphi_1 = 30°$ minimizing the overall energy. The rotation is caused by steric hindrance of the adjacent hydrogen atoms disfavoring the stabilization of the extended conjugated π-system of the CPAA monomers. Further rotation around φ into 90° is accompanied by an increase in energy to $\Delta E_{\text{rot}} = 240$ meV caused by the destruction of the π-conjugation. The rotation away from 90° to $\varphi_2 = 140°$ restores this conjugation, lowering ΔE_{rot} to the second minima. Finally for the rotation into $\varphi_3 = 180°$ a significant amount of energy is needed ($\Delta E_{\text{rot}} = 340$ meV). Here, the stabilization and energy minimization of the π-system is overcome by the strong steric hindrance of the adjacent hydrogen atoms of the anthracene backbone.
Judging from the uniform contrast of the AFM measurements (Figs. 5.2**b**, **c** and **e**), the surface adsorption is able to overcome the high energies at φ_0 and φ_3 stabilizing even the sterically frustrated antiparallel configuration. As shown later, the energy barrier between the equilibrium angles φ_1 and φ_2 ($\Delta E_{\text{rot}} = 240$ meV $\approx 580\ k_B T$ at $T = 4.8$ K + 2D confinement of the surface) is high enough to prevent a free rotation from one to the other.

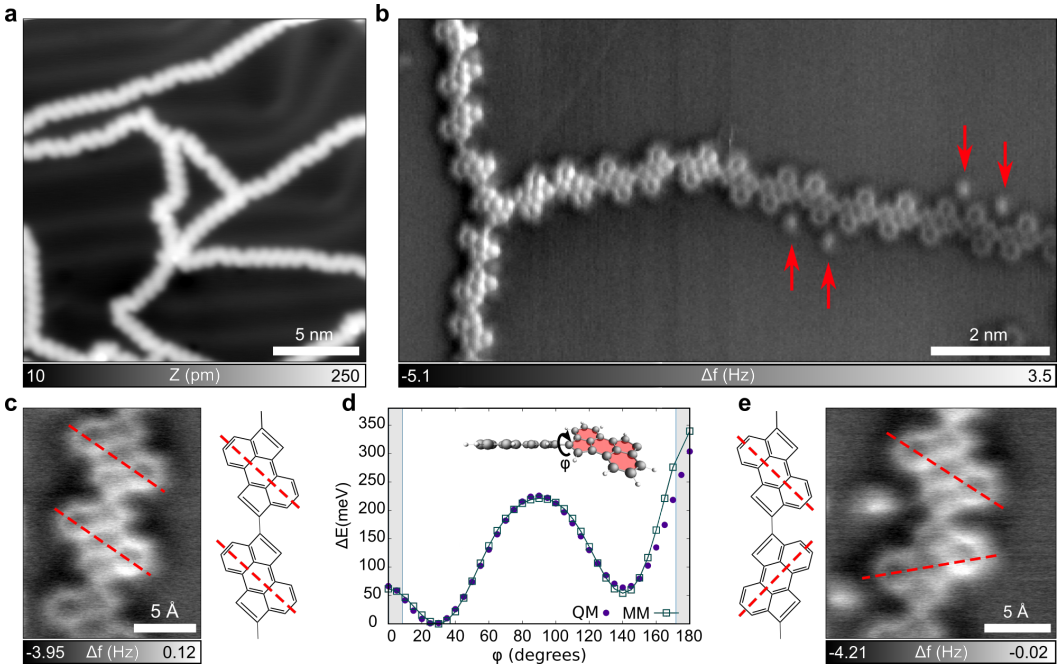

Figure 5.2: ***On-surface synthesis of sterically frustrated polymers. a,*** *STM measurement of interlinking polymers showing the created network. ($I_{\text{setpoint}} = 1$ pA, $V_{\text{Bias}} = -1$ V) **b,** FM-AFM image with CO-modified tip of CPAA polymer with parallel and antiparallel sequences of monomers. Br adatoms are visible on the right-hand-side along the polymer. ($f_0 = 25.57$ kHz, $A_0 = 50$ pm, $Q = 7357$, $V_{\text{Bias}} = 0$ V) Detailed AFM image of **c,** the parallel and **e,** antiparallel bond configuration with a Kekulé-representation of the structure. **d,** Simulation of the gas-phase rotational energy upon rotation around the bond connecting two monomers. Two minima belonging to the two configurations are separated by a high energy barrier.*

5.2 Cryo-force spectroscopy and mechanical stabilization of frustrated polymers

Lifting experiments on polymers with one free lying end were performed and experimental results were compared to MD simulations of the same lifting process. Fig. 5.3**a** shows the CPAA-polymer before the lifting experiment. The orientation of the middle monomers along with a simulated representation of the molecule is inset in Fig. 5.3**a**. The molecular chain has one free lying end, the other end tethered to a step-edge outside the scan area. Starting from the free end, the polymer was peeled off the surface using the AFM tip, lifted for $\Delta z = 4$ nm before inverting the motion of the tip, reapproaching the surface again for $\Delta z = 2$ nm for redeposition of the molecular chain back onto the surface. The molecule was then finally lifted further until the bond between tip and molecule ruptured. The resulting frequency shift Δf signal recorded is shown in Fig. 5.3**b** in blue (lifting) and red (redeposition) respectively. An intricate sequence of ridges and dips in the Δf signal can be spotted, the dips corresponding to detachment events of monomers from the surface for the lifting and readsorption

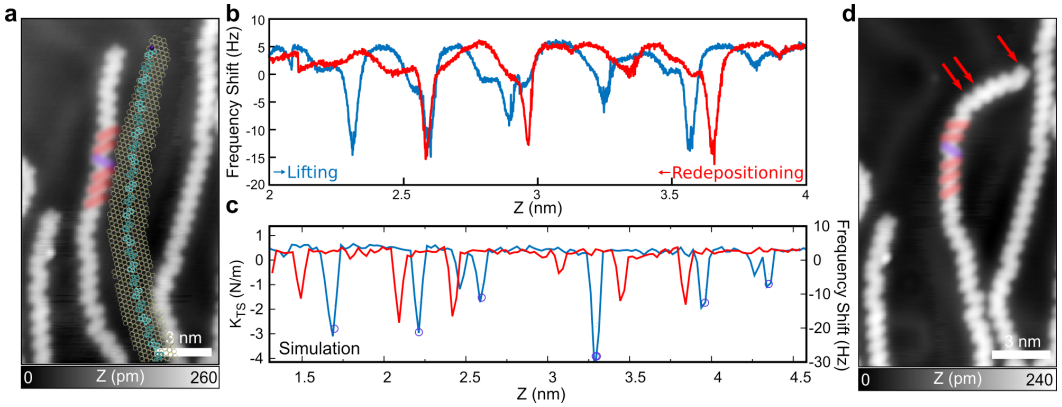

Figure 5.3: ***Measurement and simulation of the lifting experiment.*** ***a,*** *STM topography image showing the polymer to-be-lifted along with the initial configuration for the MD simulation. Highlighted on the polymer is the redeposited sequence, with left oriented monomers in blue and right in red respectively. ($I_{\text{setpoint}} = 1$ pA, $V_{\text{Bias}} = -0.5$ V)* ***b,*** *Frequency shift lifting trace for the lifting- (blue) and redepositioning process (red). Dips correspond to detachment/readsorption events. ($f_0 = 23.74$ kHz, $A_0 = 50$ pm, $Q = 6077$, $V_{\text{Bias}} = 0$ V)* ***c,*** *Contact stiffness k_{TS} and Δf simulation of the monomer sequence highlighted in* ***a*** *with trace-colouring equivalent to the experiment. Blue circles marking detachment events.* ***d,*** *STM measurement showing the scanned area and polymer after the lifting experiment. Orientation of the units in the highlighted area remained unchanged.*

events for the redepositioning of the polymer respectively. The detachment and readsorption lengths during the complete lifting experiment, *i.e.* the distance between two deep dips, strongly vary in length from short distances of $\Delta l = 250$ pm to long detachments/readsorptions of $\Delta l = 580$ pm. In the experiment, all lengths deviate from the DFT-simulated value of a single CPAA-monomer in the polymer ($\Delta l_{\text{DFT}} = 827$ pm). The traces for lifting and redepositioning are in good agreement to one another, possessing similar features for the same suspension height.
Especially between $Z = 3 - 4$ nm the traces seem almost identical, albeit the redepositioning trace being shifted a few pm higher compared to the lifting one. Previous experiments on lifting experiments already reported on similar features in the Δf traces [19, 84]. Additionally, the experiment shows a high stability of the bond motifs even without the constraining properties of the surface, indicated by the reversibility of the traces and therefore the preservation of the initial orientation of the suspended monomers. The stabilization is further evident in Fig. 5.3**d** where the sequence that was redepositioned in the experiment retained their orientation even after the tip-polymer bond rupture. The altered monomer orientations of the polymer is proof of the molecular manipulation. Some monomers close to the manipulated end unfortunately inverted their orientation (units $N = 1, 4, 5$, red arrows). The energy needed to overcome the energy barrier ΔE_{rot} and transition between φ_1 and φ_2 is presumably provided by the sudden gain of vibrational energy during the rupture of the tip-polymer bond, dissipating along the polymer upon orientation change of a random subunit.

The lifting experiment is accompanied by a MD-simulation of the lifting/redepositioning process. The simulated contact stiffness k_{ts} ($\Delta f \approx 7.2 k_{\mathrm{ts}}$) is plotted in Fig. 5.3**c** where analogous to the experimental data a sequence of dips can be spotted. In the lifting trace (blue), the detachment events marked with blue circles feature detachment lengths comparable to the data acquired experimentally. The simulation also reproduces the high reversibility of the lifting process, stabilizing the initial orientation sequence of the monomers.

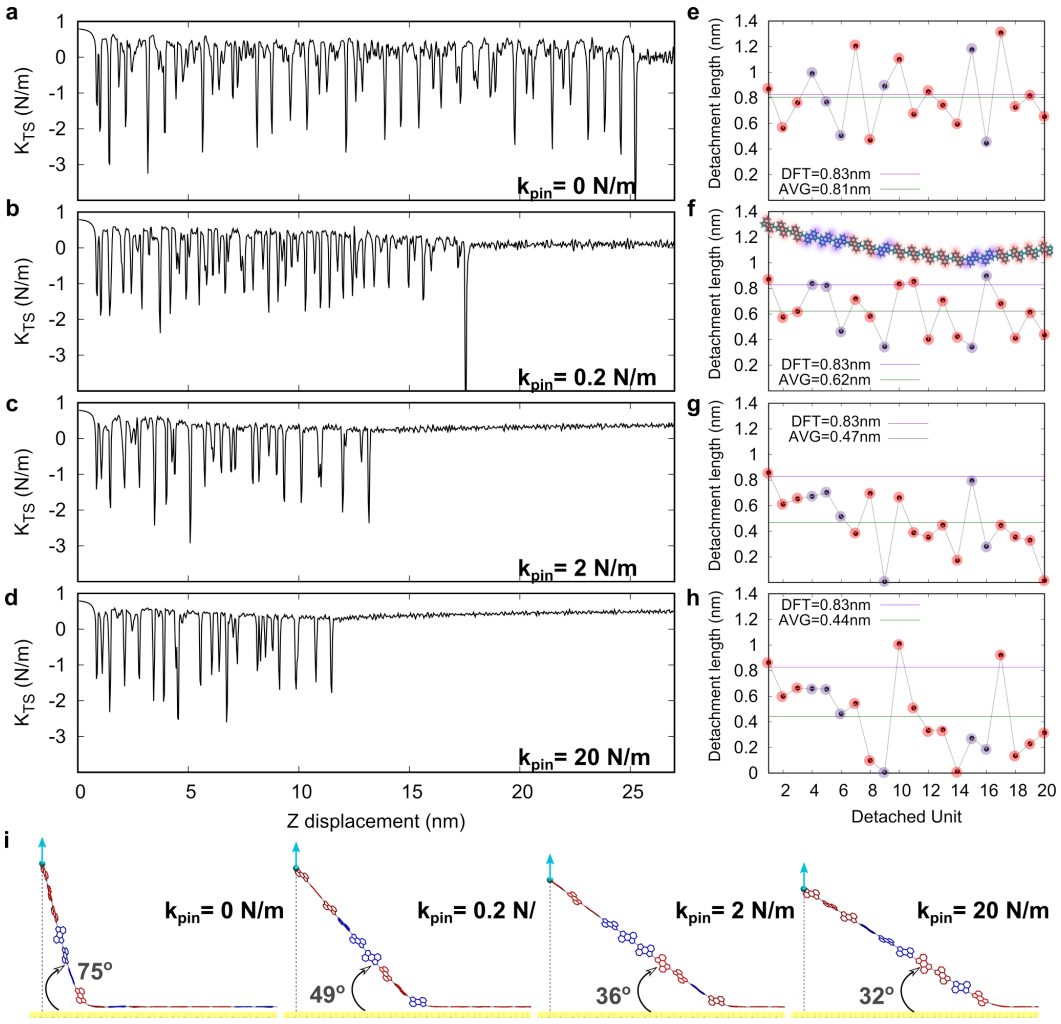

Figure 5.4: ***Dependence of contact stiffness and detachment length on the tethering strength.*** ***a-d*** *Contact stiffness $k_{\mathrm{ts}}(z)$ of a 30 monomer long CPAA-polymer with varying tethering strength. Pinning strength (k) ranging from 0 Nm^{-1} (**a**) to a strong tethering 20 Nm^{-1} (**d**).* ***e-h,*** *Detachment length of 20 monomers with their corresponding orientation highlighted in red (right-handed) and blue (left-handed) respectively. For comparison the average detachment length (green line) along with the DFT calculated length of a single monomer is added (red line).* ***i,*** *Calculated angles during the lifting process depending on the tethering strength.*

To explain the discrepancy between experimental detachment lengths and the DFT values, the MD data for different tethering strengths was analysed. In a first simulation, depicted in Figs. 5.4**a-d**, the influence of tethering strength of the last carbon atom of the polymer to the surface was inspected, ranging from no tethering in **a** ($k = 0$ Nm^{-1}), weak tethering in **b** and **c** ($k = 0.2$ Nm^{-1} and $k = 2$ Nm^{-1}) to a strong pinning in **d** ($k = 20$ Nm^{-1}). Shown in Fig. 5.4, the sudden rupture of tip-molecule bond occurs earlier every time with increasing pinning strength. The tethering strength also changes the mean detachment length of each monomer, shown in the right graphs of Figs. 5.4**a-d**. Here again, with increasing tethering strength, the mean detachment length of the CPAA units decreases from near DFT-length $\Delta l_0 = 810$ pm for no tethering to almost half the DFT calculated monomer length $\Delta l_{20} = 440$ pm. Fig. 5.4**e** finally depicts the dependence of the detachment angle on the tethering strength. As shown, for $k = 0$ Nm^{-1} the monomers detach with an angle of 75° with respect to the surface, a result of the polymer being able to follow the lifting (comparable to a necklace being lifted from the table). This sliding of the tail was already reported in Chapter 4 for the lifting of molecular poly-pyrene chains, the simulation therefore being in good agreement with past experiments. Increasing the pinning strength of the carbon atom at the end subsequently also decreases the contact angle for the just lifted monomer ($\vartheta = 75°$ for $k = 0$ Nm^{-1} vs. $\vartheta = 32°$ for $k = 20$ Nm^{-1}). The tail is not able to follow to the lifting point anymore and the monomers are being peeled from the substrate (*e.g.* opening a velcro fastener). This decrease in detachment angle is also reflected in the decreasing detachment lengths.

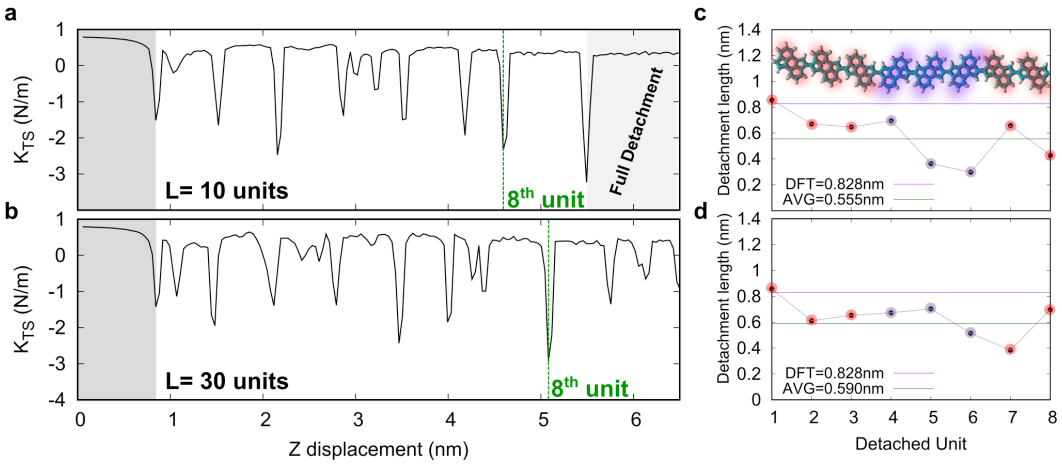

Figure 5.5: ***Dependence of contact stiffness and detachment length on the polymer length.*** *Contact stiffness $k_{\mathrm{ts}}(z)$ for the lifting of a 10 unit long polymer (**a**, L_{10}) and 30 monomers long polymer (**b**, L_{30}). Tethering strength in both cases was fixed to $k_{\mathrm{pin}} = 2$ Nm^{-1}.* ***c-d,*** *Detachment lengths for the first 8 monomers with an average length as well as the DFT calculated length is shown for L_{10} (**c**) and L_{30} (**d**) respectively. Highlighted in red and blue are the orientations analogous to Fig. 5.4.*

In a second simulation, the length of the polymer was varied to gain insight into the

influence of the polymer length, while the pinning strength was fixed at $k = 2$ Nm^{-1}. The resulting k_{ts}-trace is plotted in Fig. 5.5**a** for a poly-CPAA chain of 10 units (L_{10}) on the left along with the detachment length of the first eight monomers and in **b** for 30 units (L_{30}) respectively. As displayed detachment of the eighth unit occurs earlier for L_{10} at $z \approx 4.6$ nm compared to $z \approx 5.1$ nm for L_{30}. The effect is also visible when looking at values for detachment lengths averaging at $\Delta l = 555$ pm for L_{10} as opposed to $\Delta l = 590$ pm for L_{30}. In the case of L_{10} the stabilization of the extended π-electron system has a higher relative impact on the rigidity of the polymer backbone, compared to L_{30} where the chain is able to bend downward during the lifting due to the length of the polymer.

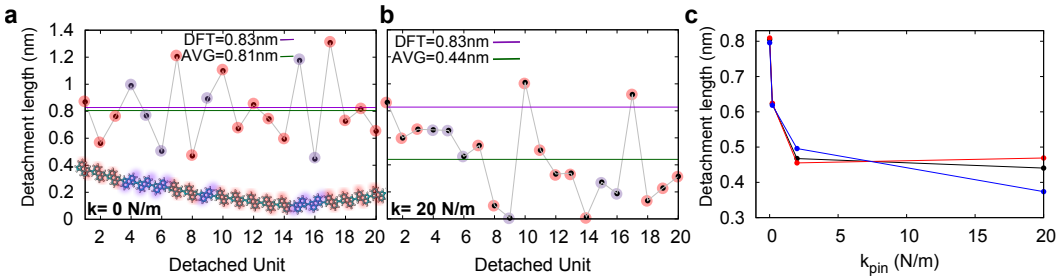

Figure 5.6: ***Impact of tethering strength on the detachment length of different orientations of the monomers.*** *MD simulation of the detachment length for* ***a,*** *no tethering and* ***b,*** *strong tethering. For no tethering both orientations are equally distributed whereas for strong tethering monomers in blue appear shorter compared to red highlighted ones.* ***c,*** *Trend of the detachment length of left- (blue) and right-oriented (red) monomers with increasing tethering strength.*

The dependence of detachment length on the orientation of the first 20 monomers for L_{30} being either left- (red) or right-handed (blue) was additionally investigated (Fig. 5.6). A comparison between no pinning (Fig. 5.6**a**) and strong tethering (Fig. 5.6**b**) respectively already shows a trend for monomers marked in blue to have a lower average detachment length as opposed to red ones. This trend becomes more evident when plotting the detachment length versus the tethering strength k_{pin} (Fig. 5.6**c**, colors corresponding to orientation in **a** and **b**). This difference in detachment length could perhaps hint at a difference in adsorption-strengths or adsorption-heights of right- and left-handed monomers due to different commensurability of the monomers with the underlying surface.

After the successful stabilization of bonding orientation during the lifting experiment with sudden bond rupture, a second experiment was performed this time lifting for $\Delta z = 8$ nm and gently redepositioning the polymer back onto the surface rupturing the tip-molecule bond by applying a small bias pulse ($V_{\mathrm{pulse}} = 0.5$ V) to the tip. The experimental data is again accompanied by MD simulations of the lifting process, visible in Fig. 5.7. The initial position of the polymer along with the orientation of each monomer superimposed over the STM image is pictured in Fig. 5.7**b**.

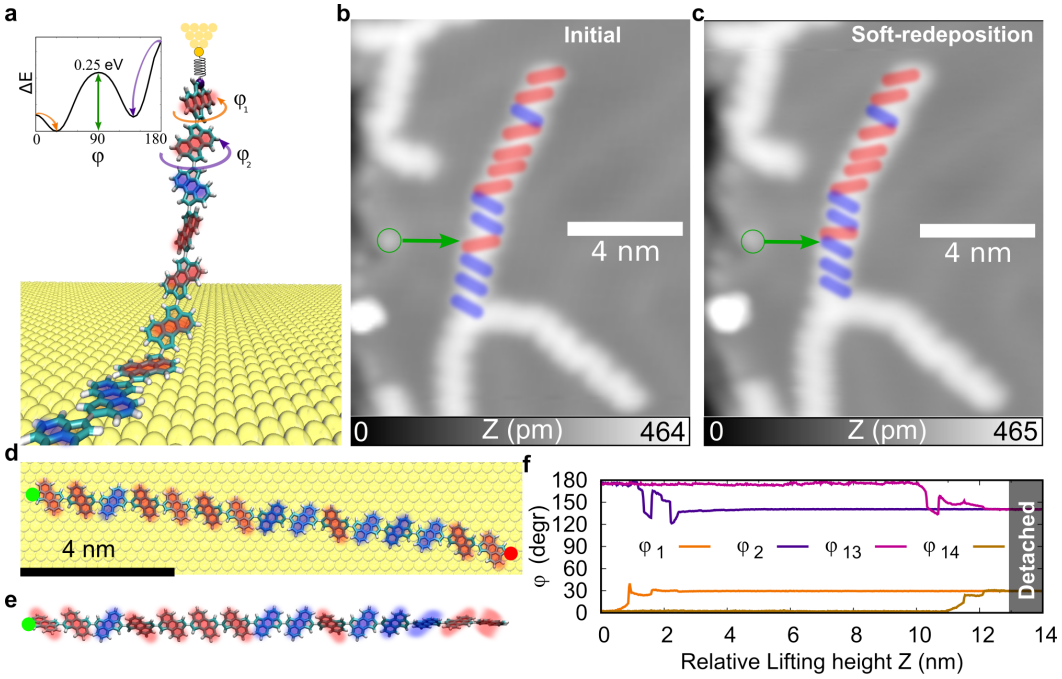

Figure 5.7: ***Mechanical stabilization of a lifted and redepositioned polymer. a,*** *MD-simulation of the lifting experiment, snap-shot of the suspended polymer. Inset: rotational energy graph upon rotation around the aryl-aryl bond connecting two CPAA monomers. Equilibrium angles at* $\varphi_1 = 30°$ *and* $\varphi_2 = 140°$ *with energy barrier of* $\Delta E = 250$ meV *separating them.* ***b,*** *STM measurement of the initial polymer configuration and* ***c,*** *After the lifting-readsorption experiment. Highlighted are the orientations of the monomers.* ($I_{\text{setpoint}} = 1$ pA, $V_{\text{Bias}} = 0.5$ V) ***d,*** *MD-simulation of the initial polymer configuration on the surface and* ***e,*** *Configuration of the completely lifted polymer with monomers rotated into their equilibrium angles.* ***f,*** *Recorded rotation of the angles between the monomers (angles visible in* ***a****) without transition between equilibrium angles.*

This particular polymer is shorter compared to the one used in the first experiment, consisting of thirteen monomers with six oriented to the left (red) and seven to the right (blue) of the scan area. It is again tethered (bottom of Fig. 5.7**b**) resulting in a weaker tethering of the end compared to the first lifting experiment. After successful lifting and soft-readsorption the orientations of the subunits comprising the polymer are completely preserved (Fig. 5.7**c**). Even critical bond configurations, *i.e.* three consecutive antiparallel bonded monomers (Units $N = 2, 3, 4$ and $N = 9, 10, 11$) have been stabilized during the lifting and subsequent soft redepositioning. Nevertheless during the soft redepositioning the molecule changed its adsorption position on the surface lying closer to the step-edge than before the experiment (green mark and arrow in Figs. 5.7**b** and **c**).
An MD simulation reproducing the experiment was performed (Fig. 5.7) with **a** illustrating a momentary snapshot of the suspended polymer during the lifting simulation. The initial configuration of the simulation is depicted in Fig. 5.7**d** (configuration

adapted from the experiment) with the final configuration in gas-phase shown in **e**. The molecule was tethered on the position marked in red (right-hand side of **d**) and lifted at the position marked in green (left-hand side). Since in the MD simulation it is possible to extract the bond angles and therefore the configuration of the polymer in gas-phase without the need of readsorption as in the experiment the simulation was performed until the molecule was completely desorbed from the surface (Fig. 5.7**e**). It is already visible that the monomers retained their bond sequence albeit rotating into their respective equilibrium angle. Extracting the angles between the units of the polymer (*i.e.* φ_1 the angle between the first and second CPAA, φ_2 between second and third, etc.) Fig. 5.7**e** shows the rotation of the monomers into their equilibrium angles (with respect to the following monomer). Further rotation of the monomers away from these angles however was not detected during the simulation process since no deviation from the equilibrium angles to other values can be spotted.
Both simulation and experiment therefore confirm the stabilization of the sequences paving the way for research of atropoisomerism in polymeric chains.

Part III

Conclusion

Conclusion

The production of microelectronics and nanomechanics has reached a turning point in length scales, density and energy efficiency that can not be further realized with classical top-down processes. New methods have to be developed and implemented in order to increase the density of components in microelectronics and reduce wear and degradation in nanomachinery such as quantum dots for data storage and nanorobots for medical applications. Due to the macroscopic scale of the tools that are used production of quantum dots and nanorobots is still challenging. One possible solution to these problems is bottom-up fabrication using organic molecules on metal surfaces due to their ability to be synthesized in abundance and to easily be designed specifically for the desired function. Understanding and characterizing the interaction of organic molecules with metal surfaces is therefore of utmost importance.
This work investigated both self-assembled supramolecular networks and on-surface synthesized polymers from organic molecules on noble metal surfaces using STM, FM-AFM with modified tip, STS and force spectroscopy. The results were accompanied by molecular dynamics (MD) simulations and density functional theory (DFT) calculations.

In Chapter 3, *2,7-dihydroxypyrene* (DHP) molecules were assembled on *Ag*(111) into two nanoporous networks (α and β). While the α-assembly consisted of only hexagonal pores constructed from six DHP molecules the β incorporated three-, six-, eight- and nine member pores.
Investigation of the electronic structure of the α-array revealed an energetic and spatial confinement of the surface electrons into the cavities of the network forming a quantum dot array (QDA). A Kronig-Penney model was used to rationalize the interaction of the quantum-dots and formation of an electronic band.
The electronic structure of the β-array was investigated similarly to the α-QDA. The eigenenergies of the confinements were uncovered, showing a weaker confinement for bigger pores compared to smaller ones. A decrease of the eigenenergy of six-member pores in the β-array compared to the value in the α-assembly was hypothesized to be a result of the surface electrons not being confined as strongly due to the different

surrounding cavities in the β-array.
The quantum dot arrays were further investigated using electrostatic force spectroscopy that unveiled a difference in quantum capacitance of the assemblies. This quantum capacitance could additionally be measured by mechanical dissipation using AFM [114]. Utilizing the mechanical dissipation and modelled quantum capacitance, the interdot tunneling rates Γ were calculated. Self-assembly of organic molecules into supramolecular networks thus enables for easy creation of QDAs that can potentially be utilized in electronic storage devices. Oxidation of the precursor molecules by means of removing hydrogen from hydroxyl-groups could be utilized in the steered assembly of mixed-pore networks to specifically alter the electronic behavior of the QDA.

In Chapter 4, a halogen-substituted pyrene derivate was used to investigate the influence of halogen position on the polymerization reaction as well as on the molecule-surface interaction. Pyrene based precursors can, depending on the position of the halogen atoms, be used to synthesize long regular polymers from *2,7-dibromopyrene* (Chapter 4.1.1) or pGNRs from *1,6-dibromopyrene* (Chapter 4.2.1) on $Au(111)$ to investigate adsorption mechanics, friction forces and dynamics of single monomers of suspended molecules.
In Chapter 4.1.2, long physisorbed *poly(2,7)-pyrenylene* chains were lifted from the surface of a $Au(111)$ sample. The effective stiffness k_{eff} of the tip-molecule system was recorded using the tip of an AFM revealing two alternating detachment periods. Comparing the experiment with MD simulations revealed the bigger and smaller detachment lengths to be a result of clockwise or anticlockwise monomer rotation upon desorption from the surface. In a MD simulation the motion of the tail end was modelled exposing a rotation of the tail away from the pulling axis ($\left[11\bar{2}\right]$) and mainly moving in the $\left[0\bar{1}1\right]$ and $\left[\bar{1}01\right]$ directions (Chapter 4.1.3).
In Chapter 4.1.4, the *poly(2,7)-pyrenylene* chains were furthermore pulled at increasing heights along the fcc valley of the reconstructed $Au(111)$ surface. The friction maps recorded revealed a strong and weak adsorption regime at the single monomer level that changes the movement dynamics of the whole molecule from small stick-slip jumps to irregular jumps. The weak and strong regime were unveiled to be a result of the clockwise or anticlockwise rotation of the lifted monomer resulting in steric repulsion between hydrogen atoms of the lifted and still adsorbed neighboring monomers. The backward motion during the sliding experiments was investigated to behave similarly to the forward motion giving insight into the stability and rigidity of the *C-C* bond connecting the monomers. A *1,6-dibromopyrene* precursor was used in Chapter 4.2 to synthesize pGNRs that were used in lifting and sliding experiments to compare with the motion of the *poly(2,7)-pyrenylene* chains and regular armchair GNRs on $Au(111)$. The $k_{\text{eff}}(X,Y)$-maps revealed changing patterns depending on the lifting height of the head atom without changing into a weak regime, as opposed to the case of *poly(2,7)-pyrenylene*. The sliding motion resembled the behavior of regular armchair-GNRs previously reported on by Kawai *et al.* [1]. This molecular manipulation by cryo force-spectroscopy and sliding experiments can therefore be used to gain insight into the influence of monomer rotation, flexibility and rigidity on the behavior of suspended polymers. Unravelling the motion dynamics on the single monomer

level by experimental force-spectroscopy in conjunction with simulations furthers the understanding of molecular processes upon desorption and diffusion.

In Chapter 5, *1,6-cyclopenta[h,i]aceanthrylene* (CPAA) was utilized to synthesize sterically frustrated polymers on $Au(111)$ for lifting experiments. Investigation of the polymers by AFM revealed two different bonding configurations (parallel/antiparallel). The uniform contrast in the AFM images of the antiparallel configuration unveiled the surface adsorption energy to surpass the steric repulsion of the adjacent hydrogen atoms of neighboring monomers.
Cryo force-spectroscopy measurements (Chapter 5.2) with additional redepositioning of the polymer unveiled repeating dips in the frequency shift graphs that were attributed to detachment and readsorption events of monomers. The lifting and redepositioning graphs were in good agreement showing only small differences. STM images before and after the lifting revealed a stabilization of the bond conformations in the redepositioned part with only few monomers closer to the tip changing orientation due to introduced vibrational energy upon tip-molecule bond rupture. The retention of the bond conformations was hypothesized to be a result of the stabilizing character of the conjugated π-system. The influence of the pinning strength of the last carbon atom as well as the polymer length on the lifting dynamics, *i.e.* detachment lengths and lifting angle, was investigated by MD simulations to correctly model the experimental lifting data.
A subsequent manipulation experiment was performed by soft-redepositioning of a CPAA polymer back onto the surface. During the process the monomers retained their orientation, which was demonstrated by MD simulations. The simulations showed rotation of the monomers into their respective equilibrium angle without further rotation, confirming the stabilization of the backbone due to the conjugated system. The concept of reversible cryo force-spectroscopy with all-atom molecular dynamics simulations shown in these experiments can thus be used to further the knowledge of stabilizing factors in the synthesis of organic polymers. Understanding these factors enables for the precise engineering of polymers from precursor molecules that exhibit the desired stability or flexibility.

Bibliography

[1] S. Kawai, A. Benassi, E. Gnecco, H. Sode, R. Pawlak, X. Feng, K. Mullen, D. Passerone, C. A. Pignedoli, P. Ruffieux, R. Fasel, and E. Meyer. Superlubricity of graphene nanoribbons on gold surfaces. Science, 351(6276):957–961, February 2016.

[2] J. Bardeen and W. H. Brattain. The Transistor, A Semi-Conductor Triode. Phys. Rev., 74(2):230–231, July 1948. Publisher: American Physical Society.

[3] Hassan Mujtaba. AMD 2nd Gen EPYC Rome Processors Feature A Gargantuan 39.54 Billion Transistors, IO Die Pictured in Detail, October 2019. Publication Title: Wccftech.

[4] Manjula Vijh, R. S. Gupta, and Sujata Pandey. Graphene Based Tunnel Field Effect Transistor for RF Applications. In 2019 PhotonIcs Electromagnetics Research Symposium - Spring (PIERS-Spring), pages 256–259, June 2019. ISSN: 1559-9450.

[5] Tahereh Radsar, Hassan Khalesi, and Vahid Ghods. Graphene nanoribbon field effect transistors analysis and applications. Superlattices and Microstructures, 153:106869, May 2021.

[6] Virat Khanna, Vanish Kumar, and Suneev Anil Bansal. Mechanical properties of aluminium-graphene/carbon nanotubes (CNTs) metal matrix composites: Advancement, opportunities and perspective. Materials Research Bulletin, 138:111224, June 2021.

[7] Yinxiang Zeng, Xiyue Zhang, Ruofei Qin, Xiaoqing Liu, Pingping Fang, Dezhou Zheng, Yexiang Tong, and Xihong Lu. Dendrite-Free Zinc Deposition Induced by Multifunctional CNT Frameworks for Stable Flexible Zn-Ion Batteries. Advanced Materials, 31(36):1903675, 2019. _eprint: https://onlinelibrary.wiley.com/doi/pdf/10.1002/adma.201903675.

[8] Ting Zhu, Baoyu Xia, Liang Zhou, and Xiong Wen (David) Lou. Arrays of ultrafine CuS nanoneedles supported on a CNT backbone for application in supercapacitors. Journal of Materials Chemistry, 22(16):7851–7855, 2012. Publisher: Royal Society of Chemistry.

[9] Jinming Cai, Pascal Ruffieux, Rached Jaafar, Marco Bieri, Thomas Braun, Stephan Blankenburg, Matthias Muoth, Ari P. Seitsonen, Moussa Saleh, Xinliang Feng, Klaus Müllen, and Roman Fasel. Atomically precise bottom-up fabrication of graphene nanoribbons. Nature, 466(7305):470–473, July 2010.

[10] Rémy Pawlak, Xunshan Liu, Silviya Ninova, Philipp D'Astolfo, Carl Drechsel, Sara Sangtarash, Robert Häner, Silvio Decurtins, Hatef Sadeghi, Colin J. Lambert, Ulrich Aschauer, Shi-Xia Liu, and Ernst Meyer. Bottom-up Synthesis of Nitrogen-Doped Porous Graphene Nanoribbons. J. Am. Chem. Soc., 142(29):12568–12573, July 2020.

[11] Pascal Ruffieux, Shiyong Wang, Bo Yang, Carlos Sanchez, Jia Liu, Thomas Dienel, Leopold Talirz, Prashant Shinde, Carlo A. Pignedoli, Daniele Passerone, Tim Dumslaff, Xinliang Feng, Klaus Muellen, and Roman Fasel. On-surface synthesis of graphene nanoribbons with zigzag edge topology. Nature, 531(7595):489–492, March 2016. arXiv: 1511.05037.

[12] Leopold Talirz, Pascal Ruffieux, and Roman Fasel. On-Surface Synthesis of Atomically Precise Graphene Nanoribbons. Adv. Mater., 28(29):6222–6231, August 2016.

[13] F. Klappenberger, D. Kühne, W. Krenner, I. Silanes, A. Arnau, F. J. García de Abajo, S. Klyatskaya, M. Ruben, and J. V. Barth. Tunable Quantum Dot Arrays Formed from Self-Assembled Metal-Organic Networks. Phys. Rev. Lett., 106(2):026802, January 2011.

[14] G. Binnig and H. Rohrer. Scanning tunneling microscopy. Surface Science, 126(1):236–244, March 1983.

[15] G. Binnig, H. Rohrer, Ch. Gerber, and E. Weibel. Surface Studies by Scanning Tunneling Microscopy. Phys. Rev. Lett., 49(1):57–61, July 1982. Publisher: American Physical Society.

[16] G Binnig, Ch Gerber, E Stoll, T. R Albrecht, and C. F Quate. Atomic Resolution with Atomic Force Microscope. Europhysics Letters (EPL), 3(12):1281–1286, June 1987. Publisher: IOP Publishing.

[17] G. Binnig, C. F. Quate, and Ch. Gerber. Atomic Force Microscope. Phys. Rev. Lett., 56(9):930–933, March 1986. Publisher: American Physical Society.

[18] Leo Gross, Bruno Schuler, Fabian Mohn, Nikolaj Moll, Jascha Repp, and Gerhard Meyer. Atomic Resolution on Molecules with Functionalized Tips. In Seizo Morita, Franz J. Giessibl, Ernst Meyer, and Roland Wiesendanger, editors, Noncontact Atomic Force Microscopy: Volume 3, NanoScience and Technology, pages 223–246. Springer International Publishing, Cham, 2015.

[19] S. Kawai, M. Koch, E. Gnecco, A. Sadeghi, R. Pawlak, T. Glatzel, J. Schwarz, S. Goedecker, S. Hecht, A. Baratoff, L. Grill, and E. Meyer. Quantifying the

atomic-level mechanics of single long physisorbed molecular chains. Proceedings of the National Academy of Sciences, 111(11):3968–3972, March 2014.

[20] Sara Freund, Rémy Pawlak, Lucas Moser, Antoine Hinaut, Roland Steiner, Nathalie Marinakis, Edwin C. Constable, Ernst Meyer, Catherine E. Housecroft, and Thilo Glatzel. Transoid-to-Cisoid Conformation Changes of Single Molecules on Surfaces Triggered by Metal Coordination. ACS Omega, 3(10):12851–12856, October 2018. Publisher: American Chemical Society.

[21] Shadi Fatayer, Florian Albrecht, Yunlong Zhang, Darius Urbonas, Diego Peña, Nikolaj Moll, and Leo Gross. Molecular structure elucidation with charge-state control. Science, 365(6449):142–145, July 2019. Publisher: American Association for the Advancement of Science Section: Report.

[22] Rémy Pawlak, J. G. Vilhena, Antoine Hinaut, Tobias Meier, Thilo Glatzel, Alexis Baratoff, Enrico Gnecco, Rubén Pérez, and Ernst Meyer. Conformations and cryo-force spectroscopy of spray-deposited single-strand DNA on gold. Nat Commun, 10(1):685, December 2019.

[23] Dirk Kühne, Florian Klappenberger, Régis Decker, Uta Schlickum, Harald Brune, Svetlana Klyatskaya, Mario Ruben, and Johannes V. Barth. High-Quality 2D Metal-Organic Coordination Network Providing Giant Cavities within Mesoscale Domains. J. Am. Chem. Soc., 131(11):3881–3883, March 2009.

[24] Kathrin Müller, Mihaela Enache, and Meike Stöhr. Confinement properties of 2D porous molecular networks on metal surfaces. J. Phys.: Condens. Matter, 28(15):153003, March 2016.

[25] Jorge Lobo-Checa, Manfred Matena, Kathrin Müller, Jan Hugo Dil, Fabian Meier, Lutz H. Gade, Thomas A. Jung, and Meike Stöhr. Band Formation from Coupled Quantum Dots Formed by a Nanoporous Network on a Copper Surface. Science, 325(5938):300–303, July 2009.

[26] Zhenghao Hu, Jian Wang, Xiaoling Ma, Jinhua Gao, Chunyu Xu, Kaixuan Yang, Zhi Wang, Jian Zhang, and Fujun Zhang. A critical review on semitransparent organic solar cells. Nano Energy, 78:105376, December 2020.

[27] Tobias Meier, Rémy Pawlak, Shigeki Kawai, Yan Geng, Xunshan Liu, Silvio Decurtins, Prokop Hapala, Alexis Baratoff, Shi-Xia Liu, Pavel Jelínek, Ernst Meyer, and Thilo Glatzel. Donor–Acceptor Properties of a Single-Molecule Altered by On-Surface Complex Formation. ACS Nano, 11(8):8413–8420, August 2017. Publisher: American Chemical Society.

[28] Nan Sun, Chengming Jiang, Qikun Li, Dongchen Tan, Sheng Bi, and Jinhui Song. Performance of OLED under mechanical strain: a review. J Mater Sci: Mater Electron, 31(23):20688–20729, December 2020.

[29] Andrey K. Geim and Allan H. MacDonald. Graphene: Exploring carbon flatland. Physics Today, 60(8):35–41, August 2007. Publisher: American Institute of Physics.

[30] Valeria Alzari, Daniele Nuvoli, Sergio Scognamillo, Massimo Piccinini, Emilia Gioffredi, Giulio Malucelli, Salvatore Marceddu, Mario Sechi, Vanna Sanna, and Alberto Mariani. Graphene-containing thermoresponsive nanocomposite hydrogels of poly(N-isopropylacrylamide) prepared by frontal polymerization. J. Mater. Chem., 21(24):8727–8733, June 2011. Publisher: The Royal Society of Chemistry.

[31] Yenny Hernandez, Valeria Nicolosi, Mustafa Lotya, Fiona M. Blighe, Zhenyu Sun, Sukanta De, I. T. McGovern, Brendan Holland, Michele Byrne, Yurii K. Gun'Ko, John J. Boland, Peter Niraj, Georg Duesberg, Satheesh Krishnamurthy, Robbie Goodhue, John Hutchison, Vittorio Scardaci, Andrea C. Ferrari, and Jonathan N. Coleman. High-yield production of graphene by liquid-phase exfoliation of graphite. Nature Nanotech, 3(9):563–568, September 2008.

[32] Daniele Nuvoli, Luca Valentini, Valeria Alzari, Sergio Scognamillo, Silvia Bittolo Bon, Massimo Piccinini, Javier Illescas, and Alberto Mariani. High concentration few-layer graphene sheets obtained by liquid phase exfoliation of graphite in ionic liquid. J. Mater. Chem., 21(10):3428–3431, February 2011. Publisher: The Royal Society of Chemistry.

[33] Buddhika Jayasena and Sathyan Subbiah. A novel mechanical cleavage method for synthesizing few-layer graphenes. Nanoscale Research Letters, 6(1):95, January 2011.

[34] Nihar Mohanty, David Moore, Zhiping Xu, T. S. Sreeprasad, Ashvin Nagaraja, Alfredo Alexander Rodriguez, and Vikas Berry. Nanotomy-based production of transferable and dispersible graphene nanostructures of controlled shape and size. Nat Commun, 3(1):844, May 2012.

[35] Zhihong Chen, Yu-Ming Lin, Michael J. Rooks, and Phaedon Avouris. Graphene nano-ribbon electronics. Physica E: Low-dimensional Systems and Nanostructures, 40(2):228–232, December 2007.

[36] Melinda Y. Han, Barbaros Özyilmaz, Yuanbo Zhang, and Philip Kim. Energy Band-Gap Engineering of Graphene Nanoribbons. Phys. Rev. Lett., 98(20):206805, May 2007. Publisher: American Physical Society.

[37] L. A. Ponomarenko, F. Schedin, M. I. Katsnelson, R. Yang, E. W. Hill, K. S. Novoselov, and A. K. Geim. Chaotic Dirac Billiard in Graphene Quantum Dots. Science, April 2008. Publisher: American Association for the Advancement of Science.

[38] Levente Tapasztó, Gergely Dobrik, Philippe Lambin, and László P. Biró. Tailoring the atomic structure of graphene nanoribbons by scanning tunnelling microscope lithography. Nature Nanotech, 3(7):397–401, July 2008.

[39] Liying Jiao, Li Zhang, Xinran Wang, Georgi Diankov, and Hongjie Dai. Narrow graphene nanoribbons from carbon nanotubes. Nature, 458(7240):877–880, April 2009.

[40] Dmitry V. Kosynkin, Amanda L. Higginbotham, Alexander Sinitskii, Jay R. Lomeda, Ayrat Dimiev, B. Katherine Price, and James M. Tour. Longitudinal unzipping of carbon nanotubes to form graphene nanoribbons. Nature, 458(7240):872–876, April 2009.

[41] Sithara P. Sreenilayam, Inam Ul Ahad, Valeria Nicolosi, Victor Acinas Garzon, and Dermot Brabazon. Advanced materials of printed wearables for physiological parameter monitoring. Materials Today, 32:147–177, January 2020.

[42] Ali K. Yetisen, Juan Leonardo Martinez-Hurtado, Barış Ünal, Ali Khademhosseini, and Haider Butt. Wearables in Medicine. Advanced Materials, 30(33):1706910, 2018. _eprint: https://onlinelibrary.wiley.com/doi/pdf/10.1002/adma.201706910.

[43] A. N. M. Alamgir. Drugs: Their Natural, Synthetic, and Biosynthetic Sources. In A.N.M. Alamgir, editor, Therapeutic Use of Medicinal Plants and Their Extracts: Volume 1: Pharmacognosy, Progress in Drug Research, pages 105–123. Springer International Publishing, Cham, 2017.

[44] Sumio Iijima. Helical microtubules of graphitic carbon. Nature, 354(6348):56–58, November 1991.

[45] Ting Guo, Pavel Nikolaev, Andrew G. Rinzler, David Tomanek, Daniel T. Colbert, and Richard E. Smalley. Self-Assembly of Tubular Fullerenes. J. Phys. Chem., 99(27):10694–10697, July 1995. Publisher: American Chemical Society.

[46] Naoki Ishigami, Hiroki Ago, Kenta Imamoto, Masaharu Tsuji, Konstantin Iakoubovskii, and Nobutsugu Minami. Crystal Plane Dependent Growth of Aligned Single-Walled Carbon Nanotubes on Sapphire. J. Am. Chem. Soc., 130(30):9918–9924, July 2008. Publisher: American Chemical Society.

[47] M. José-Yacamán, M. Miki-Yoshida, L. Rendón, and J. G. Santiesteban. Catalytic growth of carbon microtubules with fullerene structure. Appl. Phys. Lett., 62(6):657–659, February 1993. Publisher: American Institute of Physics.

[48] Mukul Kumar and Yoshinori Ando. Chemical Vapor Deposition of Carbon Nanotubes: A Review on Growth Mechanism and Mass Production. Journal of Nanoscience and Nanotechnology, 10(6):3739–3758, June 2010.

[49] Qitang Fan, Daniel Martin-Jimenez, Daniel Ebeling, Claudio K. Krug, Lea Brechmann, Corinna Kohlmeyer, Gerhard Hilt, Wolfgang Hieringer, André Schirmeisen, and J. Michael Gottfried. Nanoribbons with Nonalternant Topology from Fusion of Polyazulene: Carbon Allotropes beyond Graphene. J. Am. Chem. Soc., 141(44):17713–17720, November 2019. Publisher: American Chemical Society.

[50] Martin Knudsen. Die Molekularströmung der Gase durch Offnungen und die Effusion. Annalen der Physik, 333(5):999–1016, 1909. _eprint: https://onlinelibrary.wiley.com/doi/pdf/10.1002/andp.19093330505.

[51] Christopher J. Satterley, Luís M. A. Perdigão, Alex Saywell, Graziano Magnano, Anna Rienzo, Louise C. Mayor, Vinod R. Dhanak, Peter H. Beton, and James N. O'Shea. Electrospray deposition of fullerenes in ultra-high vacuum:in situscanning tunneling microscopy and photoemission spectroscopy. Nanotechnology, 18(45):455304, October 2007. Publisher: IOP Publishing.

[52] Janine C. Swarbrick, J. Ben Taylor, and James N. O'Shea. Electrospray deposition in vacuum. Applied Surface Science, 252(15):5622–5626, May 2006.

[53] Johannes V. Barth. Molecular Architectonic on Metal Surfaces. Annual Review of Physical Chemistry, 58(1):375–407, 2007. _eprint: https://doi.org/10.1146/annurev.physchem.56.092503.141259.

[54] George M. Whitesides, John P. Mathias, and Christopher T. Seto. Molecular Self-Assembly and Nanochemistry: a Chemical Strategy for the Synthesis of Nanostructures. Science, November 1991. Publisher: American Association for the Advancement of Science.

[55] Stefan Griessl, Markus Lackinger, Michael Edelwirth, Michael Hietschold, and Wolfgang M. Heckl. Self-Assembled Two-Dimensional Molecular Host-Guest Architectures From Trimesic Acid. Single Molecules, 3(1):25–31, 2002. _eprint: https://onlinelibrary.wiley.com/doi/pdf/10.1002/1438-5171%28200204%293%3A1%3C25%3A%3AAID-SIMO25%3E3.0.CO%3B2-K.

[56] A. Dmitriev, N. Lin, J. Weckesser, J. V. Barth, and K. Kern. Supramolecular Assemblies of Trimesic Acid on a Cu(100) Surface. J. Phys. Chem. B, 106(27):6907–6912, July 2002. Publisher: American Chemical Society.

[57] Ignacio Piquero-Zulaica, Jorge Lobo-Checa, Ali Sadeghi, Zakaria M. Abd El-Fattah, Chikahiko Mitsui, Toshihiro Okamoto, Rémy Pawlak, Tobias Meier, Andrés Arnau, J. Enrique Ortega, Jun Takeya, Stefan Goedecker, Ernst Meyer, and Shigeki Kawai. Precise engineering of quantum dot array coupling through their barrier widths. Nat Commun, 8(1):787, December 2017.

[58] Ignacio Piquero-Zulaica, Zakaria M Abd El-Fattah, Olha Popova, Shigeki Kawai, Sylwia Nowakowska, Manfred Matena, Mihaela Enache, Meike Stöhr, Antonio Tejeda, Amina Taleb, Ernst Meyer, J Enrique Ortega, Lutz H Gade, Thomas A

Jung, and Jorge Lobo-Checa. Effective determination of surface potential landscapes from metal-organic nanoporous network overlayers. New Journal of Physics, 21(5):053004, 2019. Publisher: IOP Publishing.

[59] Gelavizh Ahmadi and Katharina J. Franke. Self-assembly of tetracyanonaphthoquinodimethane (TNAP) based metal–organic networks on Pb(111): Structural, electronic, and magnetic properties. Applied Surface Science, 373:2–7, June 2016.

[60] David Écija, Knud Seufert, Daniel Heim, Willi Auwärter, Claudia Aurisicchio, Chiara Fabbro, Davide Bonifazi, and Johannes V. Barth. Hierarchic Self-Assembly of Nanoporous Chiral Networks with Conformationally Flexible Porphyrins. ACS Nano, 4(8):4936–4942, August 2010. Publisher: American Chemical Society.

[61] Brian D. Adams and Aicheng Chen. The role of palladium in a hydrogen economy. Materials Today, 14(6):282–289, June 2011.

[62] Saw-Wai Hla, Ludwig Bartels, Gerhard Meyer, and Karl-Heinz Rieder. Inducing All Steps of a Chemical Reaction with the Scanning Tunneling Microscope Tip: Towards Single Molecule Engineering. Phys. Rev. Lett., 85(13):2777–2780, September 2000. Publisher: American Physical Society.

[63] F. Ullmann and Jean Bielecki. Ueber Synthesen in der Biphenylreihe. Ber. Dtsch. Chem. Ges., 34(2):2174–2185, May 1901.

[64] Leonhard Grill, Matthew Dyer, Leif Lafferentz, Mats Persson, Maike V. Peters, and Stefan Hecht. Nano-architectures by covalent assembly of molecular building blocks. Nature Nanotech, 2(11):687–691, November 2007. Number: 11 Publisher: Nature Publishing Group.

[65] Matthew O. Blunt, James C. Russell, Neil R. Champness, and Peter H. Beton. Templating molecular adsorption using a covalent organic framework. Chemical Communications, 46(38):7157–7159, 2010. Publisher: Royal Society of Chemistry.

[66] Marco Bieri, Manh-Thuong Nguyen, Oliver Gröning, Jinming Cai, Matthias Treier, Kamel Aït-Mansour, Pascal Ruffieux, Carlo A. Pignedoli, Daniele Passerone, Marcel Kastler, Klaus Müllen, and Roman Fasel. Two-Dimensional Polymer Formation on Surfaces: Insight into the Roles of Precursor Mobility and Reactivity. J. Am. Chem. Soc., 132(46):16669–16676, November 2010. Publisher: American Chemical Society.

[67] Johanna Eichhorn, Damian Nieckarz, Oliver Ochs, Debabrata Samanta, Michael Schmittel, Pawel Jerzy Szabelski, and Markus Lackinger. On-Surface Ullmann Coupling: The Influence of Kinetic Reaction Parameters on the Morphology and Quality of Covalent Networks. ACS Nano, 8(8):7880–7889, August 2014. Publisher: American Chemical Society.

[68] Jia Liu, Pascal Ruffieux, Xinliang Feng, Klaus Müllen, and Roman Fasel. Cyclotrimerization of arylalkynes on Au(111). Chemical Communications, 50(76):11200–11203, 2014. Publisher: Royal Society of Chemistry.

[69] Yi-Qi Zhang, Nenad Kepčija, Martin Kleinschrodt, Katharina Diller, Sybille Fischer, Anthoula C. Papageorgiou, Francesco Allegretti, Jonas Björk, Svetlana Klyatskaya, Florian Klappenberger, Mario Ruben, and Johannes V. Barth. Homo-coupling of terminal alkynes on a noble metal surface. Nat Commun, 3(1):1286, December 2012.

[70] Haitao Zhou, Jianzhao Liu, Shixuan Du, Lizhi Zhang, Geng Li, Yi Zhang, Ben Zhong Tang, and Hong-Jun Gao. Direct Visualization of Surface-Assisted Two-Dimensional Diyne Polycyclotrimerization. J. Am. Chem. Soc., 136(15):5567–5570, April 2014. Publisher: American Chemical Society.

[71] Qitang Fan, Cici Wang, Yong Han, Junfa Zhu, Wolfgang Hieringer, Julian Kuttner, Gerhard Hilt, and J. Michael Gottfried. Surface-Assisted Organic Synthesis of Hyperbenzene Nanotroughs. Angewandte Chemie International Edition, 52(17):4668–4672, 2013. _eprint: https://onlinelibrary.wiley.com/doi/pdf/10.1002/anie.201300610.

[72] Leif Lafferentz, Francisco Ample, Hao Yu, Stefan Hecht, Christian Joachim, and Leonhard Grill. Conductance of a Single Conjugated Polymer as a Continuous Function of Its Length. Science, 323(5918):1193–1197, February 2009. Publisher: American Association for the Advancement of Science Section: Report.

[73] Shigeki Kawai, Ali Sadeghi, Toshihiro Okamoto, Chikahiko Mitsui, Rémy Pawlak, Tobias Meier, Jun Takeya, Stefan Goedecker, and Ernst Meyer. Organometallic Bonding in an Ullmann-Type On-Surface Chemical Reaction Studied by High-Resolution Atomic Force Microscopy. Small, 12(38):5303–5311, October 2016.

[74] Sören Zint, Daniel Ebeling, Tobias Schlöder, Sebastian Ahles, Doreen Mollenhauer, Hermann A. Wegner, and André Schirmeisen. Imaging Successive Intermediate States of the On-Surface Ullmann Reaction on Cu(111): Role of the Metal Coordination. ACS Nano, 11(4):4183–4190, April 2017. Publisher: American Chemical Society.

[75] Maria El Abbassi, Mickael L. Perrin, Gabriela Borin Barin, Sara Sangtarash, Jan Overbeck, Oliver Braun, Colin J. Lambert, Qiang Sun, Thorsten Prechtl, Akimitsu Narita, Klaus Müllen, Pascal Ruffieux, Hatef Sadeghi, Roman Fasel, and Michel Calame. Controlled Quantum Dot Formation in Atomically Engineered Graphene Nanoribbon Field-Effect Transistors. ACS Nano, 14(5):5754–5762, May 2020. Publisher: American Chemical Society.

[76] Aishah Khalid, Jahariah Sampe, Burhanuddin Yeop Majlis, Mohd Ambri Mohamed, Takuo Chikuba, Takuya Iwasaki, and Hiroshi Mizuta. Towards high per-

formance graphene nanoribbon transistors (GNR-FETs). In 2015 IEEE Regional Symposium on Micro and Nanoelectronics (RSM), pages 1–4, August 2015.

[77] Gonzalo Otero, Giulio Biddau, Carlos Sánchez-Sánchez, Renaud Caillard, María F. López, Celia Rogero, F. Javier Palomares, Noemí Cabello, Miguel A. Basanta, José Ortega, Javier Méndez, Antonio M. Echavarren, Rubén Pérez, Berta Gómez-Lor, and José A. Martín-Gago. Fullerenes from aromatic precursors by surface-catalysed cyclodehydrogenation. Nature, 454(7206):865–868, August 2008.

[78] Matthias Treier, Carlo Antonio Pignedoli, Teodoro Laino, Ralph Rieger, Klaus Müllen, Daniele Passerone, and Roman Fasel. Surface-assisted cyclodehydrogenation provides a synthetic route towards easily processable and chemically tailored nanographenes. Nat Chem, 3(1):61–67, January 2011.

[79] Daniel J. Rizzo, Gregory Veber, Ting Cao, Christopher Bronner, Ting Chen, Fangzhou Zhao, Henry Rodriguez, Steven G. Louie, Michael F. Crommie, and Felix R. Fischer. Topological band engineering of graphene nanoribbons. Nature, 560(7717):204–208, August 2018. Number: 7717 Publisher: Nature Publishing Group.

[80] Oliver Gröning, Shiyong Wang, Xuelin Yao, Carlo A. Pignedoli, Gabriela Borin Barin, Colin Daniels, Andrew Cupo, Vincent Meunier, Xinliang Feng, Akimitsu Narita, Klaus Müllen, Pascal Ruffieux, and Roman Fasel. Engineering of robust topological quantum phases in graphene nanoribbons. Nature, 560(7717):209–213, August 2018. Number: 7717 Publisher: Nature Publishing Group.

[81] Qiang Sun, Oliver Gröning, Jan Overbeck, Oliver Braun, Mickael L. Perrin, Gabriela Borin Barin, Maria El Abbassi, Kristjan Eimre, Edward Ditler, Colin Daniels, Vincent Meunier, Carlo A. Pignedoli, Michel Calame, Roman Fasel, and Pascal Ruffieux. Massive Dirac Fermion Behavior in a Low Bandgap Graphene Nanoribbon Near a Topological Phase Boundary. Advanced Materials, 32(12):1906054, 2020. _eprint: https://onlinelibrary.wiley.com/doi/pdf/10.1002/adma.201906054.

[82] C. Wagner, N. Fournier, F. S. Tautz, and R. Temirov. Measurement of the Binding Energies of the Organic-Metal Perylene-Teracarboxylic-Dianhydride/Au(111) Bonds by Molecular Manipulation Using an Atomic Force Microscope. Phys. Rev. Lett., 109(7):076102, August 2012.

[83] Matthias Rief, Filipp Oesterhelt, Berthold Heymann, and Hermann E. Gaub. Single Molecule Force Spectroscopy on Polysaccharides by Atomic Force Microscopy. Science, 275(5304):1295–1297, February 1997.

[84] Rémy Pawlak, J. G. Vilhena, Philipp D'Astolfo, Xunshan Liu, Giacomo Prampolini, Tobias Meier, Thilo Glatzel, Justin A. Lemkul, Robert Häner, Silvio

Decurtins, Alexis Baratoff, Rubén Pérez, Shi-Xia Liu, and Ernst Meyer. Sequential Bending and Twisting around C–C Single Bonds by Mechanical Lifting of a Pre-Adsorbed Polymer. Nano Lett., 20(1):652–657, January 2020.

[85] Lorenzo Gigli, Shigeki Kawai, Roberto Guerra, Nicola Manini, Rémy Pawlak, Xinliang Feng, Klaus Müllen, Pascal Ruffieux, Roman Fasel, Erio Tosatti, Ernst Meyer, and Andrea Vanossi. Detachment Dynamics of Graphene Nanoribbons on Gold. ACS Nano, 13(1):689–697, January 2019. Publisher: American Chemical Society.

[86] Christian Wagner, Norman Fournier, Victor G. Ruiz, Chen Li, Klaus Müllen, Michael Rohlfing, Alexandre Tkatchenko, Ruslan Temirov, and F. Stefan Tautz. Non-additivity of molecule-surface van der Waals potentials from force measurements. Nat Commun, 5(1):5568, November 2014.

[87] Rémy Pawlak, Wengen Ouyang, Alexander E. Filippov, Lena Kalikhman-Razvozov, Shigeki Kawai, Thilo Glatzel, Enrico Gnecco, Alexis Baratoff, Quanshui Zheng, Oded Hod, Michael Urbakh, and Ernst Meyer. Single-Molecule Tribology: Force Microscopy Manipulation of a Porphyrin Derivative on a Copper Surface. ACS Nano, 10(1):713–722, January 2016. Publisher: American Chemical Society.

[88] R Pawlak, S Kawai, T Meier, T Glatzel, A Baratoff, and E Meyer. Single-molecule manipulation experiments to explore friction and adhesion. J. Phys. D: Appl. Phys., 50(11):113003, March 2017.

[89] J. Bardeen. Tunnelling from a Many-Particle Point of View. Phys. Rev. Lett., 6(2):57–59, January 1961. Publisher: American Physical Society.

[90] Michael Schmid. Schematic diagram of a scanning tunneling microscope, June 2005.

[91] Xiangying Deng, Fang Xiong, Xiayu Li, Bo Xiang, Zheng Li, Xu Wu, Can Guo, Xiaoling Li, Yong Li, Guiyuan Li, Wei Xiong, and Zhaoyang Zeng. Application of atomic force microscopy in cancer research. Journal of Nanobiotechnology, 16(1):102, December 2018.

[92] M. A. Lantz, H. J. Hug, R. Hoffmann, P. J. A. van Schendel, P. Kappenberger, S. Martin, A. Baratoff, and H.-J. Güntherodt. Quantitative Measurement of Short-Range Chemical Bonding Forces. Science, 291(5513):2580–2583, March 2001. Publisher: American Association for the Advancement of Science Section: Report.

[93] S. Hudlet, M. Saint Jean, C. Guthmann, and J. Berger. Evaluation of the capacitive force between an atomic force microscopy tip and a metallic surface. Eur. Phys. J. B, 2(1):5–10, March 1998.

[94] H. C. Hamaker. The London—van der Waals attraction between spherical particles. Physica, 4(10):1058–1072, October 1937.

[95] Franz J. Giessibl. Advances in atomic force microscopy. Rev. Mod. Phys., 75(3):949–983, July 2003. Publisher: American Physical Society.

[96] Elisabeth Wutscher and Franz J. Giessibl. Atomic force microscopy at ambient and liquid conditions with stiff sensors and small amplitudes. Review of Scientific Instruments, 82(9):093703, September 2011. Publisher: American Institute of Physics.

[97] Franz J. Giessibl. High-speed force sensor for force microscopy and profilometry utilizing a quartz tuning fork. Appl. Phys. Lett., 73(26):3956–3958, December 1998. Publisher: American Institute of Physics.

[98] Franz J. Giessibl. The qPlus sensor, a powerful core for the atomic force microscope. Review of Scientific Instruments, 90(1):011101, January 2019. Publisher: American Institute of Physics.

[99] Y. Niimi, T. Matsui, H. Kambara, K. Tagami, M. Tsukada, and Hiroshi Fukuyama. Scanning tunneling microscopy and spectroscopy of the electronic local density of states of graphite surfaces near monoatomic step edges. Phys. Rev. B, 73(8):085421, February 2006. Publisher: American Physical Society.

[100] Umut Bostanci, M. Kurtuluş Abak, O. Aktaş, and A. Dâna. Nanoscale charging hysteresis measurement by multifrequency electrostatic force spectroscopy. Appl. Phys. Lett., 92(9):093108, March 2008. Publisher: American Institute of Physics.

[101] Shadi Fatayer, Bruno Schuler, Wolfram Steurer, Ivan Scivetti, Jascha Repp, Leo Gross, Mats Persson, and Gerhard Meyer. Reorganization energy upon charging a single molecule on an insulator measured by atomic force microscopy. Nature Nanotech, 13(5):376–380, May 2018.

[102] Leo Gross, Fabian Mohn, Peter Liljeroth, Jascha Repp, Franz J. Giessibl, and Gerhard Meyer. Measuring the Charge State of an Adatom with Noncontact Atomic Force Microscopy. Science, 324(5933):1428–1431, June 2009. Publisher: American Association for the Advancement of Science Section: Report.

[103] Alexander Kerelsky, Leo J. McGilly, Dante M. Kennes, Lede Xian, Matthew Yankowitz, Shaowen Chen, K. Watanabe, T. Taniguchi, James Hone, Cory Dean, Angel Rubio, and Abhay N. Pasupathy. Maximized electron interactions at the magic angle in twisted bilayer graphene. Nature, 572(7767):95–100, August 2019.

[104] Substrate cleaning with ion beams.

[105] M. Kulawik, H.-P. Rust, M. Heyde, N. Nilius, B.A. Mantooth, P.S. Weiss, and H.-J. Freund. Interaction of CO molecules with surface state electrons on Ag(111). Surface Science, 590(2-3):L253–L258, October 2005.

[106] Dler Adil Jameel. Thin Film Deposition Processes. IJMPA, 1(4):193–199, August 2015.

[107] Sami Franssila. Introduction to Microfabrication. John Wiley & Sons, October 2010. Google-Books-ID: cvoR9vmDJIQC.

[108] L. Gross, F. Mohn, N. Moll, P. Liljeroth, and G. Meyer. The Chemical Structure of a Molecule Resolved by Atomic Force Microscopy. Science, 325(5944):1110–1114, August 2009.

[109] Leo Gross, Fabian Mohn, Nikolaj Moll, Bruno Schuler, Alejandro Criado, Enrique Guitián, Diego Peña, André Gourdon, and Gerhard Meyer. Bond-Order Discrimination by Atomic Force Microscopy. Science, 337(6100):1326–1329, September 2012. Publisher: American Association for the Advancement of Science Section: Report.

[110] Johannes Thiele. Zur Kenntniss der ungesättigten Verbindungen. Theorie der ungesättigten und aromatischen Verbindungen. Justus Liebigs Annalen der Chemie, 306(1-2):87–142, 1899. _eprint: https://chemistry-europe.onlinelibrary.wiley.com/doi/pdf/10.1002/jlac.18993060107.

[111] M. F. Crommie, C. P. Lutz, and D. M. Eigler. Confinement of Electrons to Quantum Corrals on a Metal Surface. Science, 262(5131):218–220, October 1993. Publisher: American Association for the Advancement of Science Section: Reports.

[112] Yoichi Miyahara, Antoine Roy-Gobeil, and Peter Grutter. Quantum state readout of individual quantum dots by electrostatic force detection. Nanotechnology, 28(6):064001, January 2017. Publisher: IOP Publishing.

[113] Serge Luryi. Quantum capacitance devices. Appl. Phys. Lett., 52(6):501–503, February 1988. Publisher: American Institute of Physics.

[114] D. Yildiz, M. Kisiel, U. Gysin, O. Gürlü, and E. Meyer. Mechanical dissipation via image potential states on a topological insulator surface. Nat. Mater., 18(11):1201–1206, November 2019.

[115] Jan Berger, Martin Ondráček, Oleksandr Stetsovych, Pavel Malý, Petr Holý, Jiří Rybáček, Martin Švec, Irena G. Stará, Tomáš Mančal, Ivo Starý, and Pavel Jelínek. Quantum dissipation driven by electron transfer within a single molecule investigated with atomic force microscopy. Nat Commun, 11(1):1337, March 2020.

[116] Lynda Cockins, Yoichi Miyahara, Steven D. Bennett, Aashish A. Clerk, Sergei Studenikin, Philip Poole, Andrew Sachrajda, and Peter Grutter. Energy levels of few-electron quantum dots imaged and characterized by atomic force microscopy. PNAS, 107(21):9496–9501, May 2010. Publisher: National Academy of Sciences Section: Physical Sciences.

[117] Philipp Scheuerer, Laerte L. Patera, and Jascha Repp. Manipulating and Probing the Distribution of Excess Electrons in an Electrically Isolated Self-Assembled Molecular Structure. Nano Lett., 20(3):1839–1845, March 2020. Publisher: American Chemical Society.

[118] Romain Stomp, Yoichi Miyahara, Sacha Schaer, Qingfeng Sun, Hong Guo, Peter Grutter, Sergei Studenikin, Philip Poole, and Andy Sachrajda. Detection of Single-Electron Charging in an Individual InAs Quantum Dot by Noncontact Atomic-Force Microscopy. Phys. Rev. Lett., 94(5):056802, February 2005. Publisher: American Physical Society.

[119] Michael T. Woodside and Paul L. McEuen. Scanned Probe Imaging of Single-Electron Charge States in Nanotube Quantum Dots. Science, 296(5570):1098–1101, May 2002. Publisher: American Association for the Advancement of Science Section: Report.

[120] Jun Zhu, Markus Brink, and Paul L. McEuen. Single-Electron Force Readout of Nanoparticle Electrometers Attached to Carbon Nanotubes. Nano Lett., 8(8):2399–2404, August 2008. Publisher: American Chemical Society.

[121] Teresa M. Figueira-Duarte and Klaus Müllen. Pyrene-Based Materials for Organic Electronics. Chem. Rev., 111(11):7260–7314, November 2011. Publisher: American Chemical Society.

[122] Julia Merz, Julian Fink, Alexandra Friedrich, Ivo Krummenacher, Hamad H. Al Mamari, Sabine Lorenzen, Martin Haehnel, Antonius Eichhorn, Michael Moos, Marco Holzapfel, Holger Braunschweig, Christoph Lambert, Andreas Steffen, Lei Ji, and Todd B. Marder. Pyrene Molecular Orbital Shuffle-Controlling Excited State and Redox Properties by Changing the Nature of the Frontier Orbitals. Chemistry – A European Journal, 23(53):13164–13180, 2017. _eprint: https://chemistry-europe.onlinelibrary.wiley.com/doi/pdf/10.1002/chem.201702594.

[123] Y. Vyborna, S. Altunbas, M. Vybornyi, and R. Häner. Morphological diversity of supramolecular polymers of DNA-containing oligopyrenes – formation of chiroptically active nanosheets. Chem. Commun., 53(89):12128–12131, November 2017. Publisher: The Royal Society of Chemistry.

[124] Zhi Li, Alexandre Tkatchenko, and Ignacio Franco. Modeling Nonreactive Molecule–Surface Systems on Experimentally Relevant Time and Length Scales: Dynamics and Conductance of Polyfluorene on Au(111). J. Phys. Chem. Lett., 9(5):1140–1145, March 2018. Publisher: American Chemical Society.

[125] J. Fraser Stoddart. The chemistry of the mechanical bond. Chemical Society Reviews, 38(6):1802–1820, 2009. Publisher: Royal Society of Chemistry.

[126] Edel Wasserman. The Preparation of Interlocking Rings: A Catenane. J. Am. Chem. Soc., 82(16):4434–4435, August 1960.

[127] L. Gigli, N. Manini, A. Benassi, E. Tosatti, A. Vanossi, and R. Guerra. Graphene nanoribbons on gold: understanding superlubricity and edge effects. 2D Mater., 4(4):045003, August 2017. Publisher: IOP Publishing.

[128] Xin Cao, Emanuele Panizon, Andrea Vanossi, Nicola Manini, and Clemens Bechinger. Orientational and directional locking of colloidal clusters driven across periodic surfaces. Nat. Phys., 15(8):776–780, August 2019.

[129] Felix Trillitzsch, Roberto Guerra, Arkadiusz Janas, Nicola Manini, Franciszek Krok, and Enrico Gnecco. Directional and angular locking in the driven motion of Au islands on MoS2. Phys. Rev. B, 98(16):165417, October 2018. Publisher: American Physical Society.

[130] Andrea Vanossi, Clemens Bechinger, and Michael Urbakh. Structural lubricity in soft and hard matter systems. Nat Commun, 11(1):4657, September 2020.

[131] Wengen Ouyang, Davide Mandelli, Michael Urbakh, and Oded Hod. Nanoserpents: Graphene Nanoribbon Motion on Two-Dimensional Hexagonal Materials. Nano Lett., 18(9):6009–6016, September 2018. Publisher: American Chemical Society.

[132] Henry C. Astley, Chaohui Gong, Jin Dai, Matthew Travers, Miguel M. Serrano, Patricio A. Vela, Howie Choset, Joseph R. Mendelson, David L. Hu, and Daniel I. Goldman. Modulation of orthogonal body waves enables high maneuverability in sidewinding locomotion. PNAS, 112(19):6200–6205, May 2015. Publisher: National Academy of Sciences Section: Biological Sciences.

[133] Hamidreza Marvi, Chaohui Gong, Nick Gravish, Henry Astley, Matthew Travers, Ross L. Hatton, Joseph R. Mendelson, Howie Choset, David L. Hu, and Daniel I. Goldman. Sidewinding with minimal slip: Snake and robot ascent of sandy slopes. Science, 346(6206):224–229, October 2014. Publisher: American Association for the Advancement of Science Section: Report.

[134] Isaac J. Yeaton, Shane D. Ross, Grant A. Baumgardner, and John J. Socha. Undulation enables gliding in flying snakes. Nat. Phys., 16(9):974–982, September 2020.

[135] Dirk Dietzel, Ján Brndiar, Ivan Štich, and André Schirmeisen. Limitations of Structural Superlubricity: Chemical Bonds versus Contact Size. ACS Nano, 11(8):7642–7647, August 2017. Publisher: American Chemical Society.

[136] Yiming Song, Davide Mandelli, Oded Hod, Michael Urbakh, Ming Ma, and Quanshui Zheng. Robust microscale superlubricity in graphite/hexagonal boron nitride layered heterojunctions. Nature Mater, 17(10):894–899, October 2018.

[137] Shuai Zhang, Tianbao Ma, Ali Erdemir, and Qunyang Li. Tribology of two-dimensional materials: From mechanisms to modulating strategies. Materials Today, 26:67–86, June 2019.

[138] André Gourdon. On-Surface Covalent Coupling in Ultrahigh Vacuum. Angewandte Chemie International Edition, 47(37):6950–6953, 2008. _eprint: https://onlinelibrary.wiley.com/doi/pdf/10.1002/anie.200802229.

Part IV

Appendix

List of Figures

List of Tables

Nomenclature

Abbreviations

16DBP	*1,6-dibromopyrene*
2DEG	2D electron gas
27DBP	*2,7-dibromopyrene*
AC	Analysis chamber
AGNR	Armchair graphene nanoribbon
AFM	Atomic force microscope or microscopy
AM-AFM	Amplitude modulated atomic force microscope or microscopy
ARPES	Angular resolved photo-electron spectroscopy
CB	Conduction band
CNT	Carbon nano tube
CPAA	*2,7-dibromocyclopenta[h,i]aceanthrylene*
CPD	Contact potential difference
DFT	Density functional theory
DHP	*2,7-dihydroxypyrene*
DoF	Degree of freedom
DOS	Density of states
DW	Double wall
fcc	face-centered-cubic
FEL	Fast entry lock
FIB	Focussed ion beam
FM-AFM	Frequency modulated atomic force microscope or microscopy
GNR	Graphene nanoribbon
hcp	hexagonal-closed-package
HOMO	Highest occupied molecular orbital
IPS	Image potential state
KP	Kronig-Penney
LDOS	Local density of states

LJ	Lennard-Jones
LT	Low temperature
LUMO	Lowest unoccupied molecular orbital
MBE	Molecular beam epitaxy
MD	Molecular dynamics
MO	Molecular orbital
MOF	Metal organic framework
OLED	Organic light emitting diode
PC	Preparation chamber
pGNR	Pyrene-based graphene nanoribbon
PLL	Phase-lock-loop
PVD	Physical vapor deposition
PZT	Piezo-electric tube
QD	Quantum dot
QDA	Quantum dot array
QM	Quantum mechanical
QMB	Quartz-microbalance
SAM	Self-assembled monolayer
SC	Strong contact
SS	Surface state
STM	Scanning tunneling microscope or microscopy
STS	Scanning tunneling spectroscopy
SW	Single wall
TSP	Titanium-sublimation pump
UHV	Ultra high vacuum
UV	Ultra violet
VB	Valence band
vdW	Van-der-Waals
WC	Weak contact
ZGNR	Zigzag graphene nanoribbon

Symbols

Latin letters

a_α	Unitcell vector length of α-array
a_β	Unitcell vector length of β-array
A	Oscillation amplitude
A_0	Amplitude at Eigenfrequency
A_{exc}	Excitation amplitude
A_{H}	Hamaker constant
$C(z)$	Capacitance of a plate capacitor
C_{Q}	Quantum capacitance
C_{Q}^{α}	Quantum capacitance of α-array

C_{Q}^{β}	Quantum capacitance of β-array
C_{sub}	Capacitance of the sample
C_{tip}	Capacitance between tip and sample
dI/dV	Differential conductance
$d_{[11\overline{2}]}$	Distance between atoms in the $[11\overline{2}]$ direction
d_6	Diameter of hexagonal cavity
$d_{\mathrm{Au-Au}}$	Distance between gold atoms
d_{SC}	Separation in strong contact regime
d_{Wall}	Wall thickness separating cavities
d_{WC}	Separation in weak contact regime
e	Charge of an electron
E^*	Energy dissipation peak position
E_0	Ground state energy
$E_{3,1}$	Eigenenergy of the three-member cavity
$E_{6,1}$	Eigenenergy of the hexagonal cavity
$E_{8,1}$	Eigenenergy of the eight-member cavity
$E_{9,1}$	Eigenenergy of the nine-member cavity
E_{ads}	Adsorption energy
E_{Bond}	Bonding energy
E_{chain}	Energy of the polymer
E_{Diss}	Energy dissipation
E_{F}	Fermi energy level
E_{IPS}	Energy level of Image potential state
E_{kin}	Kinetic energy
E_{n}	Eigenenergy of the n-th band
E_{SS}	Surface state energy level
f	Frequency
f_0	Eigenfrequency
F_{chem}	Chemical forces between tip and sample
F_{el}	Electrostatic forces between tip and sample
F_{LJ}	Chemical forces between tip and sample described by the Lennard-Jones Potential
$F_{\mathrm{L+}}$	Force during bigger detachment lengths
$F_{\mathrm{L-}}$	Force during smaller detachment lengths
F_{sliding}	Friction forces upon sliding
F_{ts}	Total force between tip and sample
F_{vdW}	Van-der-Waals forces between tip and sample
$\hbar$	Reduced Planck constant
I	Current
I_{setpoint}	Tip-current for constant current STM measurements
k^*	Effective spring constant
k	Spring constant
k_{B}	Boltzmann constant
k_{eff}	Effective stiffness

k_{pin}	Pinning strength of the last carbon atom to the surface
k_{ts}	Spring constant of tip-sample interaction
L	Length
m^*	Effective mass
m_{e}	Mass of an electron
n	Positive integer
N_{d}	Array of n units
p	Pressure
p_{AC}	Pressure of analysis chamber
p_{FEL}	Pressure of Fast entry lock
p_{PC}	Pressure of preparation chamber
Q	Quality factor
R	Tip apex radius
r_{vdW}	Van-der-Waals interaction radius
t	Thickness
T	Temperature
T_{Ag}	Annealing temperature of silver
T_{Au}	Annealing temperature of gold
T_{He}	Boiling temperature of helium gas
$T_{\mathrm{N_2}}$	Boiling temperature of nitrogen gas
U	Potential
U_{LJ}	Lennard-Jones potential
U_{vdW}	Van-der-Waals potential
v	velocity
V^*	Voltage at dissipation peaks
V_{Bias}	Voltage between tip and sample
V_{IPS}	Voltage onset of Image potential states
V_{pulse}	Voltage pulse between tip and sample
V_{tip}	Tip-sample Voltage applied to the tip
x	Coordinate of horizontal axis on the sample surface
y	Coordinate of horizontal axis on the sample surface
Y	Youngs modulus
z	Coordinate of vertical axis, tip-sample separation

Greek letters

ΔE	Energy difference
ΔE_{Des}	Desorption energy difference
ΔE_{rot}	Rotational energy difference
Δf	Frequency shift
Δf^*	Frequency shift at dissipation peaks
Δh_{Ag}	Step height of silver
Δh_{Au}	Step height of /gold
$\Delta t_{\mathrm{anneal}}$	Time used for annealing

$\Delta t_{\text{sputter}}$	Time used for sputtering
$\Delta\theta$	Rotation angle around a pyrene-pyrene bond
Δz	Difference in tip-sample separation
δf	Full width at half-maximum
ε_0	Vacuum permittivity
Γ	Tunneling rate
Γ_α	Interdot-tunneling rate of α-array
Γ_β	Interdot-tunneling rate of β-array
κ	Dampening coefficient
π-MO	Molecular orbital formed between p-orbitals of atoms
ϕ	Rotation angle between CPAA monomers
Φ	Workfunction
Φ_s	Workfunction of the sample
Φ_t	Workfunction of the tip
ψ	Wavefunction
ρ	Mass density
$\rho(E)$	Density of states
σ	Equilibrium distance between Pauli repulsion and Van-der-Waals attraction or energy perturbation
σ-MO	Molecular orbital formed between s-orbitals of atoms of s-p-orbitals
ϑ	Lifting angle between polymer and surface

Acknowledgements

This thesis would not have been possible without the help and input of many people that I would like to give my thanks to.

First and foremost, I would like to thank Prof. Dr. Ernst Meyer for building such an amazing research-group and giving me the opportunity to be a part of it. For both my Masters and PhD research I was able to investigate many different and interesting phenomenons that changed the way I look at the world. I appreciate all the input I got during meetings and talks that helped me understand what I uncovered. Additionally, each year we were also able to partake in a group excursion, be it in winter to go skiing, or in summer to go hiking, that furthered the warm and welcoming group climate.

I would furthermore like to thank Dr. Thilo Glatzel for sharing his knowledge, expertise and advice. We had many fruitful discussions in our office that impacted my research very positively. He also helped me with all the organizational things and problems during my PhD, that I would honestly have overlooked or forgotten.

For mentoring and helping me reach my potential I would also like to thank Dr. Rémy Pawlak. He guided me during the time I was part of the group, introducing me to the tools and knowledge I needed to conduct my own research. Whenever I had difficulties, was stuck, or had problems with the machinery, he helped me figure it out and solve it. He proofread my articles, presentations and manuscripts and always took the time to give me advice on how to get better, especially during this thesis. I was also able to help him assemble a new state-of-the-art microscope gaining a deeper insight and appreciation for the technology and engineering, as well as solving technical problems. During lunch-breaks, outside the office and lab, I really enjoyed our mutual passion for motorbikes and long discussions about latest politics, sports and other topics.

Additionally I would like to thank Dr. Guilherme Vilhena. It was really enriching and enjoyable to work with him on several projects and I appreciated his input and thoughts. I also really enjoyed the time we went climbing together and the familiarity he entrusted me with.

I would further like to thank the members of the Group of Silvio Decurtins and Shi-

Xia Liu from the University of Bern, and especially Simon Rothenbühler and Xunshan Liu that provided me with the molecules I used in my research. I would not have been able to investigate these interesting phenomena if it weren't for their chemical knowhow.

Many thanks go to my colleagues on the LT Microscope, Carl Drechsel and Jung-Ching Liu. Due to the openness and friendliness in the lab I was always happy to join for discussions or help on the system. If I needed help, they were there to lend me a hand. With Carl I also spend some entertaining hours at the Pubquiz at my local Pub.

For the abundant and long discussions in the office, I would also like to thank Dr. Antoine Hinault, Alexina Ollier and Marco Sutter. The atmosphere in the office was always familial and welcoming and I always enjoyed coming back. With Antoine and Alexina we always had a connection through Sports and Marco and me could talk about Gaming, Music and Dungeons and Dragons for hours without end.

I also thank Dr. Marcin Kisiel, and Prof. Alexis Baratoff for sharing their knowledge and expertise with me.

I thank the technical staff, especially Roland Steiner and Yves Pellmont for their help in maintaining the microscope and all its components.

Many thanks go to all other members of our group that made the time I spent in this group fly by.

I thank my Family, Enrico and Annette, Martin, Susanne and Paolo, as well as my friends for always being there for me.

My deepest gratitude goes to my wife Lisa that supported me in all highs and lows, that motivated and pushed me to follow my own path. When sometimes I drove her crazy with my ways to do or don't do things, she was always understanding and helpful. I love you with all my heart ♡.

List of publications and communications

Peer-reviewed journal publications

1. **D'Astolfo, P.**; Pawlak, R.; Kisiel, M.; Drechsel, C.; Liu, J.-C.; Baratoff, A.; Aschauer, U.; Decurtins, S.; Liu, S.-X.; Meyer, E. Mechanical dissipation via the delocalized state of an array of strongly coupled quantum dots, *article in preparation* (2022)

2. **D'Astolfo, P.**; Vilhena, J. G.; Drechsel, C.; Liu, J.-C.; Liu, X.; Decurtins, S.; Liu, S.-X.; Pawlak, R.; Meyer, E. On-surface synthesis and mechanical stabilization of sterically frustrated polymers, *article in preparation* (2022)

3. Vilhena, J. G.; Pawlak, R.; **D'Astolfo, P.**; Liu, X.; Gnecco, E.; Kisiel, M.; Glatzel, T.; Pérez, R.; Häner, R.; Decurtins, S.; Baratoff, A.; Prampolini, G.; Liu, S.-X.; Meyer, E. Flexible-Superlubricity unveiled in Sidewinding Motion of Individual Polymeric Chains, *article under review* (2021)

4. Drechsel, C.; **D'Astolfo, P.**; Liu, J.-C.; Glatzel, T.; Pawlak, R.; Meyer, E. Topographic signatures and manipulations of Fe atoms, CO molecules and NaCl islands on superconducting Pb(111), *Beilstein Archives*, *Beilstein J. Nanotechnol.* **13**, 1-9, (2022). DOI: 10.3762/bjnano.13.1

5. Pawlak, R.; Liu, X.; Ninova, S.; **D'Astolfo, P.**; Drechsel, C.; Liu, J.-C.; Häner, R.; Decurtins, S.; Aschauer, U.; Liu, S.-X.; Meyer, E. On-Surface synthesis of Nitrogen-Doped Kagome Graphene, *Angew. Chem. Int. Ed.* **60**, 8370–8375, (2021). DOI: 10.1002/anie.202016469

6. Pawlak, R.; Drechsel, C.; **D'Astolfo, P.**; Kisiel, M.; Meyer, E.; Iribas Cerda, J. Quantitative determination of atomic buckling of silicene by atomic force microscopy, *PNAS* **117**, 228-237, (2020). DOI: 10.1073/pnas.1913489117

7. Pawlak, R.; Liu, X.; Ninova, S.; **D'Astolfo, P.**; Drechsel, C.; Sangtarash, S.; Häner, R.; Decurtins, S.; Sadeghi, H.; Lambert, C. J.; Aschauer, U.; Liu, S.-X.;

Meyer, E. Bottom-up Synthesis of Nitrogen-Doped Porous Graphene Nanoribbons, *J. Am. Chem. Soc.* **142**, 29, 12568–12573 (2020). DOI: 10.1021/jacs.0c03946

8. Pawlak, R.; Vilhena, J. G.; **D'Astolfo, P.**; Liu, X.; Prampolini, G.; Meier, T.; Glatzel, T.; Lemkul, J. A.; Häner, R.; Decurtins, S.; Baratoff, A.; Pérez, R.; Liu, S.-X.; Meyer, E. Sequential Bending and Twisting around C–C Single Bonds by Mechanical Lifting of a Pre-Adsorbed Polymer, *Nano Lett.* **20**, 1, 652-657 (2019). DOI: 10.1021/acs.nanolett.9b04418

Presentations

1. **D'Astolfo, P.**; Vilhena, J. G.; Drechsel, C.; Liu, J.-C.; Liu, X.; Decurtins, S.; Liu, S.-X.; Pawlak, R.; Meyer, E. Lifting and Manipulation of molecular wires, molCH Meeting, virtual, Switzerland (18.06.2021)

2. **D'Astolfo, P.**; Pawlak, R.; Drechsel, C.; Glatzel, T.; Decurtins, S.; Liu, S.-X.; Meyer, E. Confined States in self-assembled $(OH)_2$-pyrene porous networks on Ag(111). DPG-Frühjahrstagung, Regensburg, Germany (01.04.2019)

Posters

1. **D'Astolfo, P.**; Vilhena, J. G.; Drechsel, C.; Liu, J.-C.; Liu, X.; Decurtins, S.; Liu, S.-X.; Pawlak, R.; Meyer, E. On-Surface synthesis and mechanical stabilization of class 1 atropoisomers, DPG-Frühjahrstagung, virtuell, Germany (01.03.2021-04.03.2021)

2. **D'Astolfo, P.**; Pawlak, R.; Drechsel, C.; Glatzel, T.; Decurtins, S.; Liu, S.-X.; Meyer, E. Confined States in self-assembled $(OH)_2$-pyrene porous networks on Ag(111). Swiss NanoConvention, Lausanne, Switzerland (2019) (06.06.2019)